Modeling the Solar Forcing of the Total Column Ozone Variation in Selected Cities in Kenya

Carolyne May Mutambi Songa

A Thesis submitted in Partial fulfillment for the Degree of Doctor of Philosophy in Physics in the Jomo Kenyatta University of Agriculture and Technology

2017

DECLARATION

This thesis is my original work and has not been presented for a degree in any other University.

Signature ……………………………….. Date……………………

Carolyne May Mutambi Songa

This thesis has been submitted with our approval as university supervisors.

1. Signature …………………………………… Date ……………………..

    Dr. Jared O. H. Ndeda, PhD

    JKUAT, Kenya

2. Signature …………………………………… Date ……………………..

DEDICATION

This research work is dedicated to my husband Frank; Sons, Barvin, Ray and Neon. To my dear Mummy Juliana for always being there for me and always confident in what I do. To my Dad, Stephen; I know you always wanted the best for me. To my brothers and sisters and my dearest friend; Margaret Seth.

ACKNOWLEDGEMENT

Mama, through your prayers, love and silent support, I pressed on. You continuously enquired on my progress and every time cheered me on. Thank you Mama. Last but not least, I appreciate my brothers and sisters' support and love. You visited me without complaining of me doing the same. You always called me to find out how I was progressing on. I thank you.

I would like to thank all those who supported me directly and indirectly throughout my research work.

TABLE OF CONTENTS

LIST OF TABLES

LIST OF FIGURES

LIST OF SYMBOLS

∇	Gradient
∇^2	Laplacian operator
B	Magnetic field
σ	Electrical conductivity
μ	Average number of particles
ρ	Mass density
v	Fluid velocity
R_m	Magnetic Reynolds's number
ε	Mean electromotive force
α	Measure of mean helical motion in fluids
τ	Turbulent time
β	Turbulent diffusion coefficient
R_z	Relative sunspot number
η	Artificial neural network learning rate
R_E	Earth's radius
C_p	Specific heat capacity at constant pressure

LIST OF ABBREVIATIONS

ACIA   Arctic Climate Impact Assessment

ANN   Artificial Neural Network

ANOVA   Analysis of Variance

AU   Astronomical Unit

CFC   Chlorofluorocarbons

DNA   Deoxyribonucleic Acid

DU   Dobson Unit

ECVs   Essential Climate Variables

ENSO   El Nino South Oscillation

ETSP   Extra Terrestrial Suction Pump

EUV   Extreme Ultraviolet

FFT   Fast Fourier Transform

FPL   Free Path Length

GCOS   Global Climate Observing Systems

IPCC   Intergovernmental Panel on Climate Change

MAE	Mean Absolute Error
MHD	Magneto-Hydro Dynamics
MLFNN	Multi-Layer Feed-forward Neural Networks
MLR	Multiple Linear Regression
MOD	Merged Ozone Data
NASA	National Astronomies and Space Administration
NGDC	National Geophysical Data Centre
NOAA	National Oceanic and Atmospheric Administration
OMI	Ozone Monitoring Instruments
PE	Predictive Error
QBO	Quasi Biennial Oscillations
RMSE	Root Mean Square Error
SAI	Solar Activity Indices
SBUV	Solar Backscatter Ultraviolet
SFU	Solar Flux Unit
SOLSTICE	Solar Stellar Irradiance Experiment
STP	Standard Temperature and Pressure

SUSIM	Solar Ultraviolet Spectral Irradiance Monitor
TCO	Total Column Ozone
TOMS	Total Ozone Mapping Spectrophotometers
TSI	Total Solar Irradiance
UARS	Upper Atmospheric Research Satellite
UNEP	United Nation Environment Programme
UV	Ultraviolet
WSN	Wolf's Sunspot Number

ABSTRACT

A quantitative non- experimental correlation study aimed at investigating the relationship between ozone and the solar activity indices for the period 1985- 2011 was carried out. Dataset for solar activity indices were collected from the National Geophysical Data Centre through their website while dataset for total column ozone over Nairobi (1.17º S; 36.46º E), Kisumu (0.03º S; 34.45º E) and Mombasa (4.02º S; 39.43º E) from combined multiple satellite based instruments prepared by Bodeker scientific were collected through their website; both of which are publicly accessible and available. Analysis of trend and variability was done for the variables for each city. Correlation analysis was performed to analyze the relationship between time series data. A spectral analysis was carried out to characterize the frequency dependence of daily variation. Total column ozone and solar activity indices data were fitted on to multiple linear regression and the artificial neural network models. Statistical indicators were employed to verify the quality and reliability of the fitted models. A decreasing trend of 0.031% year^{-1} was observed at Nairobi, 0.026% year^{-1} at Kisumu and 0.031% year^{-1} at Mombasa over the study period. Lowest total ozone values appeared in warm dry season. Short rainy season recorded the highest total ozone. Total ozone annual variability ranged between 1% and 6%, while the seasonal variability ranged between 2% and 4%. Solar activity indices and total ozone were positively correlated and significant. Solar activity had both immediate and delayed impact on total ozone. An increase in total ozone of about 1 − 4 % was attributed to solar activity indices. A negative forcing of Mg II index was observed in all the cities. Three types of periodicities 6 months, 12 months and 30 months were identified. Only Mg II index significantly affected total column ozone in all the cities. Neural networks in the form of multilayer perceptron feed forward with backpropagation algorithm with a sigmoid activation function with supervised learning method in the form of 3-15-1 were obtained in all the cities. Neural networks showed slightly better skills in predicting total column ozone. Therefore the temporal variability of total column ozone in all the three cities was declining. Not all solar activity indices had significant contributions in the variation of stratospheric ozone.

CHAPTER ONE

INTRODUCTION

1.1 Background

Scientific curiosity and societal utility both call for a robust understanding of the sun - earth system (Haigh, 2007; Benestad, 2006; Lean, 2005). Although Sun and Earth are separated by 150 million kilometers, they are inextricably linked by an energy flow that both sustains and imperils life. This dominant energy flow from the Sun's surface to Earth's enables life by heating the planet, fueling photosynthesis and powering the interactions among oceans, land and atmosphere that generate weather and climate (Ruddiman, 2001).

The Sun, undergoes changes characterized by variations in its output ranging from minutes to months and decades due to the different degrees of activity (Lockwood, 2005) and these variations reflect the inhomogeneous emission of radiation due to the presence and absence of active regions on the solar disk. The variations occur because of the changing impacts of the solar features whose opposing influences depend on the wavelengths. The three manifestations of solar variability are variations of solar structures, electromagnetic radiations and energetic solar particles. Variations of the solar electromagnetic radiation are the cause of the radiated solar output variability both total and in various wavelengths (Spruit, 2000).

The magnetic fields generated by a self-exciting magneto hydrodynamics (MHD) dynamo in the interior of the sun controls the solar activity (Charbonneau, 2005). The distinctive features perpetrated by these magnetic fields are displayed on different solar spheres, namely, the photosphere, chromosphere, and corona. Even though different solar layers are coupled, the variability is strongly wavelength dependent.

1

Solar cycle variations affect stratospheric ozone through changes in the UV fluxes that affects the dissociation of chemical species. In particular, the solar Ultraviolet (UV) radiation plays a major role in the temperature, dynamics and photochemistry of the stratosphere (Newman, 2004; Gray, Rumbold & Shine, 2009; Gray, 2010). UV radiation between 120 and 300 nm is absorbed in the earth's outer atmosphere by ozone and molecular oxygen. Increased levels of UV radiation heat the stratosphere and mesosphere due to absorption by ozone and oxygen. Therefore variations in the different spectral regions can have a major impact on the Earth's atmosphere (Geller, 1988; Marsh, Garcia, Kinnison, Boville, Sassi, Solomon & Matthes, 2007) since the origins and fate of life on Earth are intimately connected to the way different layers of the Earth's atmosphere respond to these variations (Tsiropouli, 2003).

Many different indicators have been employed to measure solar activity (Lean, 2001). These include; the Geomagnetic activity index (aa index), AE index, AL index, ca index Kp index, sunspot index, am index, AO index, Mg II core- to-wing ratio and F10.7 cm solar radio flux and E10.7 cm solar radio fluxes. No single proxy can produce the solar variability over the whole UV spectrum, hence, various other indicators and proxies for various UV spectral bands that encompass emissions coming from the solar corona down to the photosphere do exist (Dudok, Kretzschmar, Lilensten & Woods, 2009) and have been tested (de Wit & Watermann, 2010). The indices of interest in this study are the sunspot numbers, the F10.7 cm solar radio flux and Mg II core to wing ratio.

The sunspots, visible on the solar disk at any given time, has been the most commonly used parameter and the basic indicator of solar activity hence, a proxy for the general state of solar activity. Relative sunspot numbers are the collection of sunspot numbers that provide spot counts averaged over different time intervals. It is given by the sum of the number of individual sunspots and ten times the number of groups. On average, most sunspot groups have about ten spots; hence this formula for counting sunspots gives reliable numbers even when the observing conditions are less than ideal and small spots difficult to observe (Jana & Bhattacharyya, 2013)

The 10.7-cm solar radio flux, F10.7 was first observed by Covington (1948). F10.7 index is the solar output originating in the high solar atmospheric layers of the chromosphere and in lower corona. The solar flux, measured in solar flux units (SFU) (Tobiska, Bouwer & Bowman, 2008), is the amount of radio noise or flux emitted at a frequency of 2800 MHz (10.7 cm).

Representing a measure of diffuse, non-radiative heating of the coronal plasma trapped by magnetic fields over the active regions, the F10.7 index is an excellent indicator of overall solar activity levels in the UV region. Each value of F10.7 index is a measurement of the total emission at a wavelength of 10.7 cm from all sources present on the solar disk, made over a one hour period centered on the epoch given for the value (Tapping, 2013)

The Mg II core-to-wing index has been shown to be a good measure of solar chromospheric activity for solar features and wavelengths that have strong chromospheric components (Viereck, Puga, McMullin, Judge, Weber & Tobiska, 2001). It is a ratio of the Mg II chromospheric emission at 280 nm to the photospheric radiation in the line wings (Toma, White, Knapp, Rottman & Woods, 1997). Introduced by Heath and Schlesinger (1986), the Mg II core-to-wing ratio is one of the most widely used indices of solar activity in the UV region.

The Mg II core to wing ratio is calculated by taking the ratio between the highly variable chromospheric Mg II h and k lines at 279.56 and 280.27 nm respectively and weakly varying wings or nearby continuum which are photospheric in origin. The result is mostly a measure of chromospheric solar active region emission that is theoretically independent of instrument sensitivity change through the time (Bruevich, E. & Bruevich, V., 2013)

The atmosphere, which consists of the lower, middle and upper atmosphere levels, is the transition zone between earth and space made up of a mixture of gases. These gases are exposed to the sun's electromagnetic spectrum. In the middle atmosphere, ozone plays a major role in both radiation and chemistry.

Ozone is the main gas involved in radiative heating of the stratosphere. Solar-induced variations in ozone can therefore directly affect the radiative balance of the stratosphere with indirect effects on circulation. Solar-induced ozone variations are possible through changes in solar ultraviolet (UV) spectral solar irradiance, which modifies the ozone production rate through photolysis of molecular oxygen, primarily in the mid-to-upper stratosphere at low latitudes (Haigh, 1994; Dessler, 2000).

Solar-induced ozone variations are possible also through changes in the precipitation rate of energetic particles, which can indirectly modify ozone concentrations through changes in the abundance of trace species that catalytically destroy ozone, primarily at polar latitudes (Randall et al., 2007). In addition, transport-induced changes in ozone can occur (Hood & Soukharev, 2003; Rind, Shindell, Perlwitz, Lerner, Lonergan, Lean & McLinden, 2004; Shindell, Faluvegi, Miller, Schmidt, Hansen & Sun, 2006; Gray, Rumbold & Shine, 2009) as a consequence of indirect effects on circulation caused by Brewer – Dobson circulation (Andrews, 2000) and Quasi-biennial Oscillation (Baldwin et al., 2001).

The Global Climate Observing System (GCOS), in their report (Secretariat, G. C. O. S., 2009), identified Total Column Ozone (TCO) to be among the fifty Essential Climate Variables (ECVs). Both stratospheric depletion and tropospheric excess of ozone are harmful to the biosphere. This calls for the monitoring of ozone concentration variations and trends in both the stratosphere and troposphere. Total column ozone (TCO) is composed of the tropospheric and stratospheric ozone content. TCO is a measure of the vertically integrated ozone molecules in the atmosphere's column above a specific location.

The global distribution of TCO is well known (Stanford, Ziemke, McPeters, Krueger & Bhartia, 1995; Plumb, 2002; Zahid & Rasul, 2010). At equatorial latitudes, a minimum of around 260 DU (Dobson Units; defined as 0.01 mm total thickness of the ozone layer at standard temperature and pressure, that is, 0º Celsius and one atmosphere pressure; 1 DU contains 2.69×10^{16} molecules cm^{-2}), increasing to between 300 – 350 DU at mid

latitudes and increasing further towards the North and South poles reaching a maximum value of approximately 450 – 500 DU at sub-polar latitudes.

Stratospheric ozone is produced by the ultraviolet radiation. The amount of ozone in any region depends on the balance between ozone production and loss processes and the transport of ozone by atmospheric dynamics (Haynes, 2005; Garny, Grewe, Dameris, Bodeker & Stenke, 2011). There is more ultraviolet radiation over the equator, as compared to high latitudes, hence ozone production. It is therefore expected that the highest concentration of ozone levels must be found over the tropics and the lower levels over the Polar Regions, but this is not the case, the observed behavior is quite different. The high-latitude maximum ozone is due to ozone transport from the equator (source) to higher latitudes (Whitten & Prasad, 1985).

TCO amounts near the equator are rather low, that is, less than the typical global average of $\approx$ 300 DU. These low TCO amounts in the tropics combined with the direct overhead sun, create the very high amounts of UV levels (Bais et al., 2007). Chapman (1930) proposed the fundamental ozone formation and destruction chemical reactions which include the photolysis of molecular oxygen by solar ultraviolet (UV) radiation ($\lambda <$ 242 nm) given by reaction 1.1. The rapid reaction of oxygen atoms (O) from reaction 1.1 with O_2 in the presence of a third molecule M*, usually O_2 or N_2, form ozone (reaction 1.2). Photolysis of ozone molecules from reaction 1.2 by radiation at wavelengths less than 320 nm produces O and O_2 through reaction 1.3. O_3 can also react very fast with atomic oxygen and convert back to O_2 molecules via reaction 1.4.

$$O_2 + hv \rightarrow 2O^{\cdot} \tag{1.1}$$

$$O + O_2 + M \rightarrow O_3 + M* \tag{1.2}$$

$$O_3 + hv \rightarrow O^{\cdot} + O_2 \tag{1.3}$$

$$O^{\cdot} + O_3 \rightarrow 2O_2 \tag{1.4}$$

Haigh (1994) and Dessler (2000) observed that solar enhanced ozone variations are possible due to solar ultraviolet (UV) irradiance changes. The UV irradiance is capable of modifying the ozone production rates through molecular oxygen photolysis basically at low latitudes in the middle to the upper stratosphere. According to Randall et al., (2007), solar enhanced ozone variations are possible due to changes in highly energetic charged particles precipitation rate indirectly modifying the concentration of ozone by catalytically changing the trace species abundance which destroy ozone fundamentally at the polar latitudes.

Transport enhanced (Hood & Soukharev, 2003; Rind, Shindell, Perlwitz, Lerner, Lonergan, Lean & McLinden, 2004; Shindell, Faluvegi, Miller, Schmidt, Hansen & Sun, 2006; Gray, Rumbold & Shine, 2009; Gray, 2010) ozone changes occur because of Brewer-Dobson circulation (Andrews, 2000), quasi-biennial oscillation (Baldwin et al., 2001) and the El-Nino Southern Oscillation (Akinyemi, 2007), which indirectly affect circulation.

The use of satellite measurements to investigate stratospheric ozone variations and trends, as well as their seasonal, longitudinal and latitudinal structure has contributed immensely to a global view of the climatology of and variability in stratospheric ozone (Oyekola, 2011). One of the purpose of this study is to quantify trends and variability in TCO over three Kenyan cities using data from combined multiple satellite-based instruments to create a single near-global daily time series of TCO fields.

One of the most important needs of the ozone community is to perform accurate predictions (daily, monthly, yearly, and long term) of the variability in the ozone layer in order to assess, among others, the induced increase in the solar radiation doses measured at the Earth's surface (Chattopadhyay, 2007; Chattopadhyay & Chattopadhyay-Bandyopadhyay, 2007). Many approaches, linear and non linear have been made to determine ozone levels. Multiple linear regression, principal component regression, quartile regression among others are a few examples of linear models (Sousa, Pires, Martins, Pereira & Alvim-Ferraz, 2009; Pires & Martins, 2011).

A number of literature are available where statistical methodologies have been applied to look into different features of tropospheric and stratospheric ozone and their relationship with various meteorological parameters (Cartalis & Varotsos, 1994, Allen & Reck, 1997; Varotsos, Kondratyev & Efstathiou, 2001; Varotsos 2005; Varotsos & Kirk-Davidoff, 2006; Hansen & Svenøe, 2005; Aksoy et al., 2009).

The other approach is the use of Artificial Neural Networks (ANNs) (Rojas, 1996). In recent years ANN has opened up new avenues to forecast time series pertaining to complex and chaotic system research such as meteorological forecasting (Gardner & Dorling, 1998), ecological modeling and forecasting (Nunnari, Nucifora & Randieri, 1998) and financial forecasting (Ostermark, 1999).

ANNs are nonlinear models most commonly used (Gardner & Dorling, 2001 Latini, Grifoni & Passerini, 2002) to develop predictive models without a priori knowledge of the underlying process, recognizing existing complex relationships among various aspects of the process under investigation and constraints and assuming or enforcing a priori solution structures (Silverman & Dracup, 2000). Because of the non-linearity of TCO and the complex interactions between ozone and meteorological variables, the development of non-linear models like ANNs have proved their superiority over conventional methodologies, thus ANNs have gained the attention of several researchers working in the area of tropospheric ozone forecasting.

A study on the relationship between ozone and solar activity has not been carried out in cities and towns in Kenya. Hence to give an idea of solar activity effect in this low latitude region, the contributions or inputs of the solar activity indices namely; the international sunspot number (index of the sun's photosphere), the 10.7 cm solar radio flux from the sun's corona and the Mg II core-to-wing ratio (index of the sun's chromospheres), are considered for the sun's influence on the stratospheric ozone in Kenyan cities namely Nairobi, Kisumu and Mombasa using statistical analysis.

1.2 Problem Statement

Ozone exists at different heights surrounding the Earth and in different proportions depending on the physical situation of its formation (Rubin, 2001). TCO includes both tropospheric and stratospheric ozone. TCO is important due to its direct measurable effect on the amount of UV radiation reaching the surface of the Earth (Obiekezie, 2009). The presence of ozone leads to enhanced absorption of UV radiation resulting in shielding of the atmosphere below. Kerr and McElroy (1993) showed that decreased ozone levels have caused increase of ultraviolet radiation at the Earth's surface. Decreased ozone allows the harmful UV -B radiation (photons in the wavelength range 280-320 nm) and UV -C radiation (photons in the wavelength range 100-280 nm) which can affect the health of human, animal and plants (Van der Leun, & de Gruijl, 1993).

According to the WMO Ozone Assessment (1995), the global average TCO changes correlate with solar UV flux variations in the 11-year solar cycle, changing by about 1-5 % from solar maximum to solar minimum. The changing character of the magnetic fields generates the different degrees of the Sun's activity whose manifestation is observed through the existence and variability of the large number of solar features on the different layers of the solar atmosphere, but also through the variability of the solar electromagnetic radiation.

Ultraviolet (UV) rays of the Sun are associated with a number of health related and environmental issues. Environmental consequences of ozone depletion include: the alteration of the Earth's radiative energy balance and the increase in the amount of harmful UV radiation reaching the Earth's surface as stated by Agterberg and Brassard (2001) in their discussion on the effects of ozone depletion.

A 10% decrease in total stratospheric ozone is expected to cause an additional 300,000 cases of non – melanoma and 4,500 melanoma skin cancers globally each year (WHO, 1998). Without the Montreal Protocol, ozone depletion would have accounted for an additional 20 million cases of skin cancer (Linkages, 1999).

Due to the suppression of the immune system by UV radiation, particularly in skin cells, infectious diseases having a stage involving the skin are likely to increase. An estimated 20% of cataracts are due to UV exposure (WHO, 1998). Constant exposure to UV radiation can cause photo allergy, which results in the outbreak of rash in fair-skinned people. Ozone chemicals can cause difficulty in breathing, chest pain, throat irritation, and hamper lung functioning.

Kenya is a country largely dominated by dark skin, albinos and fair- skinned people. Kenya depends on tourism and agriculture for its economy; therefore those with fair skin, including the tourists, are at high risk of exposure to UV radiations. Majority of people in Kenya have high outdoor activities for example, fishing, 'jua kali' artisans, school children and women, all are exposed to high doses of UV radiation.

About 1.5 million people in Kenya are living with HIV (Kenya Aids Response report, 2014), the precursor for AIDS or any other virus that attack the immune system hence apart from weakening of the body's immunity by viruses, UV radiation also enhances the weakening of the immunity by being absorbed by a molecule located in the skin leading to changes in the distribution and activity of some of the key molecular and cellular players of the immune system.

A study on the relationship between ozone and solar activity has not been carried out in cities and towns in Kenya. Hence to give an idea of solar activity effect in this low latitude region, the contributions or inputs of the solar activity indices namely; the international sunspot number (index of the sun's photosphere), the 10.7 cm solar radio flux from the sun's corona and the Mg II core-to-wing ratio (index of the sun's chromospheres), are considered for the sun's influence on the stratospheric ozone in Kenyan cities namely Nairobi, Kisumu and Mombasa using statistical analysis.

1.3 Objectives

1.3.1 General Objective

The main objective of this study is to model total column ozone by investigating solar forcing of ozone in Kenya so as to ascertain the contributions of the solar activity indices on the stratospheric ozone in Kenya

1.3.2 Specific objectives

(i)   To derive monthly and annual means from the daily total column ozone over Kenya's cities and solar activity indices.

(ii)   To establish the pattern of temporal variations of total column ozone and solar activity indices.

(iii)   To fit a predictive model to the total column ozone and solar activity indices data.

(iv)   To evaluate the performance of the fitted predictive model.

(v)   To predict total column ozone values using the fitted model.

1.4 Justification

Issues concerning depletion of ozone border us. This is because it affects lives on Earth and what affects our being will be our priority research work. Some research works on the variation of ozone have been carried out in temperate regions but very few in the equator where Kenya lies. It has long and recently been noted that TCO amounts near the equator show the least variation and are rather low (less than the approximated global average of 300 DU), over the course of the year. These low total ozone amounts in the tropics combined with the direct overhead sun creates the very high amounts of UV-B exposures. It therefore becomes pertinent that this study be carried out in order to understand the natural factors that control ozone concentrations in the stratosphere. The solar activities at the various spheres as proxies by the solar parameters; sunspot numbers (proxy of the photosphere), F10.7 cm solar radio flux (proxy of the corona) and Mg II core to wing ratio (proxy of the chromospheres) are possible forming agents of the

stratospheric ozone. Hence it is important to model the solar forcing of TCO in the region using the solar parameters so as to ascertain the causes of TCO variation. The study would come up with a good performing predictive model that can be used to mitigate effects of UV exposures resulting from low TCO values.

1.5 Research Questions

In light of the main objective and specific objectives of the study, the following research questions are supported:

a) Research Question 1:   What is the relationship between ozone concentration and

   solar indices at each station?

b) Research Question 2:   What is the effect of the solar indices on ozone

   concentration?

1.6 Hypothesis

With these research questions, the following hypotheses were formulated. For the first research question:

H_0: There is no significant linear relationship between solar activity indices and ozone

   concentration at each city.

For the second research question:

H_0: The solar indices do not significantly predict the ozone concentration.

CHAPTER TWO

LITERATURE REVIEW

2.1 Introduction

The Sun-Earth connection is a world of paradoxes. Until recently, this seamless system was widely considered as a stack of independent layers, and only in recent times did the interactions between these layers really attract attention. The role of the Sun in our solar system goes undisputed, and yet the effect of solar variability on the atmosphere remains quite controversial (de Wit & Watermann, 2010).

The Sun (like any living star) continuously radiates energy outward into the heliosphere. The heliosphere refers to the space from the Sun through the Earth to the end of the solar system; the heliopause. The radiated energy is carried by (i) electromagnetic waves over a frequency band ranging from radio waves to hard X-rays, (ii) a stream of hot plasma

2.2 Solar Variability

The solar irradiance, or the solar flux received at the top of the Earth's atmosphere, is known to vary over a large number of time scales, ranging from minutes to months and decades. The changes in the total solar output have been measured since1978 (Willson & Hudson, 1988) and different composites of the measurements have been presented by Fröhlich and Lean (1998); Willson and Mordvinov (2003) and Dewitte, Crommelynck, Mekaoui & Joukoff (2004). While the short-term (minutes to hour) variability is mainly due to solar oscillations and granulation, the daily to decadal variability is attributed to the changes in the surface magnetic field combined with the solar rotation that transports solar active regions into and out of view (Brasseur, 1993; Chandra, 1991; Hood & Zhou, 1999)

Krivova, Solanki, Fligge and Unruh (2003) found that more than 90% of the solar variability between 1996 and 2002 could be explained by changes in the solar surface field. Similar conclusions were reached by Wenzler, Solanki, Krivova and Fröhlich (2006) who reconstructed solar irradiance from Kitt Peak magnetograms covering the last three solar cycles. Solar variability is a strong function of wavelength. While solar

output is small in the UV, the relative variability is more than one order of magnitude larger in the UV than in the visible. Until very recently, the spectral dependence of the solar variability had mainly been determined in the UV region.

The variability at most other wavelengths had to be inferred using a variety of approaches, such as the one pioneered by Lean (1989) who produced the first estimate of solar-cycle variability over a large wavelength range. An alternative approach was followed by Unruh, Solanki and Fligge (1999) who used facular and spot model atmospheres to calculate the flux changes due to magnetic features. Fligge and Solanki, (2000) and Krivova et al., (2003) used solar surface images and magnetograms to calculate the variability on time scales ranging from days to years.

2.3 Solar Photospheric Variability

Magnetic phenomena are sources of significant solar radiation variability. Waxing and waning magnetic activity throughout the solar cycle produces changing sunspots, faculae, plages, and network that modify the Sun's net radiative output by altering temperature and density in the otherwise homogeneous solar atmosphere. Magnetic regions occur frequently when solar activity is high, but they are sparse or absent during low activity epochs.

In different solar atmosphere regimes, magnetic fields perpetrate distinctive features, which are displayed on different solar spheres, namely, the photosphere, chromosphere, and corona. In the photosphere, clumps of very strong magnetic fields—thousands of gauss—form sunspots that are darker and cooler than the surrounding photosphere because the magnetic fields somehow inhibit the upward flow of energy from the convection zone to the surface. Sunspots are compact in shape because gas pressure in the photosphere is large enough to balance the magnetic field strength. Less compact aggregates of field lines form faculae, which are slightly brighter than the surrounding photosphere and barely detectable in visible light images of the solar disk except near the limb (Foukal, 1990).

2.4 The Solar Spectral Radiation

The performances of some proxies for various UV spectral bands that encompass emissions coming from the solar corona down to the photosphere have been tested (de Wit & Watermann, 2010). The variability should therefore be strongly wavelength dependent, even though different solar layers are coupled. The solar UV radiation mostly affects the terrestrial atmosphere through photochemical reactions, which are again wavelength-dependent processes (Floyd, Tobiska & Cebula, 2002; Lilensten, Wit, Kretzschmar, Amblard, Moussaoui, Aboudarham & Auchre, 2008).

The radiation in the middle UV (MUV) range (200–300 nm) mostly affects the stratospheric O_3 concentration; the Far UV (FUV) range (122–200 nm) affects the upper mesospheric O_2 excitation production and the lower thermospheric O_2 dissociation; the Extreme UV (EUV) range (10–120 nm) affects the thermospheric O, O_2 and N_2 ionization and excitation productions (Floyd et al., 2002; Lilensten et al., 2008).

2.5 Solar Corona Variability

The 10.7-cm solar radio flux, F10.7, was first observed by Covington (1948) on a daily basis beginning on February 14, 1947 and is now produced daily by the Canadian National Research Council's Herzberg Institute of Astrophysics at its ground-based Dominion Radio Astrophysical Observatory located in Penticton, British Columbia. The physical units of F10.7 are ($\times 10^{-22}$ W m^{-2} Hz^{-1}). The numerical value is used without the multiplier as is customarily done and expressed as solar flux units (sfu). That is, a 10.7-cm radio emission of 150×10^{-22} W m^{-2} Hz^{-1} is simply referred to as F10.7 = 150 sfu (Tobiska, Bouwer & Bowman, 2008).

As a measure of solar activity one can use the sunspot number or the solar radio flux at 10.7 cm (F10.7), which is the solar output originating in the high solar atmospheric layers of the chromosphere and in lower corona. It has been routinely recorded since February 1947. The F10.7 does not have significant impacts in the atmosphere, but it is

used as a proxy for total and spectral solar irradiance, including the ultraviolet irradiance, which is very important in terms of atmospheric processes (Whitten & Prasad, 1985).

2.6 Solar Chromospheric Variability

The Mg II core-to-wing ratio is a measure of solar chromospheric variability. The Mg II Index, formed by combining various Mg II core-to-wing data sets, has been used in EUV, UV, and total solar irradiance models. It is one of the longest records of solar variability dating back nearly 25 years. The Mg II core-to-wing ratio has been shown to be a good measure of solar chromospheric activity for solar features and wavelengths that have strong chromospheric components. It has been shown to be a good proxy for solar flux at many EUV wavelengths. In particular, the correlation between the Mg II Index and the integrated solar flux between 25 and 35 nm is extremely good (Viereck et al., 2001)

2.7 Solar Irradiance Measurement

Solar irradiance has been measured by different space experiments since 1978, and variability over the 11-year solar cycle has been recorded. Instruments which have contributed to solar studies include the Solar Backscatter Ultraviolet (SBUV) experiments on board of Nimbus 7 and NOAA satellites and two instruments from the Upper Atmosphere Research Satellite (UARS), the SUSIM and SOLSTICE instruments, both specifically designed for solar observations.

2.8 Ozone in the Atmosphere

Stratospheric structure is divided into distinct regions, that is, the upper, middle and lower stratosphere, all of which have no interaction with the troposphere via isentropic transport and then the lower-most stratosphere which does interact with the upper troposphere via isentropic transport (Holton *et al.,* 1995). In the stratosphere, the tropics stretch from 15ºS to 15ºN. This is the primary photochemical source region of ozone production due to high levels of radiation at wavelengths less than 242 nm (reaction 1.1). The middle latitudes are characterized by the turbulent mixing of air masses. The

lower-most stratosphere contains a mixture of both the tropospheric and stratospheric air.

Ozone is located in two different layers of the atmosphere – that in the troposphere known as 'bad ozone' that pollutes the air and helps make smog, while the one in stratosphere is referred to as 'good ozone' because, it protects life on earth by absorbing some of the sun's UV rays. This natural shield has been gradually depleted by manmade chemicals like chlorofluorocarbons (CFCs). A depleted ozone shield allows more UV radiation to reach the ground, leading to more cases of skin cancer, cataracts, and other health and environmental problems (http://www.epa.gov/ozone).

Concentration of O_3 in the troposphere is mainly contributed by two processes: one is downward distribution of stratospheric ozone and photochemical production of ozone. In photochemical production of ozone, the required atomic oxygen comes from the photodissociation of nitrogen II oxide at shorter wavelengths (<420 nm) (Naja & Lal, 1997); also, as a result of combustion of volatile organic compounds. Sunlight splits nitrogen dioxide into nitric oxide and oxygen atom. A single oxygen atom then combines with an oxygen molecule to produce ozone. This process results in no net gain in ozone. Nitric oxide and nitrogen dioxide are together known as NOx Finlayson-Pitts & Pitts Jr, 1999).

Surface ozone (O_3) is a highly efficient greenhouse gas; its global warming potential is about 1200 - 2000 times that of carbon dioxide (CO_2), (Houghton, Jenkins & Ephraums, 1990). Global warming refers to an increase in the earth's temperature, which in turn causes changes in climate. A warmer earth may lead to changes in rainfall patterns, a rise in sea level, and a wide range of impacts on plants, wildlife, and humans; this invariably is the issue of climate change. A recent IPCC report (2001) has ranked ozone as the third most important factor in terms of contributing to human-caused radiative forcing of the climate system.

Stratospheric ozone is created and destroyed primarily by ultraviolet (UV) radiation. The air in the stratosphere is bombarded continuously with UV radiation from the sun. When

high energy UV rays strike molecules of ordinary oxygen (O_2), they split the molecule into two single oxygen atoms. The free oxygen atoms can then combine with oxygen molecules (O_2) to form ozone (O_3) molecules. The same characteristic of ozone that makes it so valuable (its ability to absorb a range of UV radiation) also causes its destruction. When an ozone molecule is exposed to UV energy it may revert back into O_2 and O. During dissociation, the atomic and molecular oxygen gain kinetic energy, which produces heat and causes an increase in atmospheric temperature.

The photolysis of ozone is a primary source of the hydroxyl free radical (OH), which is the major oxidant in the troposphere that determines the lifetimes of many chemical species. Ozone reacts with some gases, such as nitric oxide (NO), and with some surfaces, such as aerosols, leaves, and biological membranes. These reactions can damage living cells, such as those present in the linings of the human lungs. Exposure has been associated with several adverse health effects, such as aggravation of asthma and decreased lung function (Holgate et al., 2003).

An air parcel movement can be in three dimensions namely in the zonal or east – west direction which is caused by meridional temperature gradients (Holton, 2004), vertically, which is weaker than the zonal and meridional circulations in terms of mass flux and is generated by stratospheric wave forcing (Dessler, 2000), and meridionally (north-south) direction (Brasseur & Solomon, 2006).

The QBO refers to reversal in the direction of the zonal winds in the tropical stratosphere which at altitudes between 15 km and 30 km occurs on a timescale of 26 to 28 months. It is caused by the internal dynamics of tropical waves. The QBO also drives changes in temperature which can then change reaction rates and thus ozone amounts. The QBO also modifies the strength of the Brewer-Dobson circulation. When the QBO is in its easterly phase, planetary waves are refracted poleward creating a more disturbed and hence warmer polar vortex. The QBO also drives changes in temperature which can then change reaction rates and thus ozone amounts The QBO also modifies the strength of the Brewer-Dobson circulation. When the QBO is in its easterly phase, planetary waves are refracted poleward creating a more disturbed and hence warmer polar vortex.

A positive temperature gradient from pole to equator (cold to warm) causes westerly winds that strengthen with height, and vice versa. Atmospheric temperature can affect ozone in two ways. First, temperatures modulated photochemical reaction rates as detailed in reactions (1.1) to (1.4). Secondly, temperatures directly influence the circulation by amending the heating and cooling rates.

The predominant winds over the Nairobi and Kisumu cities are easterlies while south easterlies over Mombasa (Ongoma, Muthama, & Gitau, 2013). The easterly winds are generally stronger than the westerly winds and they persist for longer at upper levels (approx. 30 km altitude) and have maximum speeds centered over the equator near 26 km altitude.

Westerly winds descend faster than the easterlies and persists for longer at lower levels than the easterly winds. Below 30 km altitude in the tropical regions ozone is primarily under dynamical control and is therefore affected by the QBO-induced circulation, as well as the Brewer- Dobson circulation which has it's upwards branch over the equatorial region. Above 30 km altitude, ozone becomes increasingly under photochemical control and responds to the QBO-induced temperature changes rather than transport effects.

2.9 Ozone and Ultraviolet Radiation
Ozone's role as an ultraviolet (UV) filter is crucial in sustaining life in the biosphere. On average, less than 10% of the solar energy incident on the top of the Earth's atmosphere is in the UV spectral region (100-400 nm) (ACIA, 2005). While atmospheric oxygen (O_2) and ozone almost entirely absorb (referred to as UV-C radiation), (UV-B radiation) are absorbed efficiently but not entirely by atmospheric ozone. UV-B photons have enough energy to harm human beings, ecosystems and materials once they reach the Earth's surface (UNEP, 1998). UV-B photons can cause corneal damage, cataracts, immune suppression, aging of the skin, erythema and even break the bonds of DNA molecules (UNEP, 2003).

Generally, living cells are able to repair the damaged DNA, although sometimes the damaged DNA molecules can replicate which is the cause of dangerous forms of skin

cancer (Newman, 1998). UV-A radiations are absorbed by atmospheric ozone in small amounts compared to the UV-C and UV-B radiations. At the same time, UV-A radiations are low-energy photons compared to UV-C and UV-B photons, which makes them less harmful (ACIA, 2005).

2.10 Ozone Measurement

Measurements form the base on which our understanding of the atmosphere is built. Systematic measurement of stratospheric ozone commenced with the organization and operation of a network of ground-based instruments by G. M. B. Dobson (Dobson & Harrison, 1926), and has continued to the present day through a number of measurement techniques and platforms. Remote sensing measurements are made of the atmosphere located at a distance from the instrument. Remote sounding measurements can be made from the ground, from sub-orbital platforms such as balloons and aircraft, and from space-based platforms. Space-based measurements have the advantage of global (or near-global) coverage.

Total Ozone Mapping Spectrometer (TOMS) measures the total ozone content of the Earth's atmosphere. The instrument was first launched on the Nimbus 7 Spacecraft in 1978 followed by Meteor and Earth Probe. The nominal uncertainties of TOM's ozone data vary from 1 to 3%. (McPeters et al., 1993).

2.11 Ozone Depletion

In 1985, Farman et al., (1985) reported the first observations of the extreme decline in the Total Ozone Column (TCO) above Halley Bay, Antarctica. This phenomenon was named the ozone hole, and was seen in the springtime. TCO which declined from 320 DU (1 Dobson Unit (DU) is defined to be 0.01 mm thickness at STP) to less than 200 DU over the period 1979-1985. The results of Farman et al., (1985) were confirmed by TOM's satellite data, which showed that from September to November, the ozone depletion occurred over a much extended region of Antarctica (Stolarski, Krueger, Schoeberl, McPeters, Newman & Alpert, 1986; Solomon, 1986).

According to Rowland, (1991); WMO, (2002) and Welch, (2014), most O_3 destruction takes place through catalytic processes rather than "Chapman Reactions". Ozone is a

highly unstable molecule that readily donates its extra oxygen molecule to free radical species such as nitrogen, hydrogen, bromine, and chlorine. These compounds naturally occur in the stratosphere, released from sources such as soil, water vapor, and the oceans.

$$O_3 + X^\cdot \rightarrow XO + O_2 \tag{3.10}$$
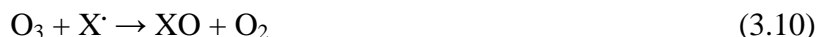
where $X^\cdot$ may be O, NO, OH, Br or Cl.

Considering anthropogenic destruction, manufactured compounds are also capable of altering atmospheric ozone levels. Chlorine, released from chloroflourocarbons (CFCs) and bromine (Br), released from halons, are two of the most important chemicals associated with ozone depletion. Halons are primarily used in fire extinguishers. CFCs are used extensively in aerosols, air conditioners, refrigerators, and cleaning solvents.

Two major types of CFCs are trichlorofluorocarbon ($CFCl_3$) or CFC-11, and dichlorodifluoromethane (CF_2Cl_2), or CFC-12. Trichlorofluorocarbon is used in aerosols, while dichlorodifluoromethane is typically used as a coolant. CFCs were originally created to provide a substitute for toxic refrigerant gases and to reduce the occupational hazard of compressor explosions.

Near earth's surface, CFCs are relatively harmless and do not react with any material, including human skin. While CFCs remain in the troposphere, they are virtually indestructible. They are not water soluble and cannot even be washed out of the atmosphere by rain. We now understand that the very quality that made them seem so safe –their stability – is what makes them so dangerous to the earth system. CFCs remain in the troposphere for more than 40 years before their slow migration to the stratosphere is complete through natural air motions transportation. Even if we were to end their production and their use at this very moment, they will continue to contribute to ozone destruction far into the future (Rowland, 2006; WMO, 2002; Space Physics course, 2011).

In the stratosphere, high energy UV radiation causes the CFC molecules to break down through photo dissociation (Reaction 3.11 and Reaction 3.12):

$$CFCl_3 + h\upsilon \rightarrow CFCl_2 + Cl \tag{3.11}$$

$$CF_2Cl_2 + h\upsilon \rightarrow CF_2Cl + Cl \tag{3.12}$$

Atomic chlorine, a true catalyst for ozone destruction, is released in the process. Chlorine initiates and takes part in a series of ozone-destroying chemical reactions and emerges from the process unchanged. The free chlorine atom initially reacts with an unstable oxygen containing compound (such as ozone) to form chlorine monoxide (ClO):

$$Cl^· + O_3 \rightarrow ClO^· + O_2 \qquad\qquad (3.13)$$

The ClO molecule then reacts with atomic oxygen to produce molecular oxygen (O_2) and more atomic chlorine. The regenerated Cl atom is then free to initiate a new cycle:

$$ClO^· + O^· \rightarrow Cl^· + O_2 \qquad\qquad (3.14)$$

This destructive chain of reactions will continue over and over again, limited only by the amount of chlorine available to fuel the process. Chlorine occurs naturally in the oceans; however, the majority of chlorine in the atmosphere has originated with man-made chemicals. Without the dissociation of manufactured chlorofluorocarbons, there would be almost no chlorine in the stratosphere (https://disc.gsfc.nasa.gov/ozone/additional/science-focus/aboutozone/ozone_cycle).

A combination of low temperatures, elevated chlorine and bromine concentrations in the upper stratosphere are responsible for the destruction of ozone as demonstrated by Welch (2014). The springtime Antarctic ozone hole has persisted, with minimum values around 100 DU, since the early 1990s (WMO, 2003). Seventy percent of the TCO was disappearing over the Antarctic by 1989 during the months of September and early October (Deshler, Adriani, Gobbi, Hofmann, Di Donfrancesco, & Johnson, 1992). Such loss means removal of 3% of the global ozone in a period of six weeks and shows how fast the state of the atmosphere can change (Anderson, Toohey & Brune, 1991).

Several studies (Angell, 1989; Labitzke & Van Loon, 1997; Isikwue, Agada, & Okeke, 2010) have shown increase in solar ultraviolet radiation with increase in sunspot number and also a more or less in phase variation of TCO with sunspot number. The relationship between ozone concentration and sunshine in Nigeria carried out by Obiekezie, (2009)

for a period 1997 – 2005 using linear regression analysis gave a significant negative correlation between the two parameters.

The linear regression analysis carried out by Rabiu (2003) to determine the relationship between solar activity and TCO variation in Lagos, Nigeria, showed a significant negative correlation between mean total column ozone and solar activity both at monthly level (r = -0.0652) and annual level (r = -0.2671), showing that the total column ozone decreases with increasing solar activity.

An investigation on the effects of extratropical suction pump (ETSP) and quasi-biennial oscillation (QBO) on the variability of ozone in Nigeria by Isikwue and Okeke (2009a) found that the mean ozone concentration for temporal oscillation period, average temporal amplitude of oscillation, and average maximum daily variation were 273.6 ± 0.04ˇDU, 7.81 DU, and 48.8 DU, respectively.

The average monthly maximum and minimum ozone concentrations were found to be 287.8 DU between July and August and 192.73 DU between December and March. These variations follow the trend of the zonal wind speeds obtained for Nigeria for the periods under investigation. Again, that ozone variation in Nigeria could be attributed to the effects of the ETSP action, which causes ozone transport from the tropical stratosphere to the mid-latitude region. Furthermore, QBO effect on ozone variability was observed in February 2001, January 2003, and January 2004.

Isikwue et al., (2010) performed a multiple regression analysis in their study on the contribution of solar activity indices on the stratospheric ozone variations in some cities in Nigeria from 1998 – 2005 and obtained a positive significant correlation (r = 0.622 at 95% level of significance) between sunspot numbers and ozone concentration and negative non- significant correlation between Mg II core to wing ratio and ozone concentration.

A statistical relationship (Pearson product moment correlation coefficient) between surface ozone and solar activity in a tropical rural site on the east coast of south India

(1996 - 2004) investigated by Selvaraj, Gopinath and Jayalakshmi (2010), found a high positive rank correlation coefficient of 0.76 and 0.62 obtained for the years 2000 and 2002 respectively indicating the influence of higher solar activity over the surface ozone levels.

2.12 Ozone Modeling and Forecasting

Biological and environmental systems have been historically very difficult for scientists and engineers to model effectively. This could have been due to the large number of variables involved and the complex way in which they interact. Researchers look to create models so as to accurately map the input variables to the output variables as is observed in real life situation and to be able to fit representations of a system to its underlying physical characteristics.

Mathematical models have traditionally been developed from either physical principles or by statistical regression (Salas, Markus & Tokar, 2000). Physical models consist of systems of ordinary or partial differential equations. These models try to represent the underlying physical relationship between the variables involved. The benefit of physical models is that they are based on a deep and thorough understanding of the system. The limitation of these models include the difficulty of setting up and solving complex differential equations analytically, as well as determining equation coefficients and initial and boundary conditions (Coppola, Rana, Poulton, Szidarovszky & Uhl, 2005).

Statistical models on the other hand are designed by finding the equation that best fits a set of historical or experimental data. These models are useful in that they are generally simple and straightforward to solve. Statistical regressions limit the user by requiring a large amount of sample data to estimate the parameters of the equation and to find the data trend.

2.13 Artificial Neural Networks Background and History

The limitation of regression equations and partial differential equations led researchers to explore alternative models. One that has become popular over the last decade is the

artificial neural network (ANN) (Govindaraju, & Rao, 2000). ANNs are a type of model that was first conceptualized in 1943 by McCulloch and Pitts (Anderson, 1995). ANNs were designed based on biological neurons and how neurons interact with each other in the brain. McCulloch and Pitts (1943) started with the concept of a perceptron, which is a single artificial neuron (Figure 2.1)
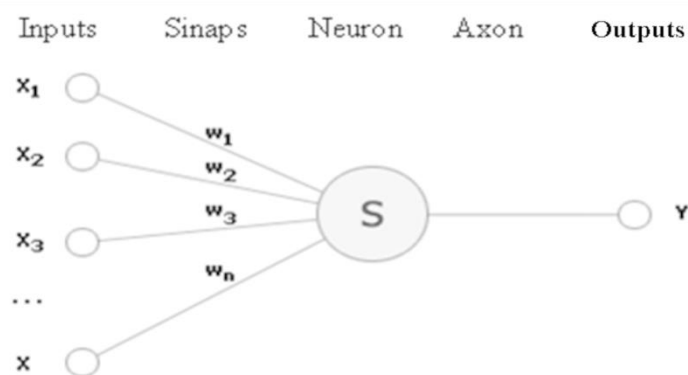
Figure 2.1 A single artificial neuron, also known as a perceptron

The node itself is similar to the cell body, and the connections made to other nodes represent the axon and synapses (Mehrotra, Mohan & Ranka, 1997).

This artificial neuron, commonly referred to as a node, is analogous to a biological neuron (Figure 2.2)
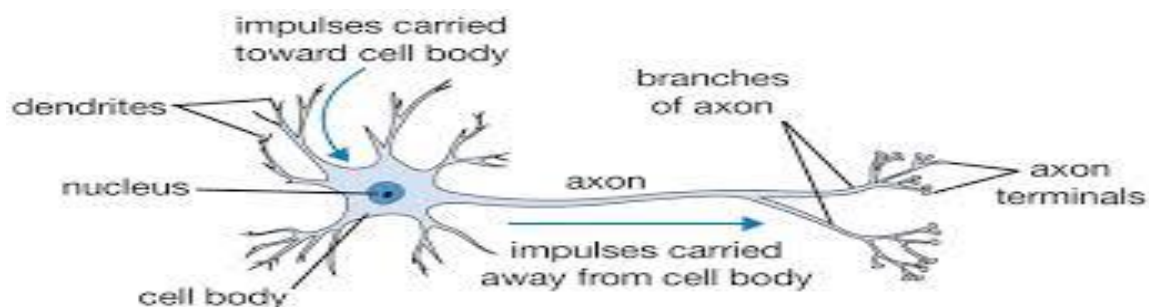
Figure 2.2 A single biological neuron

2.14 The Multilayer Perceptron

Artificial Neural Networks (ANNs) in the form of Multilayer Perceptron (MLP) (Rojas, 1996; Gardner & Dorling, 1998) is a feed forward ANN model that maps sets of input data onto a set of appropriate output. MLP utilizes a supervised learning technique called back propagation for training the network (Wikipedia 2012 from http://en.wikipedia.org/wiki/Multilayer_perceptron).

Gardner (1996) used the neural network to investigate the importance of local meteorology in determining the surface ozone concentration on an hourly basis. The purely meteorological input data were hourly observations of temperature, humidity, irradiance, wind speed, direction and ozone concentrations for an entire year. No chemical data was involved as input to the model. The model showed that over a period of a year, 48% of the ozone variation could be attributed to changing meteorological conditions. Any remaining variability was attributed to other causes such as chemical interaction between hydrocarbons and oxides of nitrogen.

Abdul-Wahab and Al-Alawi (2002) developed an ANN model using environmental pollutants (CH_4, NMHC, CO, CO_2, NO, NO_2, and SO_2) and meteorological variables (wind speed and direction, air temperature, relative humidity, and solar radiation) as predictors. They observed that the contribution of meteorology on the ozone concentration dropped within the range $31.15 - 40.64\%$. They also found that nitrogen oxide, sulfur dioxide, relative humidity, non-methane hydrocarbon and nitrogen dioxide have the most effect on the predicted ozone concentrations. In addition, temperature played an important role while solar radiation had a lower effect. Hence the results of their study indicated that the artificial neural network (ANN) is a promising method for air pollution modeling.

Crowe and DeFries (1996) applied neural networks to predict ozone concentrations in southeast Texas, near Houston. The input data consisted of hourly meteorological parameters, nitrogen oxides and seven hydrocarbon species based on carbon bond four chemistry. Three neural network models were developed. The predictor variables for the

first model consisted of five meteorological parameters for the same hour as the ozone measurement and also for six time delays to account for possible effects of transport and chemical reactions. The second model consisted of the same meteorological variables but included the species NO and NOx.

The third model dropped the time-lagged variables but added seven hydrocarbon species based on carbon bond four chemistry. The models showed progressively better predictive capability as evidenced by increasing the coefficient of determination values from 0.7 (first model) to 0.8 (second model) to 0.91 (third model). The authors reported that selected hydrocarbon species are more sensitive predictors of hourly ozone. They found that increasing olefins were associated with decreasing ozone and that increasing paraffin concentrations were associated with sharply increasing ozone levels.

Capone (1996) applied neural network technology to predict downwind hourly ozone data in the Baton Rouge area in the USA by using a more complicated network in which data from two downwind sites were employed as predictors. The model, which consisted of hourly meteorological and NO_x measurements at each site, was successful at predicting hourly ozone patterns. The Capone model did not involve any hydrocarbon species.

A study by the University of Arizona (Comrie, 1997) used data from eight cities around the United States to compare regression models and neural networks under a variety of climate and ozone regimes. The ozone data used were the daily maximum one-hour concentrations for the months of May through September over a five year period. A comparison between the two methods indicated that neural network techniques are somewhat (but not dramatically) better than regression models for daily ozone prediction.

Elkamel, Abdul-Wahab, Bouhamra and Alper (2001) illustrated the successful use of a neural network to predict ozone concentrations using both meteorological and chemical data. The network was trained using data collected near an industrial area in Kuwait for a period of 60 days. The performance of the neural network model was compared

against linear and non-linear regression models. The study indicated that neural network models consistently gave better predictions.

Gardner and Dorling (2000) established artificial neural networks (ANN) as an alternative to multiple linear regression to forecast surface ozone on the basis of meteorological data. Wang, Lu, Wang and Leung (2003) combined statistical approaches with ANN in forecasting maximum daily ozone level. In their work, they considered wind speed, wind direction, outdoor temperature, solar radiation, and indoor temperature as meteorological predictors in the development of an ANN model for forecasting daily maximum ozone concentrations on the basis of three air pollutant-monitoring stations in Hong Kong during 1999 and 2000.

Predictions from ANN were proven more accurate when contrasted with applied linear high ozone regression analysis techniques (Chelani, Rao, Phadke & Hasan, 2002) and regression models (Gardner & Dorling, 1999). Several researchers (Sousa, Martins, Alvim-Ferraz & Pereira, 2007; Chaloulakou, Saisana, & Spyrellis, 2003; Comrie, 1997), in forecasting the surface ozone concentration, compared the performance of ANN with the conventional regression method and indicated that ANNs provided better estimates of ozone concentrations than the more often used linear models which were less efficient at accurately forecasting concentrations.

The application of ANN in forecasting tropospheric ozone is available but the application of ANN in modeling and forecasting TCO, which is characterized by extensive non linearity and complexity, is not so frequent (Chattopadhyay & Chattopadhyay, 2010; Chattopadhyay & Chattopadhyay, 2008)

Sanz and Marqués (2004) attempted ANN in studying total ozone time series over some urban areas of Europe. They presented several models based on neural networks that filled the missing periods of data within a total ozone time series, and the models were able to reconstruct the data series. The results released by the ANNs were compared with those obtained by using classical statistics methods, and better accuracy was

27

achieved with the nonlinear ANNs techniques. Different network structures and training strategies were tested depending on the specific task to be accomplished.

Implementation of ANN in modeling TCO by Chattopadhyay and Chattopadhyay (2009) was made in a multivariate environment where the prediction of TCO was based on meteorological parameters or the past values of TCO time series. In their studies based on univariate approaches Chattopadhyay and Chattopadhyay (2009); Chattopadhyay, Chattopadhyay and Jain (2010), autoregressive ANN models generated were compared with autoregressive moving average and autoregressive integrated moving average models. An autoregressive AR (p)) and autoregressive moving average (ARMA (p, q)) were generated with 3 and 1 as the best values of p and q respectively. An autoregressive neural network (AR-NN (3)) was generated by training a generalized feedforward neural network (GFNN). An assessment of the model performances by means of Willmott's index of second order and coefficient of determination showed that the performance of AR-NN(3) was identified to be better than AR(3) and ARMA(3,1).

In all the aforesaid works ANN models have been developed with meteorological variables as predictors. In Bandyopadhyay and Chattopadhyay (2007) approach, instead of tropospheric ozone, total ozone has been considered as a predictand and instead of incorporating other meteorological variables, past values of total ozone time series have been explored in developing ANN predictive models.

In this study, TCO has been considered as a predictand and instead of incorporating past values of TCO time series, meteorological variables, or environmental pollutants and/or chemical data, three solar activity indices (SAI) variables representing the different spheres of the sun namely the sunspot numbers (photosphere), Mg II core to wing ratio or Mg II index (chromosphere) and F10.7 cm solar radio flux or F10.7 index (corona) are explored in developing both linear (MLR) and nonlinear (ANN) predictive models to predict TCO at Nairobi, Kisumu and Mombasa. The performance of the developed models will also be evaluated and then compared using statistical parameters namely Pearson correlation coefficient, (Wilks, 2011), Root Mean Square Error, Mean Absolute

error (Wilks, 2011), Percentage error of prediction (Pérez, Trier & Reyes, 2000), Willmott's Index of agreement (Willmott, 1982).

CHAPTER THREE

THEORETICAL CONSIDERATIONS

3.1 Introduction

In this chapter, an introduction to the structure of the Sun, its source of energy and radiation emitted are provided. It also covers the solar variability origin and gives a phenomenological survey of its different aspects. The concept of solar activity is discussed along with an overview of the solar parameters used to quantify different aspects of variable solar activity, with special emphasis on the solar parameters used in this study; sunspot number, Mg II core to wing ratio and F10.7 cm solar radio flux. The Earth's atmosphere beginning with the outer most sphere (the Exosphere) to the sphere next to the Earth's surface (the troposphere) is briefly discussed stating the various activities that occur within each one of them.

3.2 The variable Sun

The Sun, the central celestial body of our planetary system, is the only star close enough to observe details on its surface from the Earth. The Sun is a star of intermediate size and luminosity. The analysis of both solar radiation emission and the surface feature observations gives an insight into the chemical composition and the physical processes inside the Sun.

The Sun is a gaseous sphere consisting of 92.1% hydrogen, 7.8% Helium, 0.061% oxygen, 0.030% carbon, 0.0084% Nitrogen, 0.0076% neon, 0.0037% iron, 0.0031% silicon, 0.0024% magnesium and 0.0015% sulfur (Hoyt & Schatten, 1997). The gas pressure within the Sun decreases from the centre to the surface and is balanced by the hydrostatic pressure caused by the gas' own weight. Table 3.1 gives a summary of some of the Sun's fundamental properties.

Table 3.1 The fundamental properties of the Sun (Hoyt & Schatten, 1997)

Properties	value and units
Radius	6.960×10^5 km
Mass	1.989×10^{30} kg
Average density	1.41 g/cm^3
Effective surface temperature	5.780×10^3 K
Luminosity	3.85×10^{26} W
Average distance from the Earth	1.496×10^8 km

It is possible to deduce a model for the Sun's interior, in particular the distribution of pressure, temperature and energy transport based on the knowledge of its radius, surface temperature, luminosity, mass and the chemical composition of the outer layers.

The Sun (Figure 3.1) consists of a solar interior (core); $r < 0.23$ R$_\odot$ (where R$_\odot$ is the solar radius) with 40% mass of Sun and 15% of volume. 90% of energy is generated here. The temperature is approximately 8.40×10^6 K and 10^5 kg/m^3 density. The core is surrounded by a radiator or a radiative zone (0.23 R$_\odot < r < 0.7$ R$_\odot$), where the temperature drops. The convective zone is 0.7 R$_\odot < r < $ R$_\odot$. The temperature is 130,000 K and density 70 kg/m^3 (Solar structure, via http://www.columbia.edu; Stix, 2012).

The boundary of the solar radius R$_\odot$ is the outer layer of the convective zone (the photosphere) Figure 3.1. The Sun's surface, called the photosphere is visible from the Earth. It is a very thin layer which is only a few hundreds of kilometers thick. The chromosphere is the adjacent layer above the photosphere, bordering the corona. These

two are visible only during the total solar eclipse or with the aid of a coronagraph (simulating a total eclipse) hence blocks the direct sunlight.

3.2.1 Luminosity ($L_\odot$)

The average radiation power density of sunlight outside the atmosphere of Earth, the solar constant, is S = 1366 W/m^2. The average distance between the Sun and Earth, the astronomical constant, is $A_\odot$ = 1.5 × 10^{11} m. The luminosity of the Sun, or the total power of solar radiation, is given by Equation 3.1:
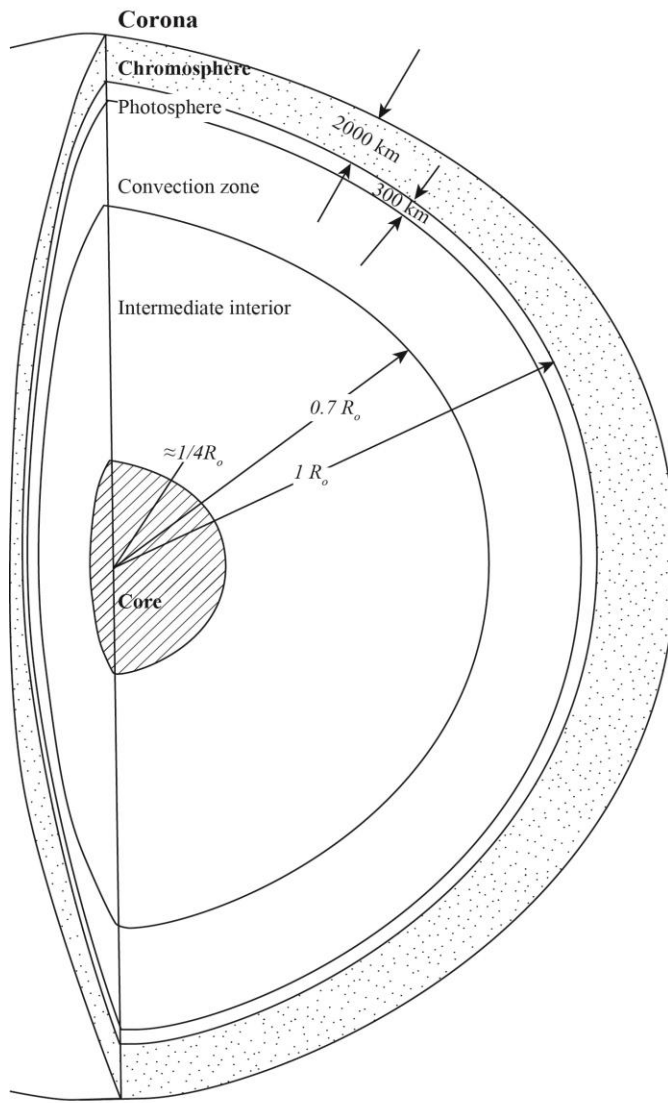
Figure 3.1 Schematic illustration of the Sun's structure (Brasseur & Solomon, 2006)

$$L_\Theta = 4\pi A_\Theta{}^2 S \tag{3.1}$$

Luminosity can also be given in terms of effective temperature as in Equation 3.2

$$L_\Theta = 4\pi R_\Theta{}^2 \sigma T^4 \tag{3.2}$$

where σ is the Stefan – Boltzmann constant

3.2.2 Irradiance and Energy Flux

The solar irradiance S (λ), Equation 3.3, is the energy flux observed at a given distance (in our case 1 AU) per unit area, time, and wavelength interval. It is related to the energy flux F (λ) at the solar surface simply by

$$S(\lambda) = R_\Theta{}^2 \, F(\lambda) \tag{3.3}$$

3.2.3 Radio Spectrum

Radio wavelengths are longer than 1 mm. Instead of wavelength, frequency is often used to characterize the emissions. Equation 3.4 gives the conversion formula.

$$\lambda \, (m) = 300 \, / \, f \, (MHz) \tag{3.4}$$

Equation 3.4 presents the solar radio emissions in terms of flux per frequency interval.

3.2.4 Emission Power (U_Θ)

Equation 3.5 gives the emission power of the surface of the Sun, in watts per square meter.

$$U_\Theta = L_\Theta \, / \, 4\pi R_\Theta{}^2 \tag{3.5}$$

3.2.5 Surface Temperature (T_Θ)

Considering the Sun as a blackbody, the temperature can be calculated from Equation 3.6 which is the Stefan Boltzmann law.

$$T_\Theta = (U_\Theta /\sigma)^{¼} \tag{3.6}$$

3.2.6 Interaction of Radiation with Matter

Part of the radiation falling on a piece of matter is absorbed, another part is reflected, and the rest is transmitted. Three dimensionless coefficients are introduced: absorptivity $A(\lambda)$, reflectivity $R(\lambda)$, and transmissivity $T(\lambda)$. Conservation of energy requires that

$$A(\lambda) + R(\lambda) + T(\lambda) = 1 \tag{3.7}$$

For opaque surfaces, the transmittivity is zero. Conservation of energy requires that incident radiation be either absorbed or reflected,

$$A(\lambda) + R(\lambda) = 1 \tag{3.8}$$

3.2.7 Energy Transport

The energy flux F is, by definition, the luminosity per unit area. Energy transport by radiation (F_R) and convection (F_C) is given as Equation 3.9

$$F = F_R + F_C = L /4\pi R^2 \tag{3.9}$$

Solar energy within the core is generated by fusion reactions forming helium from hydrogen atoms. Each hydrogen atom weighs 1.0078 atomic mass unit (amu) and each He atom weighs 4.0312 amu. During the fusion process a mass defect or an excess mass of 0.0282 amu above the He atom of 4.003 amu is converted into energy, E according to Einstein formula in Equation 3.10

$$E = mc^2 \tag{3.10}$$

Where, c is the velocity of light.

 It is assumed from model calculations that the temperature in the core region ranges from 13.0×10^6 to 15.5×10^6 K and the pressure from 2.10×10^{16} to 3.0×10^{16} Pa.

Hence the gases are highly ionized, that is; the electrons are removed from the atoms forcing plasma of nuclei, protons (hydrogen nuclei) and electrons.

The two essential pathways for the fusion process include the proton – proton (p-p chain) and the Carbon, Nitrogen and Oxygen (CNO) cycle. In the p-p chain fusion process, helium is formed from four protons (Reaction 3.1, 3.2 and 3.3) and takes place at temperatures above 5 x 10^6 K.

$$^{1}_{1}H + {}^{1}_{1}H \rightarrow {}^{2}_{1}D + e^{+} + v_e + 10.164\ MeV \tag{3.1}$$

$$^{2}_{1}D + {}^{1}_{1}H \rightarrow {}^{3}_{2}He + \gamma + 5.49\ MeV \tag{3.2}$$

$$^{3}_{2}He + {}^{3}_{2}He \rightarrow {}^{4}_{2}He + {}^{1}_{1}H + {}^{1}_{1}H + 12.85\ MeV \tag{3.3}$$
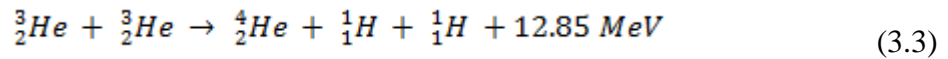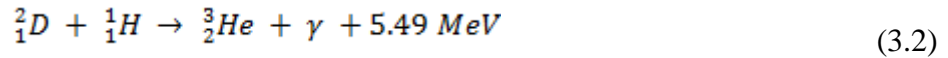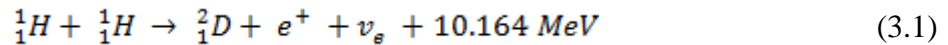
Where e^{+} is a positron (an elementary particle with mass of an electron but positively charged, v_e is an electron neutrino, a particle that escapes from the Sun immediately due to the very weak interaction with other matter and γ is the Gamma radiation. $^{2}_{1}D$ denoted deuterium, an isotope of hydrogen, the nucleus of which contains one neutron in contrast to $^{1}_{1}H$.

Reaction 3.1 rarely happens due to the high kinetic energy that is required to overcome the coulomb repulsion of the two positively charged protons. The low rate of this reaction determines the time scale for the entire chain.

The CNO cycle (also known as the Bethe – Weizsacker cycle) fusion process involves heavier elements. The carbon acts as a catalyzer.

$$^{1}_{1}H + {}^{12}_{6}C \rightarrow {}^{13}_{7}N + \gamma + 1.95\ MeV \tag{3.4}$$
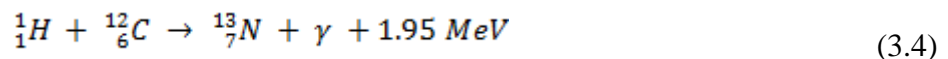
$$^{13}_{7}N \rightarrow {}^{13}_{6}C + e^{+} + \nu_{e} \ 1.50 \ MeV \tag{3.5}$$

$$^{13}_{6}C + {}^{1}_{1}H \rightarrow {}^{14}_{7}N + \gamma + 7.54 \ MeV \tag{3.6}$$

$$^{14}_{7}N + {}^{1}_{1}H \rightarrow {}^{15}_{8}O + \gamma + 7.35 \ MeV \tag{3.7}$$

$$^{15}_{8}O \rightarrow {}^{15}_{7}N + e^{+} + \nu_{e} + 1.73 \ MeV \tag{3.8}$$

$$^{15}_{7}N + {}^{1}_{1}H \rightarrow {}^{12}_{6}C + {}^{4}_{2}He + 4.96 \ MeV \tag{3.9}$$

This cycle proceeds faster than the p-p chain but require higher temperatures to operate than the p-p chain. It becomes the dominant source of energy at temperatures above 20 x 10^{6} K. As the core temperature of the Sun is about 15.5 x 10^{6} K, the CNO cycle only contributes a minor part of the solar energy production. The released energy fusion for both types of fusion amounts averagely to 25.6 MeV (Koskinen, 2011). With the Sun's given luminosity of 3.85 x 10^{26} W (Table 3.1), it is estimated that about 9.4 x 10^{37} fusion processes happens every second.

The energy produced in the core region is transported by radiation through the radiation zone and subsequently by convection through the convective zone. Due to interactions of photons with matter, the radiative energy transport proceeds relatively slowly on a time scale of the order of 10 million years. At a depth of about 150,000 km below the surface, a steep temperature gradient develops as a result of a lower ionization rate. A dynamic equilibrium is established where ions capture electrons and electrons are again removed from atoms at the same rate. In particular, the removal of electrons happens by photoionization i.e. the protons ascending from the radiative zone are strongly absorbed in this layer. Radiative processes are no longer sufficient to maintain a thermal equilibrium. Hence, convection replaces radiation as the primary energy transport process. The convective zone borders the photosphere (Koskinen, 2011; Kubin, 2011)

3.2.8 The Photosphere

The photosphere, meaning the 'light sphere', constitutes the Sun's surface as seen from the Earth. It has a temperature of 5000 K and a density of 10^{-5} kg/m^3. It denotes the region of the Sun where photons can finally escape into space and probably reach the Earth's atmosphere. The photosphere is only about 200 – 400 km thick, which is very thin compared to the Sun's radius of about 700,000 km. It is the source of most radiation. The photosphere is composed of 73.5% hydrogen, 25% helium, 1.5% oxygen and carbon (The structure of the Sun, via http://www.cs.berkeley.edu).

Photons reaching the Earth originate from different depths inside the photosphere. This is due to the limited free path length (FPL) in the layer. Photons from the bottom of the photosphere near the limb of the solar disc cannot escape towards the Earth. They are absorbed within the photosphere. Hence the light from the limb is emitted in outer, cooler regions of the photosphere which is the reason for the limb darkening of the Sun (Koskinen, 2011)

At the centre of the solar disc, the FPL is sufficient to allow photons from deeper and hotter regions of the photosphere to escape into space towards the Earth which makes the Sun appear brighter at the centre. Therefore the temperature of the photosphere is estimated at 7000 K at the bottom and 4600 K at the top (Kubin, 2011). The Sun's surface appears granulated (irregular convective cells) not even. These granules are about 1,000 to 3,000 km in dimension.

The granules are formed by the ascending and descending motion in the convective zones. They have a life time of the order of 10 minutes and a horizontal extent of about1000 km. The so called supergranules are much larger, with diameters of about 35,000 km. They are observed by the Doppler shift where higher frequencies (blue shift) indicate upwelling while lower frequencies (red shift) indicate downwelling. The life time of the super granules is of the order of a day. The edges of supergranules form the so called Networks (Lang, 2008; Kubin, 2011).

A close inspection of the continuous solar spectrum reveal a number of dark lines referred to as Fraunhofer lines. These lines emerge when light is transmitted through a gas. At certain wavelengths that correspond to the difference of two energy levels of an arbitrary element, the photon is absorbed. At a radiative equilibrium, the absorbed radiation has to be reemitted.

The emission occur isotroply, that is, with no preferential direction. This implies that the incident radiation directed towards the Earth is attenuated but not completely extinguished. There is a rest intensity in each absorption line. Fraunhofer absorption lines provide information about the composition of the solar atmosphere but not about the abundance of individual species. They also contain more information about the physical condition such as pressure and temperature in different layers of the photosphere (Kubin, 2011).

3.2.9 The Chromosphere

The chromosphere appears above the photosphere (Figure 3.1). The name 'chromosphere' means literally 'color sphere'. Literature gives different thickness of the chromosphere ranging from 1800 km to 3000 km (Lean, 1997). The light intensity is 10^5 times lower than that of the photosphere near the limb hence the chromosphere is outshined by the photosphere. It is characterized by an emission line spectrum dominated by the He_α line (656.3 nm) of hydrogen. The spectral lines of helium were first discovered in chromospheric spectrum in 1868 but they are not present in the photospheric light due to the temperature and hence energy not being sufficiently high for an excitement.

The temperature in the chromosphere slowly rises with altitude and then increases rapidly in a thin region which forms the transition to the corona. Simultaneously, the density decreases with altitude over several orders of magnitudes. It is assumed that sound waves generated in the convective zone are responsible for the steep temperature gradient in the upper most layers of the chromosphere. These waves propagate upwards and deposit their energy as their amplitudes increase with decreasing density thus

heating the surrounding area. At a height of about 1500 km above the photosphere'
luminous gases languets seem to grow like grass blades (spiculae) and are part of
chromospheric network. Spiculae are clustered in regions that can be identified by the
edges of photospheric supergranules thus forming the mesh of the network (Lean, 1997;
The structure of the Sun, via http://www.columbia.edu).

3.2.10 The Corona

The corona literally means 'crown'. The corona constitutes the outer atmosphere of the
Sun. From terrestrial observations during total solar eclipses or with coronagraphs, it can
be traced to five solar radii above the Sun's surface. Space borne measurements reveal
an extent up to 50 solar radii above the surface of the Sun. The temperature within the
corona reaches values of the order of magnitude of $1 - 2$ x 10^6 K. The coronal light can
be divided into three fractions namely; K- corona (continuously), E- corona (emission
lines) and F- corona (Fraunhofer) (Zeilik, Gregory & Smith, 1998).

The K- corona dominates up to 0.3 solar radii with a sharply decreasing intensity above.
It is generated by scattering of photospheric light at free electrons. The absence of
Fraunhofer lines in K- corona can be explained by Doppler broadening due to the high
kinetic energies of the free electrons owing to the high temperature. The E- corona is
superposed to the continuous spectrum of the K- corona at altitudes up to 0.5 solar radii.
It contains about 30 emission lines in the visible part of the spectrum. The strongest
optical emission line is found at 530.3 nm. Beyond the visible, the E- corona spectrum
extends to the extreme ultra violet and over to X- ray wavelength. The F- corona has got
nothing to do with the Sun, but arises from scattering of photospheric light at inter
planetary dust. It is observed at heights exceeding 1.5 solar radii above the photosphere
(Zeilik, Gregory & Smith, 1998; Kubin 2011).

Corona is the source of radio waves which are generated as bremsstrahlung when free
electrons change direction or speed in the electrostatic field of ions. The shape of the
corona varies with solar activity. In quiet periods, long rays of light near the equator and

shorter rays near the poles are observed whereas the rays point radially outwards and are more evenly distributed at periods of high solar activity (Nag & Das, 2007).

3.3 Solar Variability

The Sun is variable on a broad range of temporal and spatial scales. On the temporal scale, variations are observed with periodicities of about 27 days, which is, the average period of the Sun's rotation around its axis or 11 years, which is, the period in which the number of sunspots waxes and wanes. The manifestations of these two in the Earth atmosphere are subject to this study (Lean, 1997).

The Sun radiates a large part of its energy in the visible and infra- red domain with the maximum located at about 500 nm. Above approximately 300 nm, the Sun's radiation emission resembles that of a black body at a temperature of about 5770 K (Lean, 1997). Other authors specify higher temperatures for the equivalent black body radiation; 5780 K or 5900 K (Brasseur & Solomon, 2006).

Total solar irradiance (TSI) is defined as the integral of solar irradiance over all wavelengths. It was earlier denoted the 'solar constant' which is misleading as the TSI is variable in time. The average value of TSI is approximately 1365 Wm^{-2} (Frohlich and Lean, 2004). This is the radiation incident on an imaginary plane perpendicular to the rays at the distance of 1 AU (= 1.496 x 10^{11} m). It is, however the radiation incident at the top of the atmosphere and not on the earth's surface. Absorption, scattering and reflection attenuate the incident radiation in the Earth's atmosphere so that only a fraction amount reaches the surface. The total solar irradiance is measured from satellites outside the Earth's atmosphere.

3.4 Solar Irradiance Variation

The Sun spectrum is not uniformly affected by solar activity. When spectrally resolved, the solar output is most variable at wavelengths that are much shorter or considerably larger than that of irradiance in visible at about 500 nm, in the ultraviolet (UV) to X-rays range and respectively at radiofrequencies. The amplitude of irradiance change between

solar maximum and minimum at 250 nm is 3%, at 200 nm is 8% and at the Lyman alpha line (121.5 nm) it is 50 to 100%. In the near UV, the visible and the infra red part of the spectrum, sunspot darkening and faculae brightening modulate the solar irradiance. At wavelengths shorter than 300 nm, that is, in the UV, the enhanced emission from faculae and plages dominates solar variability. The influence of the dark spots arises with increasing wavelengths.

A large fraction of the solar variability is driven by the magnetic field. The magnetic fields of the Sun, (and also all astronomical bodies), are produced by a process called the hydromagnetic dynamo process (Parker, 1955). This hydromagnetic dynamo process can build up a magnetic field within the Sun starting from an initial field. If a magnetic field is present in the region where plasma blobs (which are good conductors of electricity) are rotating, then Faraday's law generalized to a continuum situation suggests that an e.m.f. can be induced within a rotating plasma blob. Under favorable circumstances, this e.m.f. can reinforce the magnetic field present in the Sun (Choudhuri, 1998).

Since all stars form from interstellar gas clouds which seem to have magnetic fields, then it is assumed that there must have been some weak initial field on which the stellar dynamo could have started operating. Solar dynamo theory, is study on how the dynamo process sustains the solar magnetic field in the form in which it is found today, hence a consideration on the dynamics of the plasma inside the Sun is needed so as to understand how the solar dynamo operates (Choudhuri, 2007).

The Sun has a cycle with twice a period of about 11 years, i.e. 22 year. This is due to the fact that the Sun's magnetic field changes its direction after 11 years; it takes 22 years for the magnetic field to come back to its initial configuration.

3.5 Basics of Magneto – hydrodynamics (MHD)

Plasma is a collection of neutral atoms, positively charged ions and negatively charged electrons; it can also be regarded as a continuum fluid while discussing many problems in plasma dynamics. The branch of plasma physics in which the plasma is treated as a

continuum fluid is called magneto - hydrodynamics, abbreviated as, MHD. Studies on non-relativistic ($|v| \ll c$) bulk motions of the plasma under the influence of gravitational and magnetic forces and for almost all problems related to the dynamics of plasma underneath the Sun's surface, MHD provides the appropriate theoretical framework (Choudhuri, 1998; Choudhuri 2007).

Due to the electrical attraction between positive and negative charges in plasma, these opposite charges usually remain very well mixed. In other words, the positive and negative charges almost exactly balance each other. This does not mean that a volume element of plasma is exactly like a volume element of an ordinary non-ionized gas. The main difference is that, an ordinary non-ionized gas is a bad conductor of electricity. On the other hand, it is possible for the electrons and ions in plasma to move systematically with respect to each other, thereby giving rise to a current, even though volume elements of the plasma remain charge-neutral. Hence, in MHD plasma is regarded as a special kind of fluid which is a very good conductor of electricity and since volume elements of the plasma remain charge-neutral, large-scale electric fields in the plasma is not expected. But currents flowing through the plasma can give rise to large-scale magnetic fields (Choudhuri, 2007; Priest, 1982).

One combines Maxwell's equations with the equations of fluid mechanics to derive the basic equations of MHD. Here some of the basic equations are given and their significance discussed. The velocity field, **v** and the magnetic field, **B** in plasma interact with each other according to the following MHD equations:

$$\frac{\partial \mathbf{v}}{\partial t} + (\mathbf{v} . \nabla)\mathbf{v} = -\frac{1}{\rho} \nabla \left(p + \frac{B^2}{2\mu} \right) + \frac{(\mathbf{B} . \nabla) \mathbf{B}}{\mu \rho} + \mathbf{g} \qquad (3.11)$$

$$\frac{\partial \mathbf{B}}{\partial t} = \nabla \times (v \times \mathbf{B}) + \lambda \nabla^2 \mathbf{B} \qquad (3.12)$$

Here ρ is density, p is pressure, g is gravitational field and

$$\lambda = \frac{1}{\mu \sigma} \qquad (3.13)$$

Equation 3.13 is called magnetic diffusivity (σ is electrical conductivity). Equation 3.11 is essentially the Euler equation of fluid mechanics, to which magnetic forces have been added. From Equation 3.11, the magnetic field has two effects: (i) it gives rise to an additional pressure $\frac{B^2}{2\mu}$; and (ii) the other magnetic term $\frac{(\mathbf{B}.\nabla)\,\mathbf{B}}{\mu\rho}$ is of the nature of a tension along magnetic field lines.

Equation 3.12 is the key equation in MHD and is called the induction equation, because Faraday's law of electromagnetic induction is incorporated within it. If V, B and L are the typical values of velocity, magnetic field and length scale, then the first term on the right hand side of Equation 3.12 is the convection term, The convective term involves the plasma motion from which new flux is generated. The second term ($\lambda\nabla^2\mathbf{B}$) is the diffusion term and it describes how the field is diffused away. If the convection term and diffusion terms are of order V B/L and λ B/L^2 then, the ratio of these two terms is a dimensionless number, known as the magnetic Reynolds number, given by Equation 3.14

$$R_m \;=\; \frac{VB/L}{\lambda B/L^2} \;=\; \frac{VL}{\lambda}$$

(3.14)

Since R_m goes as L, it is expected to be much larger R$_m$ » 1 in astrophysical situations. Then the diffusion term in Equation 3.12 is negligible compared to the term preceding it. In such a situation, it can be shown that the magnetic field is frozen in the plasma and moves with it. This result was referred to as Alfven's theorem of flux-freezing. It is known that the Sun does not rotate like a solid body. The angular velocity at the equator is about 20% faster than that at the poles. Because of the flux freezing, this differential rotation would stretch out any magnetic field line in the toroidal direction (i.e. the Ø direction with respect to the Sun's rotation axis). It is, therefore, expected that the magnetic field inside the Sun may be predominantly in the toroidal direction (Tobias, 2002).

To understand why the magnetic field remains concentrated in structures like sunspots instead of spreading out more evenly, a study on magneto - convection (the interaction of the magnetic field with the convection in the plasma) is needed. The linear theory of convection in the presence of a vertical magnetic field was studied by Chandrasekhar (1952). It was found that space gets separated into two kinds of regions. In certain regions, magnetic field is excluded and vigorous convection takes place. In other regions, magnetic field gets concentrated, and the tension of magnetic field lines suppresses convection in those regions (Choudhuri, 2007).

Although there is no direct information about the state of the magnetic field under the Sun's surface, it is expected that the interactions with convection would keep the magnetic field concentrated in bundles of field lines throughout the solar convection zone. Such a concentrated bundle of magnetic field lines is called a flux tube. In the regions of strong differential rotation, therefore, there may exist the magnetic field in the form of flux tubes aligned in the toroidal direction. If a part of such a flux tube rises up and pierces the solar surface then two sunspots with opposite polarities are expected at the same latitude.

In Equation 3.11, pressure $\dfrac{B^2}{2\mu}$ is associated with a magnetic field. If p_{in} and p_{out} are the gas pressures inside and outside a flux tube, then to maintain pressure balance across the surface of a flux tube

$$P_{out} = P_{in} + \frac{B^2}{2\mu}$$

(3.15)

Hence;

$$P_{in} \leq P_{out}$$

(3.16)

which often, though not always, implies that the density inside the flux tube is less than the surrounding density. If this happens in a part of the flux tube, then that part becomes

buoyant and rises against the gravitational field (Tobias, Brummell, Clune & Toomre, 2001; Choudhuri, 1998; Choudhuri, 2007).

Therefore, combining the ideas of flux freezing, magneto - convection and magnetic buoyancy, aspects of the bipolar sunspot pairs can be understood. Flux freezing tells us that the magnetic field in the interior of the Sun should be stretched in the toroidal direction by differential rotation. Magneto-convection calculations suggest that the magnetic field should exist in the form of flux tubes within the convection zone and finally, idea of magnetic buoyancy is used to explain how bipolar sunspots arise (Choudhuri, 2007).

Since the toroidal field is generated by the stretching of the poloidal field by differential rotation, the strongest toroidal fields are expected to be generated in the regions where differential rotation (i.e. the gradient of angular velocity) is strongest. There is this thin layer called tachocline at the bottom of the solar convection zone where strong differential rotation is concentrated. It is within this tachocline that the strong toroidal fields to be generated are expected. If the interaction with convection keeps the magnetic field in the form of flux tube, then the toroidal field generated in the tachocline may be in the form of flux rings going around the rotation axis of the Sun (Browning, Miesch, Brun, & Toomre, 2006; Tobias, 2002; Choudhuri, 2007).

Now, it can be shown that magnetic buoyancy is particularly destabilizing in the interior of the convection zone, where convective instability and magnetic buoyancy reinforce each other. On the other hand, if a region is stable against convection, then magnetic buoyancy can be partially suppressed there (Parker, 1979). Since the toroidal flux tube is produced at the bottom of the convection zone, some parts of it is expected to come into the convection zone and become buoyant, whereas other parts may remain underneath the bottom of the convection zone and stay anchored there due to the suppression of magnetic buoyancy. A part of the flux tube coming within the convection zone is expected to rise and eventually reach the solar surface to form sunspots (Choudhuri, 2007).

Discussion of dynamo theory as to whether it is possible for motions inside the plasma to sustain a magnetic field, Equations 3.11 and 3.12 would be solved to understand how velocity and magnetic fields interact with each other. A major breakthrough occurred when Parker (1955) realized that turbulent motions inside the solar convection zone (which are by nature non-axisymmetric) may be able to sustain the magnetic field.

We have seen how a magnetic field line in the poloidal plane may be stretched by the differential rotation to produce a toroidal component. Parker (1955) pointed out that the uprising hot plasma blobs in the convection zone would rotate, as they rise, because of the Coriolis force of solar rotation (just like cyclones in the Earth's atmosphere) and such helically moving plasma blobs would twist the toroidal field to produce magnetic loops in the poloidal plane. Keeping in mind that the toroidal field has opposite directions in the two hemispheres and helical motions of convective turbulence should also have opposite helicities in the two hemispheres.

According to Choudhuri (2007) and Tobias (2002) although the magnetic Reynolds number is high situation and the magnetic field is nearly frozen in the plasma (i.e. molecular resistivity is negligible), it would be expected the turbulent mixing to give rise to an effective diffusion and the poloidal should eventually coalesce to give the large-scale poloidal field. The poloidal and toroidal components of the magnetic field feed each other through a closed loop. The poloidal component is stretched by differential rotation to produce the toroidal component. On the other hand, the helical turbulence acting on the toroidal component gives back the poloidal component. Some of the basic ideas of mean field MHD are to deal with a turbulent situation, by splitting both the velocity field and the magnetic field into average and fluctuating parts;

$$v = \bar{v} + v' \; ; B = \bar{B} + B' \tag{3.17}$$

where the overline indicates the average and the prime indicates the departure from the average. On substituting Equation 3.17 in the induction Equation (3.12) and averaging term by term, Equation 3.18 is obtained.

$$\frac{\partial \overline{B}}{\partial t} = \nabla \times (\overline{v} \times \overline{B}) + \nabla \times \varepsilon + \lambda\nabla^2 B \tag{3.18}$$

on remembering that $\mathbf{v}' = \mathbf{B}' = 0$. Here

$$\varepsilon = \overline{v' \times B'} \tag{3.19}$$

where ε is the mean e.m.f. and is the crucial term for dynamo action. This term can be perturbatively evaluated by a scheme known as the first order smoothing approximation.

If the turbulence is isotropic, then this approximation scheme leads to

$$\varepsilon = \alpha\overline{B} - \beta\nabla \times \overline{B} \tag{3.20}$$

Where

$$\alpha = -\frac{1}{3}\overline{v}.(\nabla^2 \times v') \tag{3.21}$$

and

$$\beta = \frac{1}{2}\overline{v'.v'}\,\tau \tag{3.22}$$

Where τ is the correlation time of turbulence

On substituting Equation 3.20 in Equation 3.18, Equation 3.23, obtained is referred to as the dynamo equation.

$$\frac{\partial \overline{B}}{\partial t} = \nabla \times (\overline{v} \times \overline{B}) + \nabla \times (\alpha\overline{B}) + (\lambda + \beta)\nabla^2 \overline{B} \tag{3.23}$$

where α is a measure of average helical motion in the fluid. It is this coefficient which describes the production of the poloidal component from the toroidal component by helical turbulence. This term would go to zero if turbulence has no net average helicity (which would happen in a non-rotating frame). β is of the nature of a diffusion coefficient. Since this is basically diffusion induced by turbulence, it is called turbulent diffusion.

3.6 Solar Dynamo

Variations in total solar irradiance (TSI) and solar spectral irradiance (SSI) on time scales up to the solar cycle have been found to be largely modulated by sunspots and faculae. These features are caused by the eruption of magnetic fields through the solar surface. The production of strong magnetic fields within the Sun is an area of intensive research. A full discussion of this topic is not within the scope of this thesis but can be found in Charbonneau (2010) (and references within), but a brief description is needed to understand the origin of surface features integral to solar variability.

Outside the nuclear burning core, the Sun is composed entirely of plasma and is divided into two distinct regions. The radiative zone, containing the fusion core, extends out to ~70% of the solar radius and exhibits solid body rotation. Beyond this, convection becomes the driving force for energy distribution and is present between the top of the radiative zone up to the photosphere, where small scale convection manifests as granulation. The convection zone undergoes differential rotation by both latitude and depth, rotating more slowly at the poles than at the equator (Tobias, 2002)

 Helioseismology has determined that there is a significant shear profile at the boundary layer between the convective and radiative zones, known as the tachocline (Browning et al., 2006). Here, the rapidly changing rotation rate is thought to provide a mechanism that produces a magnetic dipole. The dynamo is thought to be self-exciting, that is it replenishes itself, with a period of 22 years. This 22 year periodicity appears as two solar cycles of activity that sees two reversals in the magnetic polarity of the northern and southern hemispheres (Kundt, 1992).

It is thought that activity manifests itself at the surface due to the buildup of magnetic fields deep inside the Sun, near the tachocline. At the start of a solar cycle the magnetic field is polodial, or poleward, but convective material overshooting to the base of the tachocline is stretched by the rapidly changing rotation rate (Browning et al., 2006; Charbonneau, 2010), strengthening the polodial field into a toroidal field (along latitude lines).

Finally, these boosted magnetic fields, embedded within convection currents, become buoyant and rise, eventually reaching and breaking through the surface. The appearance of these strong magnetic fields at the surface are typified by sunspots.

3.7 The Solar Indices

Solar indices can be divided into physical and synthetic according to the way they are obtained/calculated. Physical indices quantify the directly-measurable values of a real physical observable, such as the radio flux, and thus have clear physical meaning. Physical indices quantify physical features of different aspects of solar activity and their effects. Synthetic indices (the most common being sunspot number) are calculated (or synthesized) using a special algorithm from observed (often not measurable in physical units) data or phenomena. Additionally, solar activity indices can be either direct (i.e., directly relating to the sun) or indirect (relating to indirect effects caused by solar activity) (Usoskin, 2013).

3.7.1 The International Sunspot Number

The sunspot number (also known as the International sunspot number, relative sunspot number, or Wolf number) is a quantity that measures the number of sunspots and groups of sunspots present on the surface of the Sun. The most commonly used index of solar activity is based on sunspot number. Sunspots are dark areas on the solar disc (of size up to tens of thousands of km, lifetime up to half-a-year), characterized by a strong magnetic field, which leads to a lower temperature (about 4000 K compared to 5800 K in the photosphere) and observed darkening.

Sunspot number is a synthetic, rather than a physical, index, but it has still become quite a useful parameter in quantifying the level of solar activity. This index presents the weighted number of individual sunspots and/or sunspot groups, calculated in a prescribed manner from simple visual solar observations. The use of the sunspot number makes it possible to combine together thousands and thousands of regular and fragmentary solar observations made by earlier professional and amateur astronomers. The technique initially developed by Rudolf Wolf, yielded the longest series of directly and regularly-observed scientific quantities. Therefore, it is common to quantify solar magnetic activity via sunspot numbers. The details can be found from the review on sunspot numbers and solar cycles as given by (Hathaway & Wilson, 2004; Hathaway, 2010).

The relative sunspot number R_z is defined as

$$R_z = k\,(10G + N) \tag{3.24}$$

Where G is the number of sunspot groups, N is the number of individual sunspots in all groups visible on the solar disc and k denotes the individual correction factor, which compensates for differences in observational techniques and instruments used by different observers, and is used to normalize different observations to each other (Usoskin, 2013).

The routine production of the Wolf's sunspot number (WSN) series was terminated in Zurich in 1982. Since then, the sunspot number series is routinely updated as the International sunspot number R_i, provided by the Solar Influences Data Analysis Center in Belgium (Clette, Berghmans, Vanlommel, Van der Linden & Koeckelenbergh, 2007). The international sunspot number series is computed using the same definition (Equation 3.24) as WSN but it has a significant distinction from the WSN in that it is based not on a single primary solar observation for each day but instead uses a weighted average of more than 20 approved observers.

Sunspots are characterized by a dark core (umbra) and a less dark surrounding area (penumbra). It is the existence of the penumbra which distinguishes a sunspot from a pore on the Sun's surface. Sunspots exhibit diameters from 3.5 x 10^6 to 60 x 10^6 m. Once the diameter of a growing pore exceeds the lower limits for spots, the penumbra abruptly develops sector by sector. The brightness within the umbra is significantly reduced by up to 80% and 21% respectively compared to the normal photosphere, that is, the quiet Sun. According to Planck's function, brightness is closely associated with temperature. Hence the temperature within a sunspot is considerably lower than that of a quiet Sun. The umbra is cooler by 1000 to 1900 K. The penumbra is 250 to 400 K cooler. At these temperatures, molecules may also exist and their absorption lines are found in the spectra of the spots (Solanki, 2003).

The strong magnetic field inside a sunspot inhibits convection of energy and this causes the cooling. Sunspot starts to decay as soon as they are formed, in some cases, even before they are fully formed. The lifetime of a sunspot may vary from hours to months. The larger the sunspot, the larger is the lifetime. Around minimum solar activity, there are times without a single spot on the solar disc while at periods of maximum activity several spots may be presented simultaneously. From the properties of sunspots, it can be concluded that the irradiance decreases in periods of high solar activity. However, measurements show that the opposite is true i.e. the solar irradiance is enhanced during maximum activity. This is due to the brightening effect of faculae (Kubin, 2011; Solanki, 2003).

3.7.2 Faculae

In contrast to dark spots, the bright faculae are less visible, in white light only near the limb. From this and the fact that they seem to disappear in white light near the centre of the disc, one can infer that their emissions originate in upper layers. The faculae occur in the vicinity of spots. They appear earlier and live longer than the associated spots.

Corresponding phenomenon in the chromospheres are called plages (Lean, 1997). They are detected at certain wavelengths, for example, at the calcium K Fraunhofer line

(393.4 nm) or the H_α line (656.3 nm). Inside the faculae, the temperature of the photosheric base is higher than the surrounding areas. The difference is estimated to be 100 K (Kiepenheiner, 1954). A proxy for faculae brightening is Mg II index (core to wing ratio of the doublet at 280 nm). It is used as it is closely related to faculae and chromospheric plages.

3.7.3 The Solar Radio Flux (F10.7 Index)

A 10.7 cm solar flux measurement is a determination of the strength of solar radio emission in a 100 MHz wide band centered on 2800 MHz (a wavelength of 10.7 cm) averaged over an hour (Tapping, 2013). A traditional physical index of solar activity is related to the radio flux of the sun in the wavelength range of 10.7 cm and is called the F10.7 index (Tapping & Charrois, 1994). This index represents the flux (in solar flux units, 1 sfu = 10^{-22} Wm^{-2} Hz^{-1}) of solar radio emission at a centimetric wavelength. This emission is close to the peak of solar radio emission and is produced as a result of the non radiative heating of coronal plasma over active regions.

F10.7 index is a good quantitative measure of the level of solar activity, which is not directly related to sunspots. Close correlation between the F10.7 index and sunspot number indicates that the latter is a good index of general solar activity, including coronal activity. The solar F10.7 cm record has been measured continuously since 1947. F10.7 index is a useful proxy for the combination of chromospheric, transition region, and coronal solar EUV emissions modulated by bright solar active regions whose energies at the Earth are deposited in the thermosphere. The 10.7 cm flux resembles the integrated fluxes in UV and EUV well enough to be used as their proxy (Chapman & Neupert, 1974; Donnelly, Heath, Lean & Rottman, 1983; Nicolet & Bossy, 1985; Lean, 1990).

This radio emission comes from the upper part of the chromosphere and the lower part of the corona. F10.7 radio flux has two different sources: thermal bremsstrahlung (due to electrons radiating when changing direction by being deflected by other charged participles - free-free radiation) and gyro-radiation (due to electrons radiating when

changing direction by gyrating around magnetic fields lines) (Bruevich & Yakunina, 2011).

There are two types of flux values: The observed flux values and the adjusted flux values. The observed flux are the values that would be incident on the top of the atmosphere or at ground level in the absence of that atmosphere. It is the measured value multiply by atmloss. These flux values are intended for use for terrestrial applications. The adjusted flux values are modulated by changing Earth – Sun distance. When the flux values are being used as an index of solar activity, for example, being compared with other solar activity indices such as sunspot number, then modulation is undesirable and hence can be corrected by multiplying by the Earth – Sun distance in astronomical units (AU) which then makes the flux values refer to a constant distance of AU (Tapping, 2013).

3.7.4 NOAA Mg II core to wing ratio (Mg II Index)

The space-based Mg II core-to-wing ratio as an index of solar UVI (Donnelly, White & Livingston, 1994; Viereck & Puga, 1999; Snow, Mcclintock, Woods, White, Harder & Rottman, 2005) is another direct and physical index. The Solar chromospheric activity in the ultraviolet region is of great importance to our understanding of both the physical properties of the Sun as a star, and of the solar influence on the Earth's stratospheric chemistry. In the UV region, the Mg II core-to-wing ratio introduced by Heath and Schlesinger (1986) is one of the most widely used indices of solar activity.

The 280 nm Mg II solar spectrum band contains photospheric continuum and chromospheric line emissions. The Mg II h and k lines at 279.56 and 280.27 nm, respectively, are chromospheric in origin while the weakly varying wings or nearby continuum are photospheric in origin. Instruments of the satellites observe both features. The ratio of the Mg II variable core lines to the nearly non-varying wings is calculated using Equation 3.25:

$$I = \frac{4\left[E_{279.8} + E_{280.0} + E_{280.2}\right]}{3\left[E_{276.6} + E_{276.8} + E_{283.2} + E_{283.4}\right]} \qquad (3.25)$$

Where I is the index and E is the emissions.

Mg II core-to wing ratio observations were made by NOAA series operational satellites (NOAA-16-18), which host the Solar Backscatter Ultra Violet (SBUV) spectrometer (Viereck et al., 2001). This instrument can scatter solar Middle Ultra Violet (MUV) radiation near 280 nm. The Mg II observation data were also obtained by ENVISAT instruments. NOAA started in 1978 (during the 21st, 22nd and the first part of the 23rd solar activity cycles), ENVISAT was launched in 2002 (last part of the 23rd solar activity cycle). Comparison of the NOAA and ENVISAT Mg II index observation data shows that the two Mg II indices agree to within about 0.5% (Viereck et al., 2004; Skupin, Weber, Bovensmann & Burrows, 2005). We used both the NOAA and ENVISAT observational data of the Mg II index.

The Mg II index is an especially good proxy for some Far Ultra Violet (FUV) and Extreme Ultra Violet (EUV) emissions (Skupin et al., 2005). It well represents photospheric and lower chromospheric solar FUV Schumann-Runge Continuum emission near 160 nm that maps into lower thermosphere heating due to O_2 photodissociation (Bowman, Tobiska, Marcos, Huang, Lin & Burke, 2008). Since a 160 nm solar index is not produced operationally, the Mg II index proxy is used for comparison with the other solar indices (Tobiska et al., 2008).

The solar chromospheric activity in the ultraviolet region is of great importance to our understanding of both the physical properties of the Sun as a star, and of the solar influence on the Earth's stratospheric chemistry. In the UV region, the Mg II core-to-wing ratio introduced by Heath & Schlesinger (1986), is one of the most widely used indices of solar activity.

3.8 The Heliosphere

This is the space from the Sun via the Earth to the heliopause i.e. end of the solar spectrum. Other than atmospheric and solar-terrestrial physics, heliophysical studies include studies of other planets, the outer reaches of the heliosphere and its interaction with interstellar medium (Riley & Crooker, 2004)

3.8.1 Space weather

This is the physical condition in space around the Earth that is determined ultimately by solar activity. Space weather manifests itself through various physical phenomena such as enhanced intensity of hard radiations, increased strengths of electric and magnetic fields and elevated magnitude of electric currents (Fernandez, 2006).

Going further away from the Sun's atmosphere towards the Earth, we come across the gaseous portion of the Earth referred to as the atmosphere of the Earth which is retained by the Earth's gravity. The average mass of the atmosphere is about 5,000 trillion metric tons. The National Centre for Atmospheric Research reported that the total mean mass of the atmosphere is 5.1 x 10^{18} kg with an annual range due to water vapor of 1.2 or 1.5 x 10^{15} kg depending on whether surface pressure or water vapor data are used.

3.9 The Structure of the Earth's Atmosphere

Before discussing the changes in the Earth's atmosphere induced by the 11 year solar cycle, it is necessary to recall the fundamental characteristics of the individual layers of the atmosphere and the absorption of solar irradiance.

The Earth's atmosphere ranges from the surface to about 1000 km. It is composed of 78.09% nitrogen, 20.95% oxygen, 0.93% argon and a number of trace gases, for example, carbon dioxide, methane, nitrous oxide (Brasseur & Solomon, 2006).

Table 3.2 Mean composition of the atmosphere (Brasseur & Solomon, 2006)

Compound	volume fraction		mass fraction	
Nitrogen	78.09	%	76.47	%
Oxygen	20.95	%	23.53	%
Argon	0.93	%	1.29	%
Carbon dioxide	0.038	%	0.015	%
Neon	18.180	ppmv	12.75	ppm
Helium	5.240	ppmv	0.73	ppm
Methane	1.760	ppmv	0.97	ppm
Krypton	1.140	ppmv	3.30	ppm

The layer directly above the surface is the troposphere. It starts from the surface to altitudes between 8 and 18 km being higher in the tropics and lower in the near the poles. In the troposphere, the temperature decreases with height on average with a lapse rate of 0.65 K/100 M. About 50% of the atmosphere's mass is situated below 500 hPa (~ 5 km). In the lower most 1500 m, named the planetary boundary layer, bottom friction is important. In free troposphere above, frictional processes may be neglected. The troposphere is the region where all the processes commonly referred to as 'weather' take place, in particular, processes that involve phase changes of water like cloud, rain, hail, fog etc. (Layers of the earth's atmosphere, via http://www.windows2universe.org/earth/Atmosphere/layers_activity_print.html)

At 8 to 18 km, depending on latitude, temperature reaches a minimum and starts after an isothermal region of variable height to increase with latitude above. This marks the tropopause i.e. the interface between the troposphere and the stratosphere. The reason for the temperature increase in the stratosphere is the absorption of ultraviolet (UV) solar radiation and the associated heating in the ozone layer at 25 km (~ 25 hPa). (Calisesi & Matthes, 2007)

The temperature increase with height forms an effective barrier for vertical mixing from the layer below. The temperature maximum is found at 50 km (~ 1 hPa). This forms the loop of the stratosphere and the interface to the next higher layer called the stratopause.

The mesosphere (50 – 85 km) is characterized by a decrease in temperature with height. In this regard, it resembles the troposphere but with a much lower air density. The temperature lapse rate amount to ~ 0.3 K/ 100 m. The mesopause, the upper boundary of the mesosphere, is the coldest region in the atmosphere with temperature values as low as ~ 90 ˚C. The Thermosphere is the adjacent layer above the mesopause. Between the surface and about 100 km the composition of the air is roughly constant. About the same height, diffusive processes become important leading to a segregation of air into constituents.

The exosphere above 500 km forms the transition region from the atmosphere to space where molecules and atoms can escape from the Earth's gravitational field. The temperature increases with height throughout the thermosphere and exosphere, reaching values up to 2000 ˚C (Layers of the earth's atmosphere, via http://www.windows2universe.org/earth/Atmosphere/layers_activity_print.html)

Besides the classification according to the temperature change with height, the atmosphere can be divided into neutral and ionized layers. The absorption of EUV radiation with wavelengths shorter than 100 nm leads to ionization of the absorber, producing ions and free electrons. This takes place above 70 km and forms the ionosphere. The maximum electron density is found at 250 km to 300 km.

3.10 Absorption of the Solar Radiation in the Atmosphere

It becomes clear that the structure of the Earth's atmosphere is inseparably connected with the absorption of solar radiation. The total solar irradiance TSI (1365 W/m^2) (Fröhlich & Lean, 2004) arrive at the top of the atmosphere. The Earth reflects a fraction of the solar energy back to space and absorbs the remainder at a rate of:

$$(1 - A) \text{ TSI}/4 \tag{3.26}$$

Where, A is the Earth's albedo. The division by 4 is done to account for the Earth's sphericity, that is, the Earth's intercept πR_E^2 TSI solar energy per unit time; where R_E is the mean radius of Earth but this has to be averaged on the surface area of the Earth's sphere $4 \pi R_E^2$ (Gray, Beer, Geller, Haigh, Lockwood, Matthes & Luterbacher, 2010)

The penetration depth of solar radiation depends on wavelength. The shorter the wavelength the higher in the atmosphere the radiation is absorbed. Absorption of the radiation may have several consequences. On one hand, it may be photolysed, which is, split up. An excited molecule may release its excess energy at a collision with other molecules or atoms. The photolysis products may recombine likewise releasing energy which ultimately ends up as heat. Hence the chemical (photodissociation) and thermal (heating) effect of radiation absorption are closely connected.

However, the assumption that absorbed solar energy is entirely converted into heat at the location of absorption, apply only in the lower atmosphere where collisions are frequent and recombinations fast. It is not valued at higher altitudes where recombinations may take place several thousands of kilometers away from the absorption location (Brasseur and Solomon, 2005). The two main absorbers are molecular oxygen (O_2) and especially in the stratosphere, ozone (O_3).

3.11 Ozone and Temperature Distribution in the Mid-atmosphere

Ozone absorbs ultraviolet (UV) radiation from the sun, and modulates outgoing infrared (IR) radiation from the earth. Because of its chemical and radiative properties, atmospheric ozone constitutes a key element of the earth's climate system. Absorption of sunlight by ozone in the ultraviolet wavelength range is responsible for stratospheric heating, and determines the temperature structure of the middle atmosphere (Calisesi & Matthes, 2007).

The principal absorbers in the earth's atmosphere are water vapour in the troposphere which absorbs primarily in the near-infrared region, $0.7\mu m \leq \lambda \leq 4\mu m$ and in the stratosphere; at shorter wavelengths, the main gaseous absorber is ozone which is effective in the ultraviolet ($\lambda \leq 0.35\mu m$) and in the visual ($0.5\mu m \leq \lambda \leq 0.7\mu m$). Most of

the absorption in the ultraviolet occurs at altitudes 25 – 50 km, above the region of maximum ozone concentration (Lacis & Hansen, 1974).

For meteorological purposes the heating rate is of more immediate interest than the absorbed energy. In the earth's atmosphere the heating rate is related to the absorbed energy by Equation 3.27 according to Lacis and Hansen, (1974) as;

$$\frac{\Delta T}{\Delta t} = \frac{\pi F_O \, g \, A_i}{c_p \Delta P \Delta t}$$

(3.27)

Where c_p is the specific heat at constant pressure, g the acceleration due to gravity, $\mathbf{\Delta P}$ the pressure difference between the top and bottom of the ith layer, and A_i the fraction of the total solar flux absorbed in the ith layer for ozone.

3.12 Ozone, Weather/Climate System

Variations in weather/climate conditions play an important role in determining ozone concentrations. Ozone is more readily formed on warm, sunny days when the air is stagnant. In the troposphere, the air is usually warmest near the ground. Warm air has a tendency to rise and cold air to sink, causing the air to mix, which disperses ground-level pollutants. However, if cooler air gets layered beneath warm air, no mixing occurs - the air is stable or stagnant.

Conversely, ozone production is more limited when it is cloudy, cool, rainy, or windy. The direction and strength of the wind also affect ozone concentrations (ARB, 2002; Cox & Chu, 1996). Ozone hole has large and far-reaching impacts in the weather/climate system. The hole in the earth's ozone layer over the South Pole has affected atmospheric circulation in the Southern Hemisphere all the way to the equator and this has led to increased rainfall in the subtropics (Kang, Polvani, Fyfe & Sigmond, 2011). It is not really amazing that the ozone hole, located so high up in the atmosphere over Antarctica, can have an impact up to the tropics and affects rainfall there. The process through which this was achieved is known as coupling.

When temperature of the stratosphere increases by absorbing solar radiation, there will be higher stratospheric ozone concentration. This also helps to attain low temperature in the troposphere and heavy rainfall. Consequently, when ozone is depleted, solar UV rays fall directly on troposphere. As a result, temperature of stratosphere decreases and that of troposphere increases. This helps to attain an unfavorable condition of rainfall (Midya, Saha, Panda, Kundu, Chaudhuri, & Sarkar, 2011).

3.13 Variability of Ozone in the lower stratosphere

Variability of ozone can result from a number of causes. Solar UV radiation that produces ozone is present during the day but not at night. It varies with the 27-day solar rotation cycle and with the 11-year sunspot cycle. There exists a regular variation of the total column amount of ozone with weather systems (example of short-term dynamical variations) such as pressure. For instance, Dobson (1966) observed low amounts of ozone when there was high pressure system over the south of England; and when a low pressure system moved in, he also observed that the ozone amount increased.

The concentration of ozone at a location is governed by a balance among ozone production, loss, and transport. These processes determine the amount of ozone in the stratosphere and its distribution with latitude, longitude, and altitude. They contribute to the variability of ozone observed on different time scales. The atmosphere is continuously in motion and this motion occurs over different time scales, ranging from a single day to several decades (Haynes, 2005).

This atmospheric circulation affects ozone on many time scales which include the regular seasonal variations, the 27-30-month quasi-biennial oscillation, and the less regular El Niño Southern Oscillation. Sporadic major volcanic eruptions can also cause a short-term variation of ozone. In general, the chemical effect of the long-term increase in chlorine from chlorofluorocarbons (CFCs) should lead to a long-term decrease in ozone that can be separated from the other causes of variability (Madhu & Gangadharan, 2016; Molina & Rowland, 1974).

Ozone in the lower atmosphere (the troposphere and lower stratosphere) has a long life time on the order of months to years; this is because the photochemical processes that create and destroy ozone occur very slowly in the lower atmosphere. This, in turn, is because the ultraviolet radiation that drives ozone photochemistry is mostly screened out from the lower atmosphere by the ozone higher in the atmosphere. The primary source of variability in the lower atmosphere is transport processes (Space Physics course, 2011).

3.13.1 The Quasi-Biennial zonal wind Oscillation (QBO)

The wind in the stratosphere change direction on average of every 26 months and the alternating easterly and westerly wind regimes descend with time (Reed, Campbell, Rasmussen & Rogers, 1961; Veryard & Ebdon, 1961). The Quasi-Biennial Oscillation (QBO) is a slow oscillation in strength and direction of the zonal wind in the lower and middle stratosphere over the equator of the earth's atmosphere. It has a period of approximately 2 years (hence the 'quasi-biennial' title) and has been observed for more than 50 years now in climatological records.

The QBO develops as a result of the disturbances (or waves) in the tropical troposphere (generated by convective activity and other forcing in the tropics), propagating vertically into the lower stratosphere. These disturbances interact with the average wind in such a way as to cause the average wind to regularly reverse its direction. The QBO not only changes the circulation in the tropics, but it also indirectly causes changes at middle and high latitudes. The waves that cause the reversal of the tropical winds do so by exerting a drag on the flow. Thus, momentum is exchanged between the tropics and the extra tropics. Air is also transported between the two latitude regions. These air masses have different O_3 concentrations.

3.13.2 El-Nino Southern Oscillation (ENSO)

El Nino, an abnormal warming of surface ocean waters in the eastern tropical Pacific, is one part of what is called the Southern Oscillation. ENSO is a quasi-periodic climate pattern that occurs across the tropical Pacific Ocean approximately every five years. The

Southern Oscillation is the see-saw pattern of reversing surface air pressure between the eastern and western tropical Pacific; when the surface pressure is high in the eastern tropical Pacific, it is low in the western tropical Pacific, and vice-versa. This reversal thereby causes variability in ozone, hence, low amount of ozone in the eastern tropical Pacific and high in the western tropical Pacific and vice versa (Bojkov, 1987).

ENSO mode in the total ozone variations has a zonal asymmetric pattern unlike the seasonal cycle and QBO which have strong zonal uniform phase changes. Because the ocean warming and pressure reversals are, for the most part, simultaneous, scientists call this phenomenon the El Nino/Southern Oscillation or ENSO for short. ENSO causes extreme weather (such as floods and droughts) in many regions of the world Ahn and Shin (1998). Developing countries dependent upon agriculture and fishing, particularly those bordering the Pacific Ocean, are the most affected.

Volcanoes play an interesting role in the destruction of ozone. Volcanoes release bromine and chlorine when they erupt and those chemicals could have a disastrous effect on the ozone layer in the upper atmosphere. For instance, hydrogen chloride a common volcanic gas efficiently destroys ozone. But, most volcanic hydrogen chloride is washed out by rain before it has the opportunity to reach and react with the protective stratospheric ozone layer. Significant ozone loss was observed in the stratosphere after the devastating 1991 eruption of Mt. Pinatubo, Philippines, which produced a plume that rose to 34 km well into the stratosphere (Space Physics course, 2011).

CHAPTER FOUR

RESEARCH DATA AND METHODOLOGY

4.1 Introduction

In this chapter, research study area, research methods, design and data used in this work are discussed. Section 4.1 gives a brief description of the study area, the codes used, position and elevation. Section 4.2 describes the research design adopted. The data collection method involved and the websites where the parameters datasets were obtained are provided and discussed in section 4.3. Section 4.4 introduces the analyses methods adopted in this work. Starting with the several procedures the collected data underwent before analysis (data quality control and data reduction) to the methods used for analyses: time series plots, determination of percentage variability, correlational analyses, spectral analysis and finally the two techniques used for modeling of the solar indices and stratospheric ozone.

4.2 Study Area

Kenya (Figure 4.1) is located in the Eastern part of Africa (5ºN, 4.40ºS and 33.53ºE, 41.56ºE) and has a total area of 582,646 km^2. Kenya is a country boarded by Latitude 5º S and 5º N; and Longitude 34º E and 42º E as shown in Figure 4.1. The equator passes through Kenya. Situated in the Eastern part of Africa, Kenya shares boundaries with Tanzania on the Southern side, Uganda on the West, Sudan on the North Western, Ethiopia and Somalia on the Northern and Eastern sides respectively. The country borders the Indian Ocean on the South Eastern side where the coastal city of Mombasa is located. Kenya, Uganda and Tanzania share Lake Victoria; the world's second largest fresh water lake. The city of Kisumu is on the shores of this lake while Nairobi is in the inland.

Table 4.1 shows the codes, positions and elevations of the three cities. TCO trends and variability have not been carried out in major towns and cities.

Table 4.1 Names, codes, position and elevation of the three Kenyan cities

Station	Code	Latitude (ºS)	Longitude (ºE)	Altitude (m, asl)
Nairobi	nrb	1.17	36.46	1661
Kisumu	ksm	0.03	34.45	1131
Mombasa	msa	4.02	39.43	17

asl = above sea level.
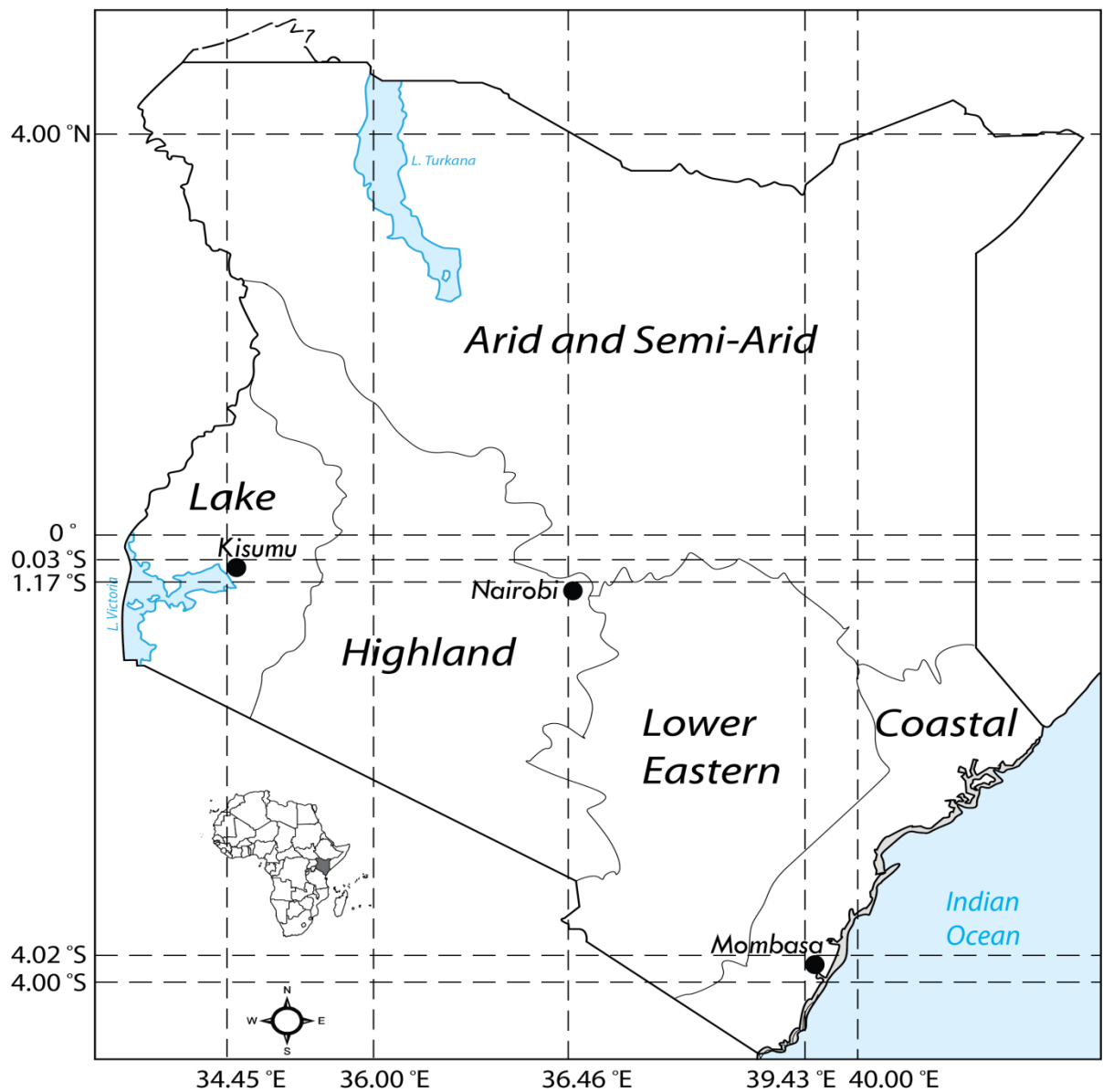
Figure 4.1 Map of Kenya indicating chosen cities and their geographical locations

Nairobi is centrally located in the country and covers an area of 684 km^2. It is the country's capital and largest city and holds a population of 4.1 million people (Kenya National Bureau of Statistics [KNBS], 2010). Mombasa is Kenya's second largest city, located on the South Eastern coast of the country, along the Indian Ocean. The city has an area of 295 km^2 and a population of 939 370 people (KNBS, 2010). Kisumu is the

third largest city in Kenya. It is located in Western Kenya and covers an area of approximately 417 km², with a population of 968 909 people (KNBS, 2010).

4.3 Research Method and Design

The research design, a quantitative non-experimental correlational study, investigated the relationship between the independent variables consisting of the three solar activity indices: photospheric index, chromospheric index, and coronal index to the dependent variable of ozone concentration for Kenyan cities namely Nairobi, Kisumu and Mombasa. A quantitative non-experimental approach was appropriate for this study rather than a qualitative one since the objectives of this study are quantitative in nature using data collected from existing and available databases.

In addition, a quantitative research approach rather than a qualitative design was more appropriate because a qualitative design would not allow the researcher to statistically compare data; the data in which qualitative studies is based on open-ended questions (Creswell, 2009), whereas the data that were collected for this study were numerical, and as such, quantitative in nature. Also, a non-experimental correlation design was consistent with the purpose of this study, which was to determine whether there exists a significant relationship between the ozone concentration and the solar indices. Conclusions derived from a study using a quantitative approach should provide a much higher degree of specificity than findings from a qualitative study (Anderson, Sweeney & Williams, 2006).

Correlational research seeks out associations between variables and investigates the extent to which the variables are related. It is important to note that while a correlation may be delineated through the proposed research, causality cannot be inferred. A non-experimental research involves variables that are studied as they exist which are not manipulated by the researcher (Belli, 2009). This was appropriate since it would be impossible to control for the different independent variables, rather, existing data were collected through publicly open databases. The specific objectives were addressed through the data analysis procedures outlined in the later section.

In correlational research, data can be collected from existing databases. Data collection for the dependent and independent variables were collected from two databases that are discussed in the data collection section of this chapter. The research project did not utilize any participants, and thus, there were no identities to keep confidential. Data in this study are publicly available, and as such, confidentiality is not be of concern.

4.4 Data Collection

Data collection involved the utilization of secondary source of daily values of merged total column ozone (TCO) data over Kenyan cities namely; Nairobi, Kisumu and Mombasa and three solar activity indices (SAI) taken over the years of 1985 to 2011. These datasets are selected for these period from two different existing data sources; The independent variable of solar activity indices were collected from the National Geophysical Data Centre (NGDC) through their website, while data for the dependent variable of TCO were collected from the merged satellite dataset prepared by Bodeker Scientific from their website, both of which are publicly accessible.

4.4.1 Solar Activity Indices Data

In this study, the daily values of three SAI representing the indices from the three spheres of the Sun were used. They are often used as a proxy for the Sun's influence on parameter measured on the Earth. These include the sunspot number, which is the photospheric index, Mg II core-to-wing ratio, which is the chromospheric index and the F10.7 cm solar radio flux which is the coronal index. These SAI are the independent variables for this study.

SAI were collected from the National Geophysical Data Centre (NGDC), Boulder, Colorado, USA through their website.

4.4.2 The Merged Total Column Ozone Data

Data from a series of instruments have been used to construct the Merged Ozone Data (MOD). The oldest data are from the Backscatter Ultraviolet (BUV) instrument which flew on NASA's Nimbus 4 mission. Data are available from 1970 through 1972, though

with reduced coverage in 1972 because of reduced spacecraft power. Data from the Total Ozone Mapping Spectrometer (TOMS) and Solar Backscatter Ultraviolet (SBUV) instruments on Nimbus 7 provide global mapping of ozone from 1979 to 1993. Ozone mappers were subsequently launched on Earth Probe (TOMS) and on Aura (OMI). Meanwhile NOAA launched a series of SBUV/2 ozone profiling instruments on satellites beginning in 1984 and continuing to the present. The coverage periods of ozone instruments used to create the merged ozone data set are shown in Table 4.2 for ozone profilers and Table 4.3 for ozone mappers.

While both the ozone mapping instruments and the ozone profiling instruments can derive total column ozone, only the SBUV and SBUV/2 instruments can derive the ozone vertical distribution. The instruments and ozone retrieval algorithms for TOMS are described by McPeters et al., (1993) while the SBUV retrieval algorithm is described by Bhartia *et al*. (1996). In order to create the merged ozone data, each time series was first averaged into a monthly average zonal mean.

Table 4.2 Ozone coverage by instrument (ozone profilers)

Ozone Profilers	Coverage
Nimbus 4 BUV	April 1970 – Nov 1972
Nimbus 7 SBUV	Nov. 1978 - June 1990
NOAA 9 SBUV/2	Feb. 1985 - Feb. 98
NOAA 11 SBUV/2	Dec. 1988 - March 2001
NOAA 16 SBUV/2	Oct. 2000 - June 2010
NOAA 17 SBUV/2	July 2002 – June 2010

Table 4.3 Ozone coverage by instrument (ozone mappers)

Ozone Mappers	Coverage
Nimbus 7 TOMS	Nov. 1978 – April 1993
Meteor 3 TOMS	Sept. 1991 – Dec. 1994
Earth Probe TOMS	Aug. 1996 – Dec. 2005
Aura OMI	Oct. 2004 – Dec. 2010

In order for a zonal mean to be considered valid it must be fully sampled, that is, most of the measurements for the zone cannot be near the zone boundary. It is also required that data from at least two thirds of possible days are required for a valid monthly average. Each individual instrument was calibrated as well as possible by the original instrument

team, but comparisons with the ground-based network (Miller et al., 1996) show that there remain distinct instrument-to-instrument differences in the retrieved ozone.

The philosophy for producing the merged data set is to take the individual data sets and combine them by making simple offsets in ozone based on overlap periods or comparison with other data sets (bootstrapping). The correction offset is determined as the average difference in the 50°S to 50°N zone. No time dependence is applied to an individual data set (the only exception is the instrument on NOAA-9, which had a distinct shift in calibration after orbit precession through the terminator and is treated as though it were two distinct instruments). All the monthly zonal means for an instrument are adjusted by that fixed offset. There is no latitude dependence applied. All the data sets available for each month are then averaged together to produce the final merged ozone time series.

A near-global TCO database at 1.25° longitude by 1° latitude, combining measurements from multiple satellite- based instruments (Bodeker, Hassler, Young & Portmann, 2013) has been used to interpolate data to the three locations of interest in Kenya. The Bodeker scientific database extends from 1st November 1978 to 2013 and can be obtained from data site: http://www.bodekerscientific.com/data/total-column-ozone. Comparisons against TCO measurements from the ground-based Dobson and Brewer spectrophotometer network are used to remove offsets and drifts between a subset of the satellite-based instruments. The corrected subset is then used as a basis for homogenizing the remaining data sets.

The construction of this database improves on earlier versions of the database by including a wider range of satellite-based instruments, using updated versions of the source satellite data, extending the period covered, using improved statistical methods to model the different fields when homogenizing the data sets, and, perhaps most importantly, robustly tracking uncertainties from the source data sets through to the final climate data record which therefore now comes with associated uncertainty fields (Bodeker, Nitzbon & Tradowsky, 2014). The combined TCO database is validated against other global TCO datasets as detailed in Bodeker *et al.,* (2014).

Hence measurements from satellite instruments provide global coverage and are supplementary to selective ground-based observations. The combination of data derived from different space-borne instruments is needed to produce homogeneous and consistent long-term data records. Important factors such as spatial coverage, instrument drifts, record continuity, and long-term calibration stability are constricted when satellite data are considered (Loyola et al., 2009)

4.5 Data Quality Control

Before analysis, the data collected underwent several procedures, namely: data quality control and data reduction. Through data quality control, missing data were filled up. After the missing data were taken care of, the data on hand were reduced to obtain a smaller dataset that produced the same analytical results through the monthly means of SAI and TCO. With large amounts of data, short term fluctuations, which are neither systematic nor predictable, may be observed. These may mask the trend and seasonality, hence the trend analysis would greatly benefit from a dataset that is reduced from the original dataset.

4.5.1 Missing Data

The TCO dataset was continuous without gaps since effects of instrument change had been minimized by adjusting data for different instruments using the instruments overlap periods when the data from two or more instruments were available. For the SAI data set, for missing data due to information not collected, linear interpolation (Equation 4.1) was used to reconcile the data set. Although biases may be present, interpolation would be the better option than the removal of entries.

$$y = y_1 + \frac{(x - x_2)(y_2 - y_1)}{x_2 - x_1}$$

(4.1)

Where y is the missing value, (x_1, y_1) and (x_2, y_2) are the adjacent coordinates to (x, y).

4.5.2 Data Reduction

Data reduction was done to obtain a reduced representation of the data set that is much smaller in volume but which produced the same analytical results. In this work, data reduction was done to get the monthly, yearly and seasonal scales. Through this method, the means represented the dataset for the time period, while the ranges of data fluctuations for the same time period were reported by the standard deviations.

4.5.2.1 TCO Monthly Means

The monthly means of the daily values of TCO were calculated by taking the monthly averages for TCO. The sum of ozone values observed for the month was divided by the total number of days in the month as shown in Equation 4.2:

$$O_{mi} = \sum_{i=1}^{n} \frac{O_i + O_{i+1} + \cdots + O_n}{n}$$

(4.2)

where O_{mi} is the monthly average TCO, O_i is the value of TCO on the ith day of the month and n is the number of days in the month.

4.5.2.2 Annual Means of TCO

Annual averages for TCO (equation 4.3), were calculated as the sum of the monthly values (O_{mi}) divided by the twelve months in a year, that is,

$$O_{ai} = \sum_{i=1}^{12} \frac{O_{mi} + O_{mi+1} + \cdots O_{m12}}{12}$$

(4.3)

where O_{ai} is the annual averages for total column ozone.

4.5.2.3 SAI Monthly Means

Monthly means of Solar Activity Indices were calculated based on the daily sunspot values, daily F10.7 cm solar radio flux values and daily Mg II core to wing ratio values assuming that they are representatives of daily means. To calculate the monthly averages for SAI variable, the sum of variable values observed for the month were divided by the total number of days in the month as shown in Equation 4.4:

$$SAI_{mi} = \sum_{i=1}^{n} \frac{SAI_i + SAI_{i+2} + \cdots + SAI_n}{n}$$

(4.4)

where, SAI_{mi} is the monthly average SAI variable, SAI_i is the value of SAI on the ith day of the month and n is the number of days in the month.

Through this, not only were the means represented the data set for the length of time concerned, but also the range at which data fluctuates for that time period represented by the standard deviation.

4.6 Trends and Variability

The analysis of trend were done for the variables for each city by making time series plots of TCO and SAI to observe whether they are increasing or decreasing, or remain the same or display seasonal variations.

 The monthly averages were used to determine the monthly variability. A visual depiction of the trends and variability in TCO is provided by means of the time series at the three cities (Figure 5.1) and Figure 5.15 for SAI. To illustrate larger timescale trends, the seasonal variations were minimized by smoothing the time series with 13 month running mean.

Seasonal variability in TCO is calculated by using the monthly average for months of December, January and February (DJF) - a hot dry season; March, April and May

(MAM) – long rain season; June, July and August (JJA) – dry cold season and September, October and November (SON) – short rain season.

Annual, monthly and seasonal trends in TCO at the three Kenyan cities were calculated from straight line fits. Net ozone changes over the 27 year analysis period are determined by multiplying the slope in (DU/year) by 27 (Zahid & Rasul, 2010; Bhattacharya, Bhoumick & Bhattacharya, 2012).

4.6.1 Percentage variability in TCO

Percentage variability in TCO was calculated using equation 4.5:

$$A(i) = \frac{R(i)}{Q(i)} \times 100$$

(4.5)

where, i = Months of the year (1, 2 … 12), $A(i)$ = Percent Variability of total column ozone for the ith month, $R(i)$ = Range of TCO for month (i) in the twenty seven years studied, $Q(t)$ = Average TCO.

4.7 Correlation Analysis

This was also done to analyze the relationship between the time series data for any two parameters for all the cities. Analysis is carried out in four aspects namely; Pearson correlation analysis, cross correlation analysis, linear and multiple regression analyses. This analysis was performed to address the first three hypotheses, and in turn, answer the first research question. All statistical analyses are based on 95% confidence level where p value or significant value is less than 0.05 for the result to be significant.

4.7.1 Pearson Correlation Analysis

Pearson correlation analysis was conducted to examine the relationship between monthly mean SAI variables ssn, sf and mg and mean monthly TCO at each city over

the study period using Equation 4.6. Correlations among SAI variables and among TCO are also performed.

$$r = \frac{n\,(\Sigma xy) - (\Sigma x)(\Sigma y)}{\{[n\Sigma x^2 - (\Sigma x)^2][n\Sigma y^2 - (\Sigma y)^2]\}^{1/2}}$$

(4.6)

where r = Pearson correlation coefficient, x = values in the first set of data, y = values in the second dataset and n = total number of values.

4.7.2 Cross correlation analysis

Cross-correlation, also known as explanative analysis, is a type of time series analysis that calculates and plots the cross-correlation function of two or more series for positive, negative, and zero lags. Cross-correlation uses one or more variable time series, a mechanism that results in a dependent time series can be estimated. Through cross-correlation, the relationship between two or more time series data sets can be determined.

Hence to calculate the correlation coefficients between the ozone concentration and solar indices at each station, the correlation method was applied for each city. The cross – correlation Equation 4.7 employed by Kilcik (2005) was used.

For any two series x_i and y_i where i = 0, 1, 2, 3…..N-1

$$r = \frac{\Sigma[(x_i - \bar{x})(y_i - \bar{y})]}{[(\Sigma_i(x_i - \bar{x})^2)(\Sigma_i(y_i - \bar{y})^2)]^{1/2}}$$

(4.7)

In the equation, r is the cross-correlation between x and y, x (bar) and y (bar) are the means of the corresponding series.

The cross correlation function between the time series of both mean monthly TCO at each city and SAI variables was analyzed to determine the time lag(s) of SAI preceding TCO at which the series showed strongest correlations.

4.7.3 Linear regression analysis

The time lags with maximum correlation coefficient values are used in the linear regression of SAI and TCO to obtain the relationship between them. The linear dependence significance is justified by the t – test and further confirmed by the analysis of variance (ANOVA) results. The dependent variable was ozone concentration. The independent variables are the sunspot number, the F10.7 cm solar radio flux, and the Mg II core to wing ratio.

With a linear regression model, it is determined whether the independent variables are significant predictors of the TCO. The sign of the regression coefficient would determine the degree of the relationship between the two variables. A positive regression coefficient indicates that an increase in the concerned independent variable results in a positive change to the dependent variable equal to the magnitude of the regression coefficient.

A negative regression coefficient indicates that an increase in the concerned independent variable results in a decrease in a dependent variable equal to the regression coefficient. The significance of the coefficient would be based on a 0.05 level of significance. The independent two-tailed t-test was used to test the statistical significance of the parameter estimates of the independent variables. For this study, this implies that the parameter estimates of the independent variables are statistically significant.

4.7.4 Solar forcing effect

SAI variables are employed to model TCO at Nairobi, Kisumu and Mombasa by using a linear multivariate model and applying the least square fittings. The models presented were then be evaluated to indicate direct or inverse forcing of the TCO.

4.8 Spectral Analysis

In order to characterize the frequency dependence of yearly variation, a spectral analysis, also known as frequency domain analysis, of yearly TCO time series was

performed and frequency dependent variance of TCO computed. The goal of spectral estimation was to describe the distribution over frequency of the power contained in a signal, based on a finite set of data. The spectral analysis was carried out to describe how variation in a time series may be accounted for by cyclic components. With this, an estimate of the spectrum over a range of frequencies obtained and periodic components in a noisy environment ignored.

Spectral analysis is often used for periodic and cyclical observations, where a specialized technique is the Fast Fourier Transform (FFT). Spectral analyses "smoothens" the time series data and apply these methods to the smoothed series (Gottman, 1981). When analyzed, the smoothed series will not tend to show the random spikes in the periodogram. The frequencies with greatest "spectral densities," which are the frequency regions with many adjacent frequencies that account for most of the overall periodic behavior in the series were identified.

4.9 Modeling the Solar Indices and Stratospheric Ozone

In this study, two models are to be fitted to predict the mean monthly TCO. A linear model using the multiple linear regression technique and a nonlinear regression model using the artificial neural network technique are to be developed. For both models, the independent and dependent variables are given in Table 4.4.

Table 4.4 Dependent and independent Variables to Predict TCO

Variable	Measure of	Notation
(a) Dependent Variable		
Total column ozone	the vertically integrated ozone concentration in the atmosphere's column above a specific location	TCO
(b) Independent Variable		
i. Sunspot Numbers	the activity of the sun in the photosphere	ssn
ii. F10.7 cm solar radio flux	the activity of the sun in the corona	sf
iii. Mg II core to wing ratio	the activity of the sun in the chromosphere	mg

4.9.1 Data Partitioning

All the datasets had to be partitioned into training, testing and validation before they are used in the models. The number of data points (324) for the period 1985 – 2011 related to both dependent and independent variables are used for modeling. By using a random process, the data points are divided into two distinct sets; a training set consisting of 75% of the data points or 243 cases used for training the models. The training process of the models is performed using the package neuralnet R version 3.2.3 software.

The remaining 25% of the data points or 81cases is excluded from the training set. It is used to track errors, that is, to test the models performance once the models are developed during training in order to prevent over training. Data for the period January 2012 – August 2013 (20 data points) referred to hold out sample are used to assess the final models. The error for the hold out sample gives an honest estimate of the predictive ability because the hold out cases is not used to build the model

4.9.2 Multiple Linear Regression (MLR) Predictive Model Fitting

The independent and dependent variables were then subjected to multiple linear regression (MLR) analysis to determine if the solar indices are indeed significant predictors of ozone concentration. The MLR analysis is performed to address the fourth hypothesis, and in turn, answer the second research question. Furthermore, the validity

of the model was also evaluated using the statistical indicators that results from the multiple linear regression analysis as well.

A MLR framework can be used to describe the relationship, to predict future scores on the dependent variable, or to test specific hypotheses based on scientific theory or prior research (Cohen, Cohen, West & Aiken, 2003). MLR assumes a linear relationship between the independent and dependent variables, and is used to examine the relationships between the two variables.

Multiple regression begins by writing an equation in which the dependent variable is a weighted linear combination of the independent variables. In general, the regression equation may be written as Equation 4.8 (Cohen *et al*., 2003)

$$Y = b_0 + b_1X_1 + b_2X_2 + \cdots + bpXp + e \qquad (4.8)$$

Y is the dependent variable, each of the Xs is an independent variable, each of the bs is the corresponding regression coefficient (weight), and e is the error in prediction (residual) for each case. The linear combination excluding the residual, $b_0 + b_1X_1 + b_2X_2 + \cdots + bpXp$, is also known as the predicted value or Y (hat), the score expected on the dependent variable based on the scores on the set of independent variables.

The independent two-tailed t-test was used to test the statistical significance of the parameter estimates of the independent variables. For this test, the assumption of normality with equal variances should hold in the samples. Checking whether or not the samples are normally distributed can be accomplished by simply constructing a probability histogram and check visually if the histogram plot fits the normality curve.

As a standard, the level of significance is set at 5%. The predictor variable is considered a significant factor to the dependent variable if the p value is below 5%. For this study, this would imply that the parameter estimates of the independent variables are statistically significant. In addition to simply determining whether each of the solar indices are significantly correlated to ozone concentration at each station, how these solar indices significantly predict the ozone concentration was also explored.

Hence to quantify the relationship between the TCO at the three cities and the SAI variables, predict the direction of the effect and to understand the parameter with the greatest effect, an MLR model in the form of Equation 4.9 was employed

$$y = b_0 + b_1 x_1 + b_2 x_2 + b_3 x_3 + e$$

(4.9)

where y is the TCO and x_1, x_2 and x_3 are the ssn, sf and mg respectively and e is random error. b_0, b_1, band b_3 are the regression coefficients to be estimated from the training set data. The results obtained for the three cities under study are shown in Table 5.14, 5.15 and 5.16.

4.9.3 Multi-layer Feed Forward Neural Network (MLFNN) Predictive Model Fitting

For the fitting of the ANN architecture of the multi-layer feed forward neural network (MLFNN) model (Figure 4.2), 3 neurons (ssn, sf and mg) were used for input and one neuron for the output (TCO).
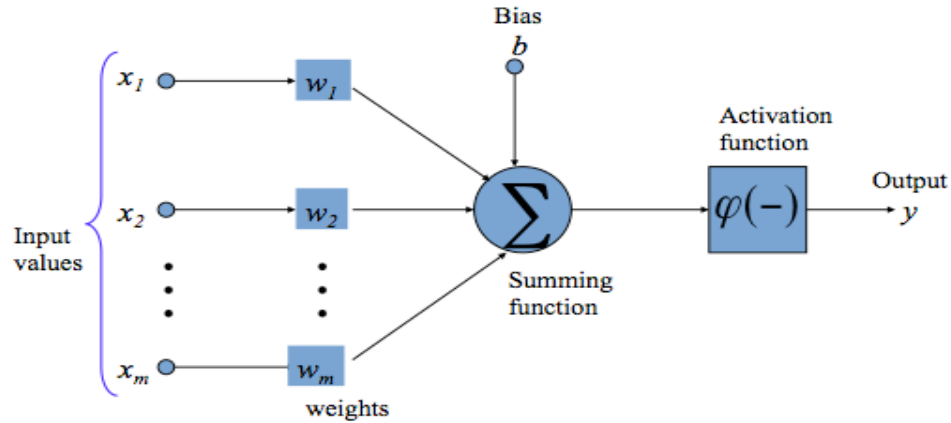
Figure 4.2 Schematic structure of artificial neural network

4.9.3.1 Data Transformation

Before training the MLFNN, all the data points are first transformed, using Equation 4.10, scaling the data to [0, 1] range.

$$t_n = \frac{(t_0 - t_{min})}{(t_{max} - t_{min})}$$

(4.10)

where t_n is the scaled value, t_0 is data value to be scaled, t_{min} and t_{max} are the minimum and maximum values of the data.

4.9.3.2 MLFNN Model Training

In training the MLFNN, incoming signals (data) are summed using Equation 4.11:

$$y(x) = \varphi \left(w_0 + \sum_{i=1}^{n} w_i x_i \right)$$

(4.11)

where w_0 denotes the intercepts, $w_i = (w_1,\ldots, w_n)$ the vector consisting of all synaptic weights without the intercept and $x_i = (x_1,\ldots,x_n)$ the vector of all inputs and φ is the "activation function" – the logistic sigmoid function (Equation 4.12) responsible for introducing non linearity in the model.

$$\varphi(x) = \frac{1}{1 + e^{-x}}$$

(4.12)

The simulator iteratively adjusts the weights until the error between the output data and the actual (observed) data are minimized. In an error back propagation (BP) with momentum learning (an adaptation of the steepest descent method) in a network with n different weights w_i, $w_2\ldots w_n$, the ith correction for weight w_k is given by Equation 4.13:

$$\Delta w = m_c . \Delta w_{prev} + (1 - m_c) . l_r . dw$$

(4.13)

where Δw_{prev} is the previous weight change, dw is the weight gradient with respect to the performance, l_r is the learning rate, and m_c is the momentum with values between 0 and 1 to be chosen.

Training is stopped when the performance gradient falls below a minimum gradient where the error function in the BP training, is the mean squared error (MSE) given in Equation 4.14:

$$MSE = \frac{1}{n} \sum_{i=1}^{n} (O_i - P_i)^2$$

(4.14)

where P_i is predicted value, O_i is the actual value and n is the number of error terms.

Several network factors such as momentum, learning rate, number of hidden nodes and threshold are tried during the training process to improve network generalization and accuracy of prediction. The best results obtained are presented in Table 5.18 for the three cities and the schematic representation of the MLFNN models for the cities are shown in Figure 5.38 (nrb), Figure 5.39 (ksm) and Figure 5.40 (msa)

4.9.4 Performance of MLR and MLFNN Models with the Test Cases

Having trained the models, testing of the models was done to judge their performance and to determine how well the predicted results agreed with the observed results by plotting line diagrams and scatter plots for visual.

The test data are used to test the respective fitted models. The results obtained by using test data are then compared with the actual results and are shown as line graphs in Figure 5.21 (nrb), Figure 5.23 (ksm) and Figure5.25 (msa) for MLR model and Figure 5.41 (nrb), Figure 5.43(ksm) and Figure 5.45 (msa) for the MLFNN model for the three cities. Scatter plots of the predicted and actual values for the models in the three cities are also displayed in Figure 5.22 (nrb), Figure 5.24 (ksm) and Figure 5.26 (msa) for MLR model and Figure 5.42 (nrb), Figure 5.44 (ksm) and Figure 5.46 (msa) for the MLFNN model for the three cities.

Quality of the fitted models and also their ability to predict were examined and verified using several statistical indicators as has been used in similar studies such as (Comrie, 1997; Chaloulakou, Grivas & Spyrellis, 2003; Jolliffe & Stephenson, 2003; Wilks,

2011; Perez et al., 2000; Willmott, 1982) These are Root mean square error (RMSE) which is a measure of the total deviation of predicted values from observed values; Correlation coefficient, R which reflects the extent of a linear relationship between the observed and the predicted values; The mean absolute error (MAE) is a quantity used to measure how close forecasts or predictions are to the actual outcome. Willmott's index of agreement (WI) which indicates the degree to which the the predictors of a model are error free. The formulae used to calculate the mentioned indices are presented in Equations 4.15 – 4.19.

$$\text{RMSE} = \left[\frac{1}{n}\sum_{i=1}^{n}(O_i - P_i)^2\right]^{1/2} \tag{4.15}$$

$$R = \frac{[n\sum_{i=1}^{n}O_iP_i - \sum_{i=1}^{n}O_i\sum_{i=1}^{n}P_i]}{\{[n\sum_{i=1}^{n}O_i^2 - (O_i)^2].[n\sum_{i=1}^{n}P_i^2 - (P_i)^2]\}} \tag{4.16}$$

$$MAE = \frac{1}{n}\sum_{i=1}^{n}|P_i - O_i| \tag{4.17}$$

$$PE = \frac{\langle(P_i - O_i)\rangle}{\langle O_i\rangle} \times 100 \tag{4.18}$$

$$WI = 1 - \frac{\sum_{i=1}^{n}(O_i - P_i)^2}{\sum_{i=1}^{n}(|P_i - \bar{O}| + |O_i - \bar{O}|)^2} \tag{4.19}$$

where P_i is predicted value, O_i is the actual value and n is the number of error terms.

The values of the statistical parameters obtained by the models are recorded in Table 5.17 (MLR model) and 5.19 (MLFNN model) for (a) Nairobi, (b) Kisumu and (c) Mombasa.

4.9.5 MLFNN and MLR Model Prediction

The models are used to predict 20 data points hold out sample which is not used to build the models. The predictive ability of the models is assessed using RMSE (Equation 4.15)

and R Equation 4.16. The predicted and observed results are presented using line diagrams and scatter plots.

4.10 Comparing Performance of MLR and MLFNN Models

Modeling of TCO has been done using traditional statistical models. Modern techniques have been proposed as efficient modeling and forecasting tools. Hence there is always a need to investigate which technique is the most efficient for a particular application. It is necessary to compare the performance of various approximation techniques. This is motivated by the fact that merits are given to various methods as a result, it is difficult to tell which method will be more suitable for a particular application (Msiza, Nelwamondo, & Marwala, 2008).

This study incorporated regression techniques and artificial neural network (ANN) models to predict TCO and hence analyze and compare the performances of the artificial neural network models with multiple linear regression (MLR) models in predicting TCO in three Kenyan cities.

The developed models results are thus compared in Table 5.20 and Table 5.21.The RMSE value of the mean for the two models in the respective cities is also compared and as a bar graph in Figure 5.58.

CHAPTER FIVE

RESULTS AND DISCUSSIONS

5.1 Introduction

This chapter presents the results and discussions on the relationship between total column ozone (TCO) and solar activity indices (SAI). The effects of TCO are also discussed. TCO variability and trends over Kenya using combined multiple satellite based instruments were examined. Monthly, annual (yearly) and seasonal trends over Nairobi, Kisumu and Mombasa are presented and discussed. Statistical study of solar forcing of total column ozone variation over three cities in Kenya in terms of correlation analysis, linear regression and solar forcing are presented and discussed. Finally, modeling and predicting of TCO using SAI as predictors are presented. Model development using, both linear and nonlinear techniques, are provided. A comparison of the models is done by calculating statistical parameters and visually using both line diagrams and scatter plots.

5.2 Trends in TCO

The trends derived from linear fits to the monthly mean TCO time series from 1985 – 2011 are shown in Figures 5.1 (a) – (c). One gross feature is the apparent decrease in TCO with time. The linear fits show that the trend in TCO is not identical at all the locations. The linear trends shown in Figures 5.1(a) – (c) suggest decreases of 2.158 DU at Nairobi, 1.759 DU at Kisumu and 2.164 DU at Mombasa over the 27 year period of analysis.

These trends are consistent with trends expected in the equatorial region where trends are expected to be zero or a minimum compared with TCO trends in the middle and higher latitudes (Holton et al., 1995). Hence, there is a decreasing trend of TCO and this loss in TCO gives a clue that, during the study period, ozone layer thickness is reducing.

The negative trend could be attributed to atmospheric dynamics specifically the meridional circulation, referred to as the Brewer-Dobson circulation, which is the main

85

source of transport at latitudes near the equator. This meridional circulations generally is driven by breaking and dissipating Rossby waves and gravity waves which dissipate their momentum in the extra tropics creating a "suction pump" which causes large scale upward transfer of air masses from the tropics into the mid and higher latitude regions (Holton et al., 1995).
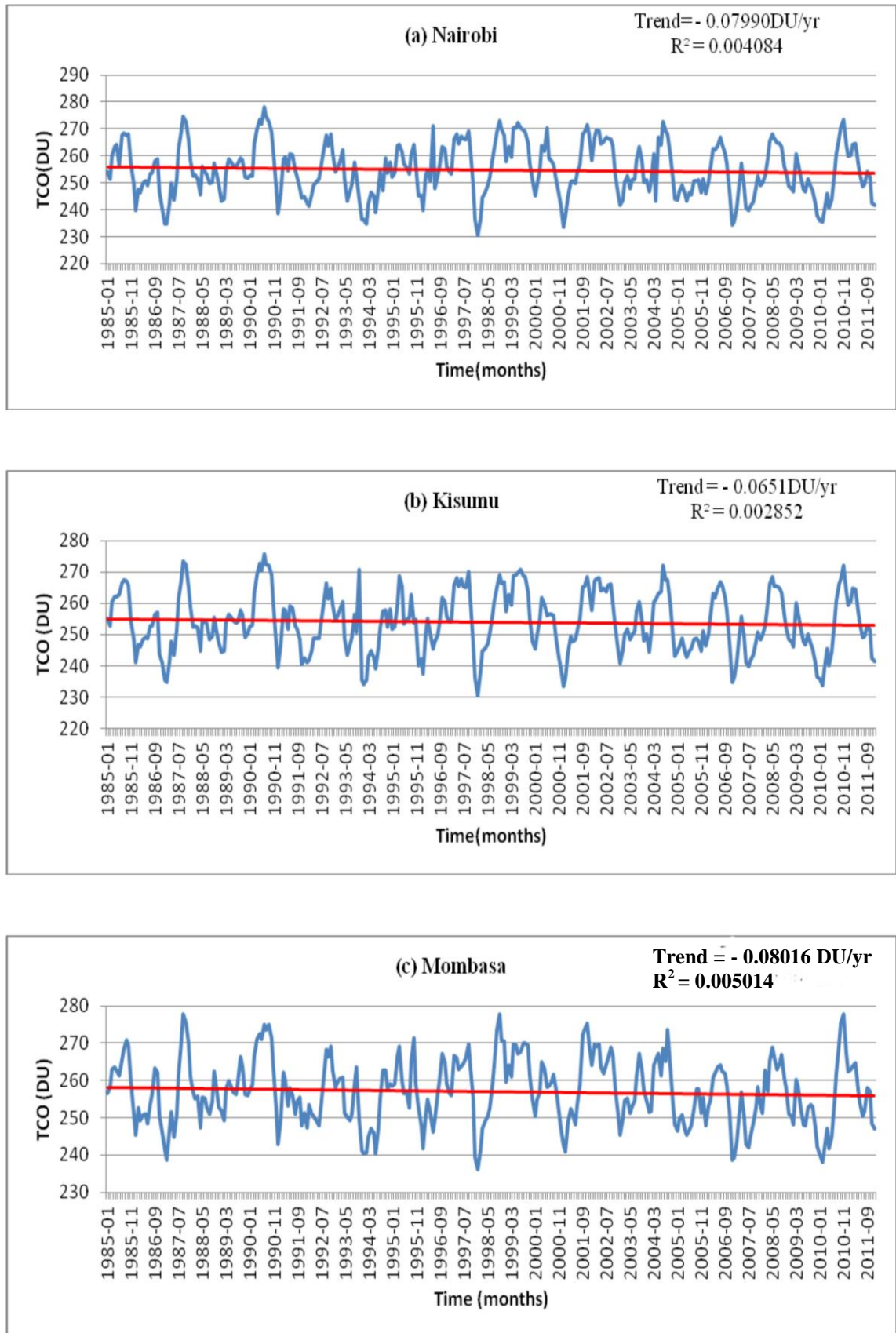
Figure 5.1 Monthly mean TCO time series from 1985 – 2011 together with their linear fits for (a) Nairobi, (b) Kisumu and (c) Mombasa

Table 5.1 Descriptive statistics of TCO for Kenyan cities during the study period from 1985 – 2011

	TCO (DU)		
	Nairobi	Kisumu	Mombasa
Mean	254.75	253.92	257.07
SD	9.76	9.54	8.84
Median	253.72	253.2	256.95
CV	3.83%	3.76%	3.44%
Max	277.93	275.85	277.86
Min	230.55	230.47	236.09
Range	47.39	45.38	41.77
Skewness	0.019	0.023	0.063
Kurtosis	-0.711	-0.738	-0.592

SD=Standard Deviation CV=Coefficient of Variation.

Table 5.1 shows the various statistical attributes of TCO at Nairobi, Kisumu and Mombasa during the study period. Mombasa registered a maximum monthly average TCO of 277.86 DU in October 1998 while Nairobi achieved a maximum of 277.93 DU in July 1990 and Kisumu a maximum of 275.85 DU in July 1990. Monthly mean minima of 230.55 DU at Nairobi, 230.47 DU at Kisumu and 236.09 DU at Mombasa were all observed in January 1988.

The temporal distribution of TCO in the three cities is approximately symmetrical (skewness ≈ 0 and hence mean ≈ median) and a value less than the kurtosis threshold (< 3) is observed. Among the locations, Mombasa had the lowest coefficient of variation of 3% compared to Nairobi and Kisumu, both had 4%.

Another persistent feature, as observed in Figure 5.1, is the presence of strong seasonal cycles, that is, high frequency variations from the data and also reduction of seasonal amplitude with time. The strong seasonal cycles resulted in low coefficient of

determination, (r^2), that is, 0.0041 at Nairobi, 0.0029 at Kisumu and 0.0050 at Mombasa. A low value of r^2 indicates that the regression line can account for only a small percentage of the variations in total column ozone.

Figure 5.2 shows line plots of the monthly mean TCO for the three cities for the same time period but the seasonal variation (high frequency variations) has been reduced using the 13 months running mean. Using the linear fit, the same decreasing trend (dashed lines) observed in Figure 5.1 is observed. A polynomial fit is also included which indicates that most of the decrease in TCO that is evident in Figure 5.1 took place between 1999 and 2010. The year 1999 and 2010 are periods of rising solar activities for solar cycles 23 and 24 respectively (Van den Berghe, 2012).
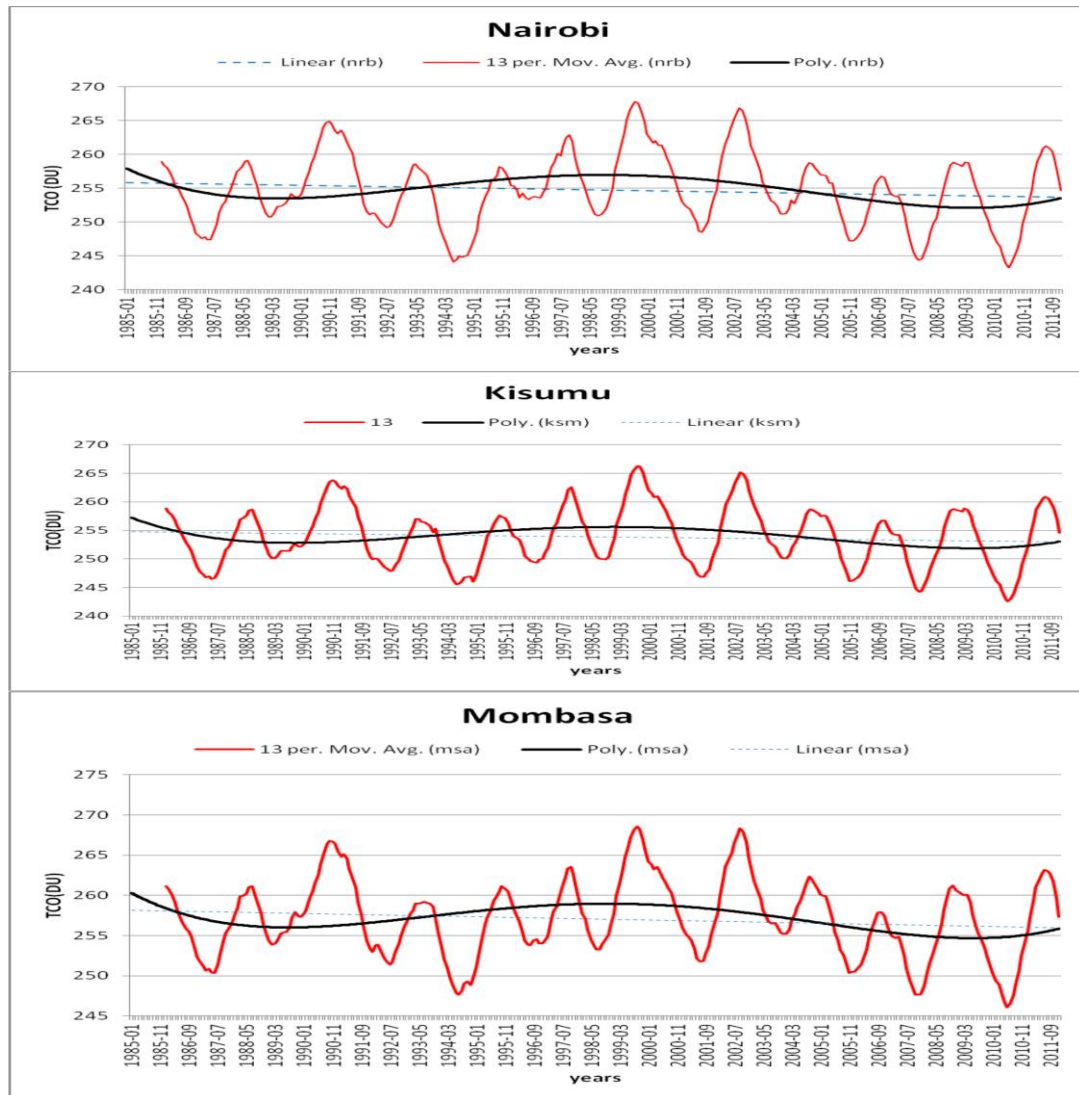
Figure 5.2 Line plots of TCO at Nairobi, Kisumu and Mombasa for the 1985 – 2011 period showing the thirteen running mean (red) and linear fit (dashed line) and polynomial fit (black)

5.2.1 Annual Trends

The annual analysis of TCO data has been done by generating time series plots for the period 1985 – 2011. The line plots in Figure 5.3 shows considerable variation in TCO amounts over the years. Some years are low, some high and many in between the minimum value of TCO (260 DU) found at the equatorial latitudes.
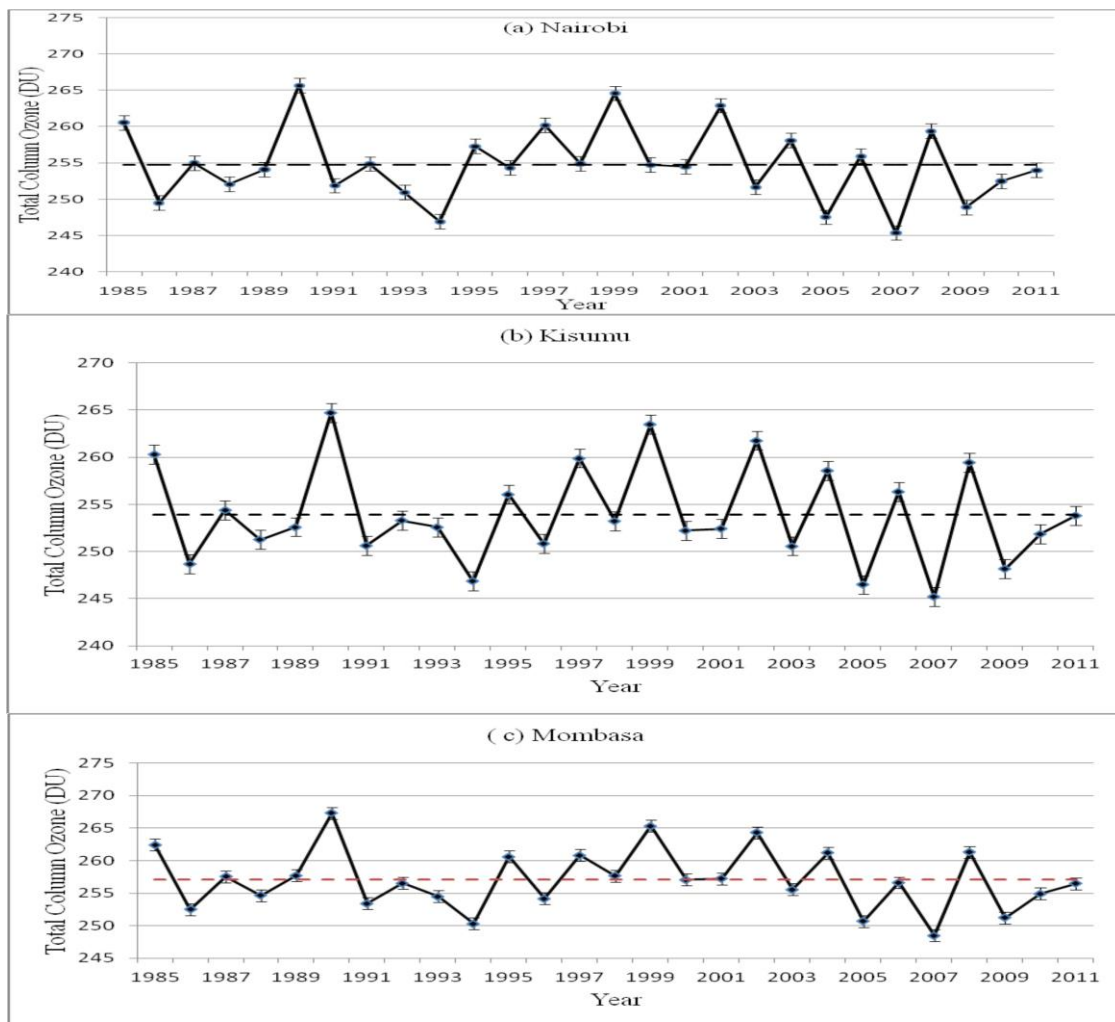
Figure 5.3 The time series of the TCO with normalized standard deviations for each year   observed in (a) Nairobi, (b) Kisumu and (c) Mombasa over 27 years period

Annual means and standard deviations of TCO estimated at Nairobi, Kisumu and Mombasa are 254.75 ± 5.17 DU, 253.92 ± 5.20 DU and 257.07 ± 4.70 DU respectively. The dashed line in Figure 5.3 indicates the annual mean TCO for each location. Annual mean TCO at Mombasa averaged higher than that at Kisumu and Nairobi. As we go from Kisumu to Mombasa, the TCO level is increased by 3.15 DU.

The maximum observed annual mean TCO over the Kenyan locations occurred at Mombasa (267.33 DU) in 1990. At Nairobi and Kisumu, a maximum value of 265.68 DU and 264.72 DU respectively and both in the year 1990. For the years analyzed, the minimum annual TCO values of 245.37 DU and 245.19 DU were found in 2007 for both Nairobi and Kisumu. At Mombasa, a minimum annual TCO value of 248.51 DU was observed in the year 2007.

Figure 5.4 shows that the value of TCO in all the three stations is below the recommended amount of (260 DU as in the tropics) in many of the years and that is also quite below the standard value of 300 DU in all the stations. Hence the maximum and minimum observed annual TCO occurred respectively in the year 1990 (267.33 DU) and in 2007 (245.19 DU). Throughout the study period, Mombasa recorded the highest value of TCO, followed by Nairobi while Kisumu recorded the lowest value of the TCO.
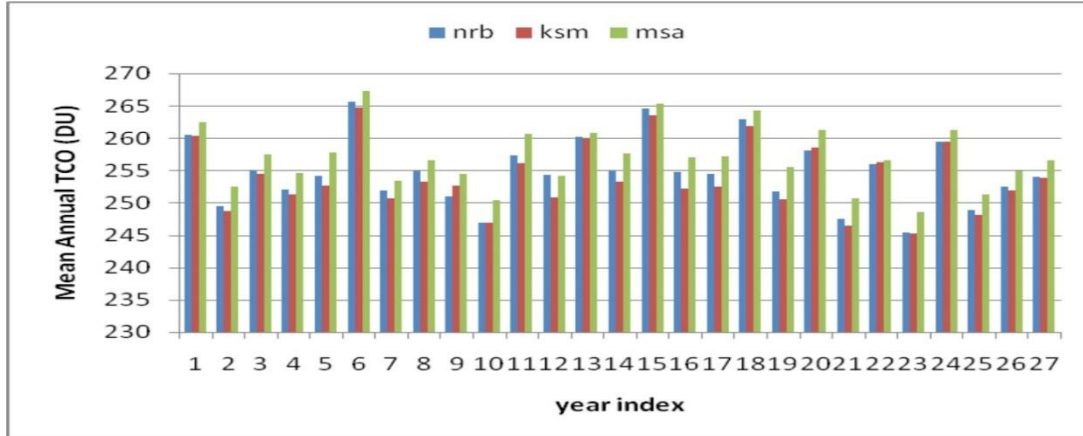
Figure 5.4 A comparison of TCO values at Nairobi, Kisumu and Mombasa over the period 1985-2011 with year index One = 1985 and year index 27 = 2011

5.2.1.1 Annual Variability

Percentage annual TCO variability is displayed in Figure 5.5. The yearly TCO percentage variability ranges between 1% to 6% with highest (5.76%) observed at Mombasa in 2010. Nairobi and Kisumu recorded 5.58% and 5.45% respectively in 1987. The lowest observed percentage TCO variability is at Kisumu (0.99%) in 2005 as compared to Nairobi (1.16%) and Mombasa (1.45%). The annual variability is attributed to the quasi-biennial oscillation (QBO) is a large-scale atmospheric phenomenon that causes year to year variability in the TCO distribution (Reid, 1994; Akinyemi, 2007).
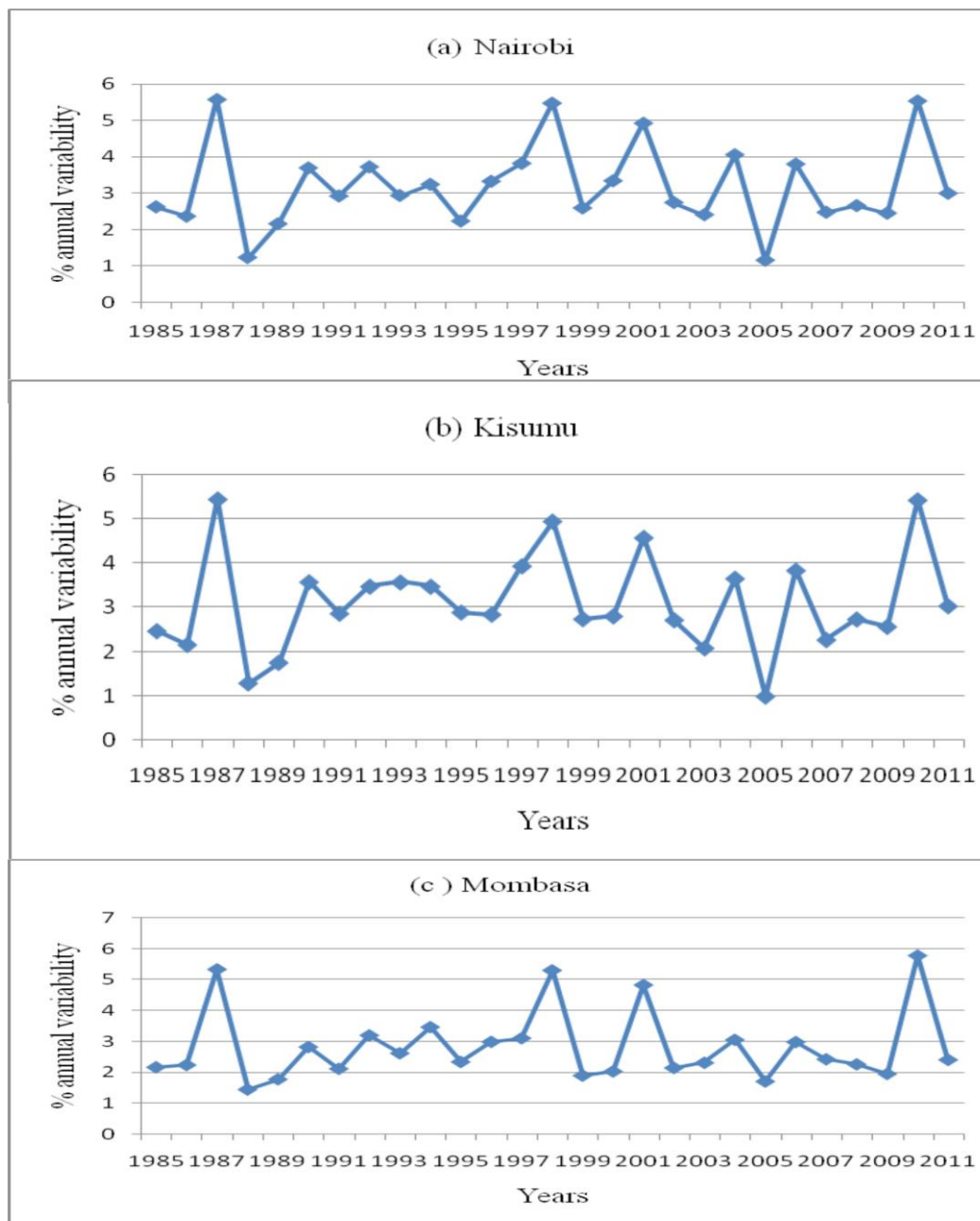
Figure 5.5 Annual mean percentage variation of TCO at (a) Nairobi, (b) Kisumu and (c) Mombasa

5.2.2 Monthly Trends

The monthly analyses of TCO for all considered cities show large variations of TCO throughout the months in the 27 years. Figure 5.6 illustrates the average monthly values of TCO of each month of the year for the three Kenyan cities and shows also the general picture of how TCO varied from January to December for all the years. The temporal patterns of mean monthly TCO for Nairobi, Kisumu and Mombasa showed a similar curved trend across the months with two maximum peaks. There was a maximum global peak in the month of September and a maximum local peak in the month of April for all the cities.

The maximum global peak is in the August – October season, which is just before the start of the short rains while the minor maximum peak is during the long rains in March – May. Hence, maximum values of TCO coincide with rainfall. Comparable results and pattern were observed by Thiong'o (2014), in his report during the ozone research managers.
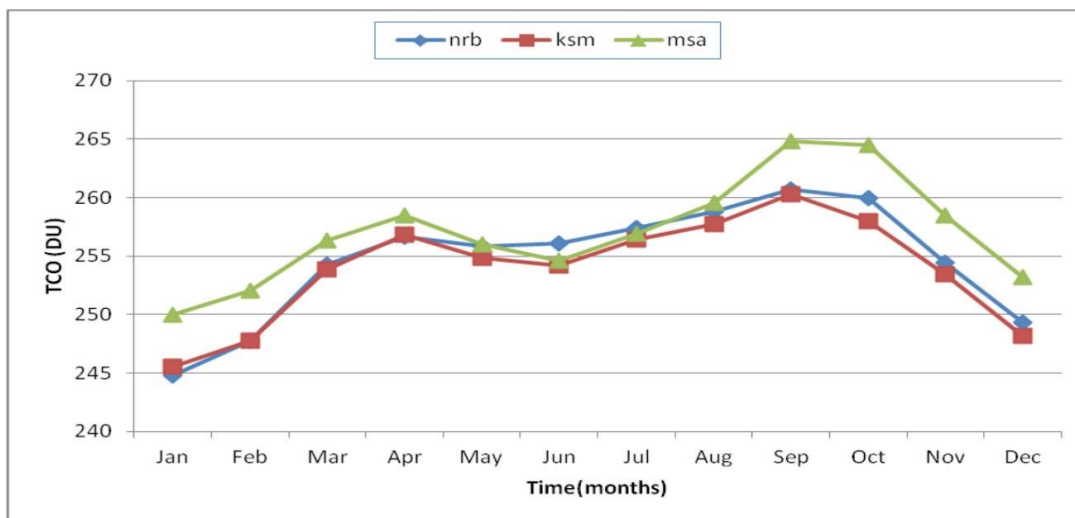
Figure 5.6 Seasonal variation of Total Column Ozone for all the years
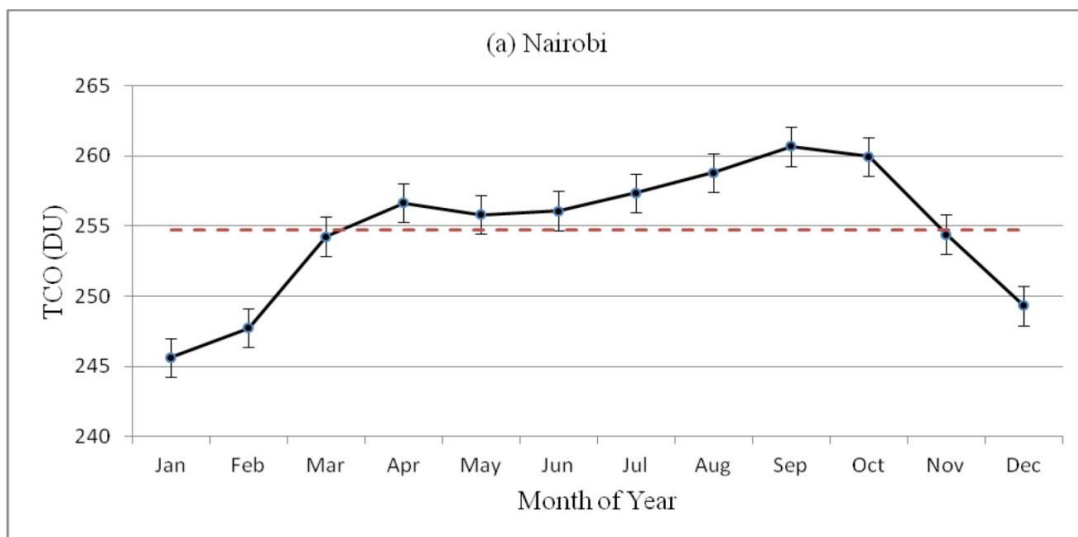
Figure 5.7 Plot of mean seasonal TCO variability measured at Nairobi
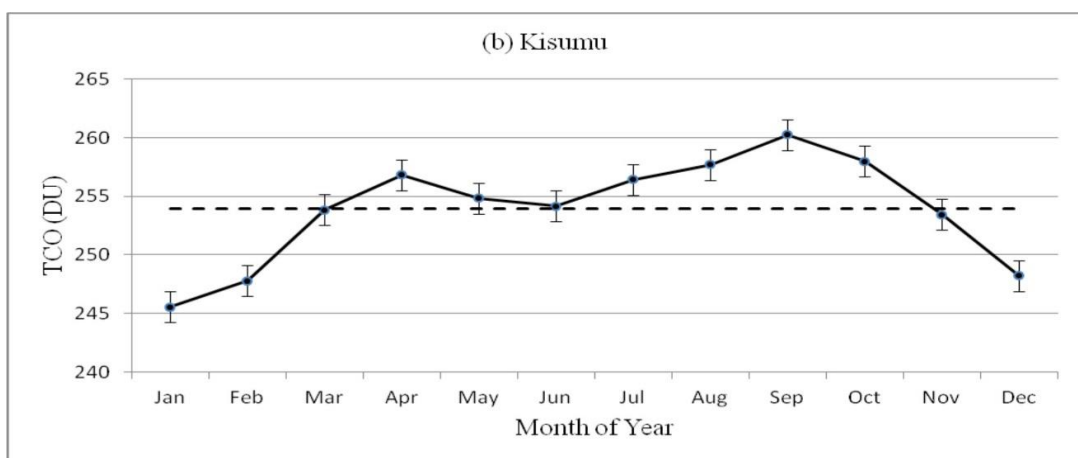
Figure 5.8 Plot of mean seasonal TCO variability measured at Kisumu
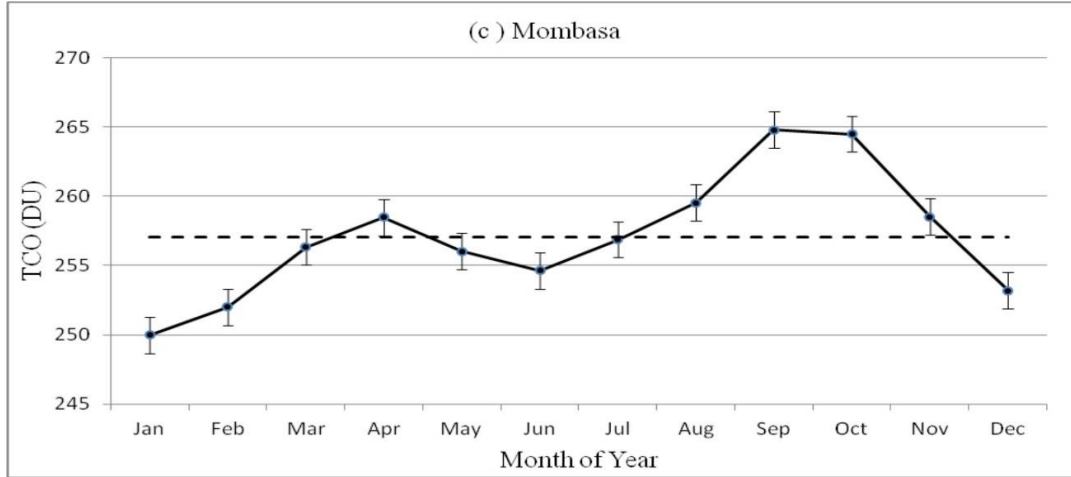
Figure 5.9 Plot of mean seasonal TCO variability measured at Mombasa

Figures 5.7- 5.9 show the mean seasonal variation of TCO observed at the three Kenyan cities with the normalized standard deviations for each month and a dotted horizontal line indicating the average TCO. A mean monthly TCO value of 254.74 ± 4.80 DU, 253.92 ± 4.55 DU and 257.07 ± 4.51 DU is observed in Nairobi, Kisumu and Mombasa respectively. Maximum and minimum values observed were respectively 260.68 DU and 245.65 DU at Nairobi; 260.25 DU and 245.54 DU at Kisumu; and 264.79 DU and 249.98 DU at Mombasa. These maximum and minimum values of TCO are observed in the months of September and January respectively.
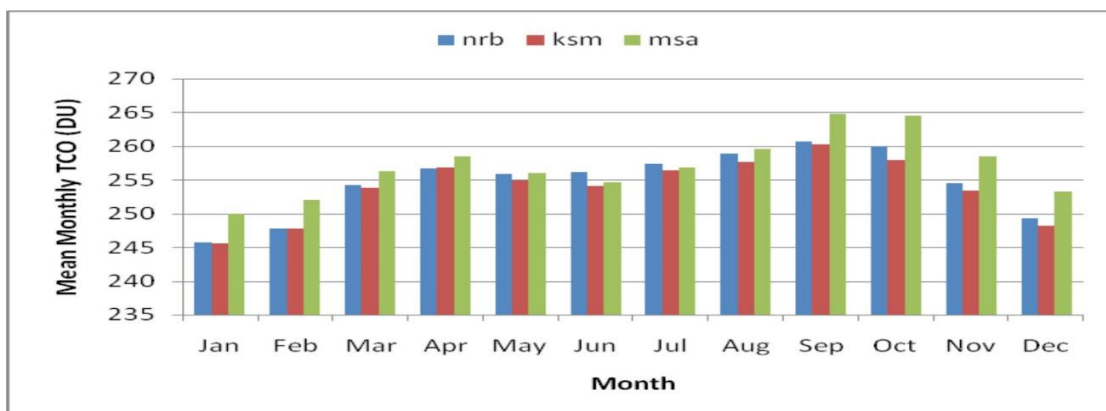
Figure 5.10 Average of mean monthly TCO values for the three Kenyan cities

The monthly analysis of TCO shows a lot of variations in ozone thickness throughout the year. There are only two months (September and October) at Mombasa and Nairobi during which ozone thickness remains at or far above the permissible limits of ozone of 260 DU near the equator. The rest of the months, for all the cities, the ozone layer becomes thin and the values of ozone calculated below the 260 DU mark (Figure 5.8).

It can also be noted from Figure 5.4 and Figure 5.8 that the values of TCO are functions of latitude. This can be seen from the values of TCO at different cities in each month and year. The higher values throughout the months of the years and the years occurred at Mombasa while the lowest occurred at Kisumu. This is attributed to latitudinal effects

5.3 Seasonal Variations

The percentage variability of TCO in the three cities was studied for each month of the year as reported in Figures 5.11 - 5.13. The seasonal variations of variability are in the range of between 2% − 4%. The highest percentage TCO variability is observed in June at Nairobi (3.91%) while Kisumu and Mombasa recorded the same value of Maximum (3.70%) in December and minimum value of 2.87 % in October. All the cities recorded a minimum value in the month of October as displayed in Figure 5.11 − 5.13. Solar

activity as well as wind transport could be associated with these variations in TCO (Bish, Pande, Chandra & Pande, 2014)
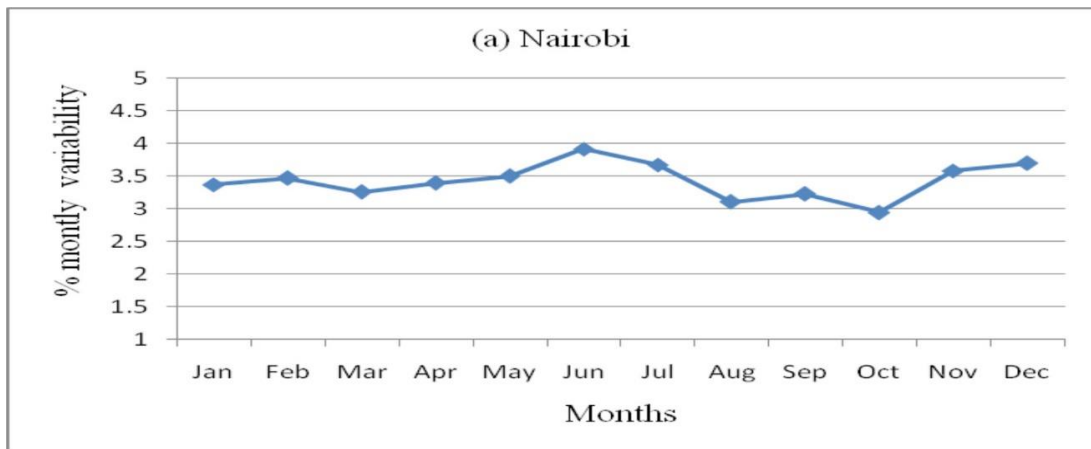
Figure 5.11 Mean seasonal variations of the month to month percentage variability for TCO at Nairobi
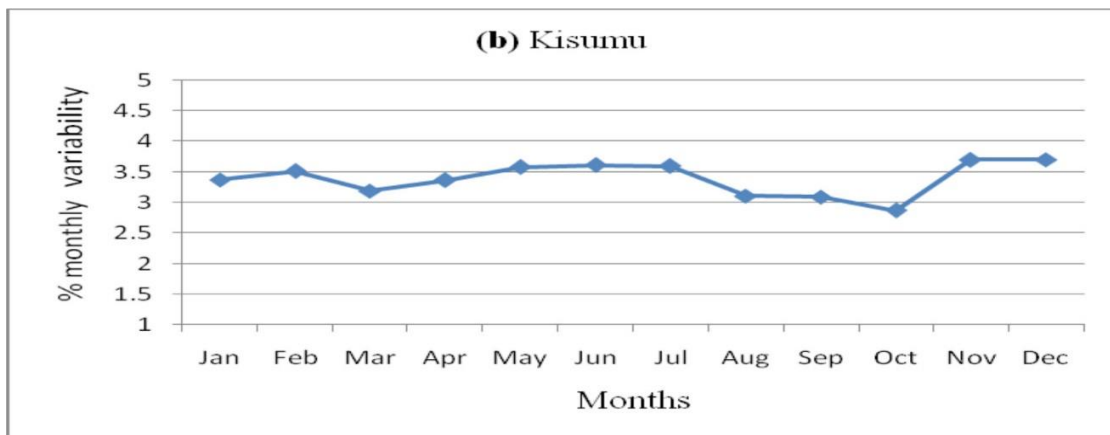
Figure 5.12 Mean seasonal variations of the month to month percentage variability for TCO at Kisumu
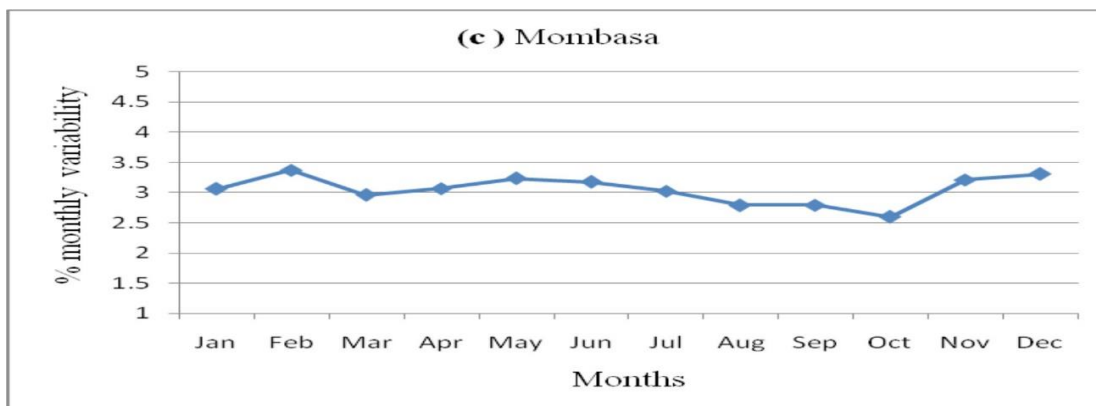
Figure 5.13 Mean seasonal variations of the month to month percentage variability for TCO at Mombasa

Kenya has four seasons; long rains season from March – May, dry-cold season from June – August, a short rain season from September to November and lastly a dry hot season from December to February (Kenya meteorological department, 2016).
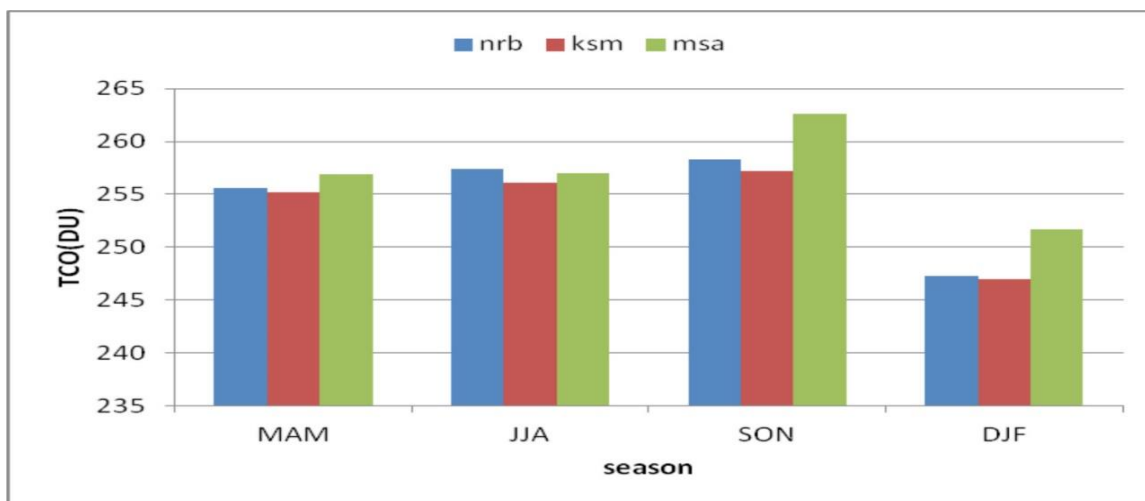
Figure 5.14 The average of the seasonal values for the three cities; Nairobi (nrb), Kisumu (ksm) and Mombasa (msa)

Ayoma, Gilbert and Bertrand (2004) reported total ozone measurements over Nairobi with a Dobson instrument, confirming maximum total ozone content during the short rainy season and a minimum in the warm-dry season. Muthama (1989), using Dobson

instrument, showed that minimum total ozone amount occurred around January and February (the warm-dry season) and maximum during September and October (the short rainy season).

Monthly mean values of TCO show distinct seasonal variation with minimum and maximum values occurring in warm -dry season and short rain season respectively. This shows that various air mass circulation specific to each season are responsible for the variability of TCO therefore ozone concentration will vary depending on the season of the year. Ozone exchange between the stratospheric and tropospheric occurs seasonally (Diab, Thompson, Mari, Ramsay & Coetzee, 2004). Using the ground based measurements, Diab et al., (2004) were able to show the seasonal variations over Irene in South Africa. Hence, the QBO acts to increase the stratosphere – troposphere ozone exchange since it is considered to be the cause of circulation in the upper level atmosphere.

Table 5.2 Seasonal analysis of the total change in TCO over the Kenyan cities 1985 – 2011

	TCO					
	Nairobi/yr	Total change	Kisumu/yr	Total change	Mombasa/yr	Total change
DJF	0.012	0.324	0.007	0.189	-0.046	-1.242
MAM	0.026	0.702	0.033	0.891	0.019	0.513
JJA	-0.174	-4.698	-0.139	-3.753	-0.146	-3.942
SON	-0.223	-6.021	-0.237	-6.399	-0.191	-5.157

Table 5.2 shows the seasonal analysis of the total change in TCO in Nairobi, Kisumu and Mombasa during the study period. The maximum decline change in TCO thickness is found in the SON months of short rainy season for all the cities with Kisumu registering the highest change of – 6.4 DU while Mombasa registered the lowest change of -5.2 DU during this season. The minimum decline change in TCO thickness is found in the DJF months of dry hot season.

5.4 SAI Descriptive Statistics Analysis

The various statistical attributes of SAI variables during the study periods are reported in Table 5.3.

Table 5.3 Descriptive Statistics of mean monthly SAI variables between January 1985 and December 2011

Variable	mean	SD	Range	Maximum	Minimum
ssn	57.77	50.81	200.00	200.00	0.00
sf	117.82	49.02	182.35	247.20	64.86
mg	0.271	0.006	0.025	0.2880	0.263

5.5 SAI Trends

The mean monthly SAI time series from 1985 - 2011 are reported in Figures 5.15 (a) – (c). A decrease in ssn, sf and mg with time is observed. The decrease is attributed to declining solar activity since all the indices of solar activity are in most cases closely related as the main source of all their variations is variable magnetic field. The trends are different but at significant levels for each SAI variable as reported by the linear fits in Table 5.4.

The linear trends suggest that, over the 27 year period of study, a decrease of 94% of the mean for ssn, 34 % of the mean for sf and $\approx$ 2 % of the mean for mg. Hence there is a decreasing trend of SAI variables showing that during the study period, SAI is decreasing with highest decrease in ssn and least in mg.
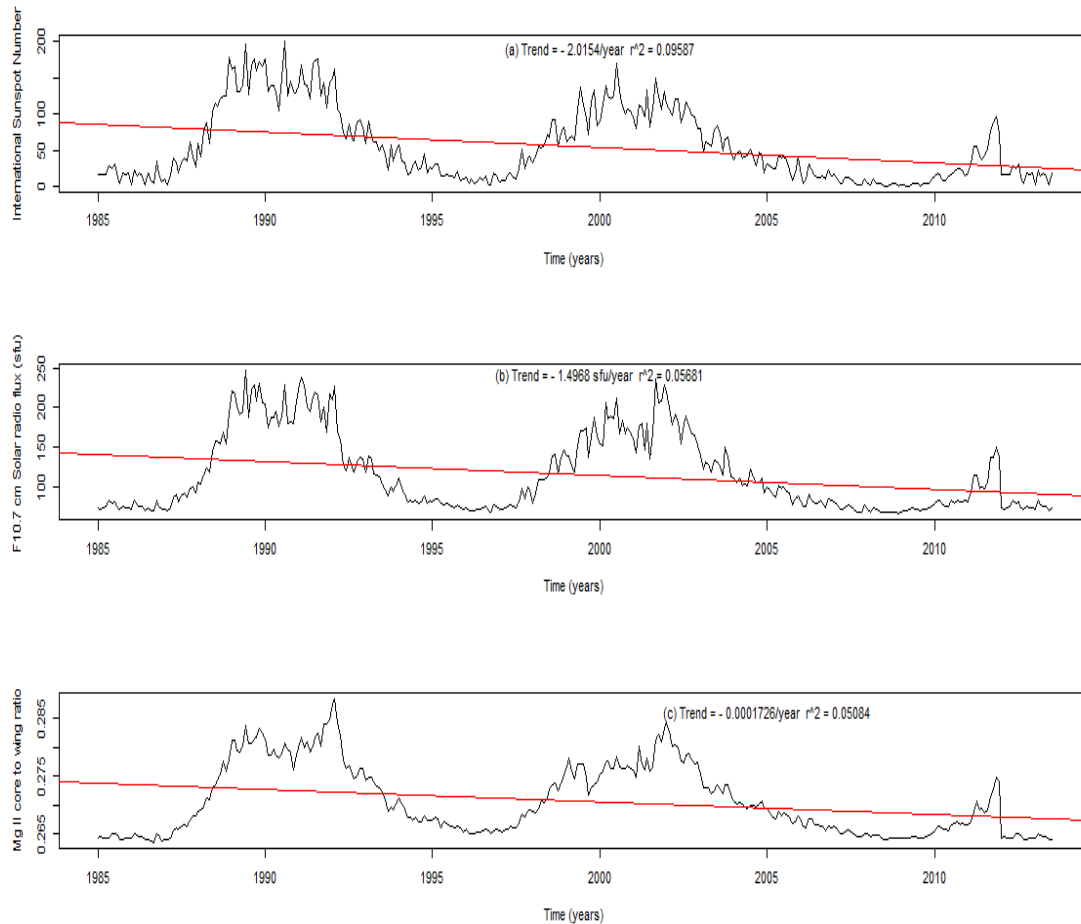
Figure 5.15 Mean monthly time series for SAI variables (a) international sunspot number (ssn), (b) F10.7cm solar radio flux (sf) and (c) Mg II core to wing ratio (mg) from 1985 – 2011 with their linear fits.

Table 5.4 Trends derived from linear fits to the mean monthly SAI time series from 1985 – 2011

Variables	Trend/yr.	r^2	p values
ssn	- 2.0154±0.3449	0.09587	< 0.001
sf	- 1.4968±0.3399 sfu	0.05681	< 0.001
mg	- 0.0001726±0.0004.183	0.05084	< 0.001

5.6 Pearson Correlation Analysis

Pearson correlation analyses were performed relating mean monthly TCO at the three cities, monthly SAI variables and mean monthly TCO at the three cities to monthly SAI variables. Figure 5.16 shows the distribution of each variable on the diagonal. On the bottom of the diagonal, the bivariate scatter plots with a fitted line are displayed while on the top of the diagonal, the value of the correlation and the significance level as stars are displayed.

Pearson's correlation analysis demonstrate that TCO at Nairobi, Kisumu and Mombasa are highly correlated with each other at $p < 0.001$ (2- tailed) significant level. This is attributed to the fact that spatial dependence on TCO varies strongly with latitude hence TCO between locations show high positive correlation with nearby locations and the correlation decreases (south to north) for far away locations (Stein, 2002). The highest correlation of 0.955 is found to exist between TCO at Nairobi and Kisumu (Table 5.5).

A lowest correlation coefficient of 0.936 is observed between TCO at Nairobi and Mombasa among the cities.
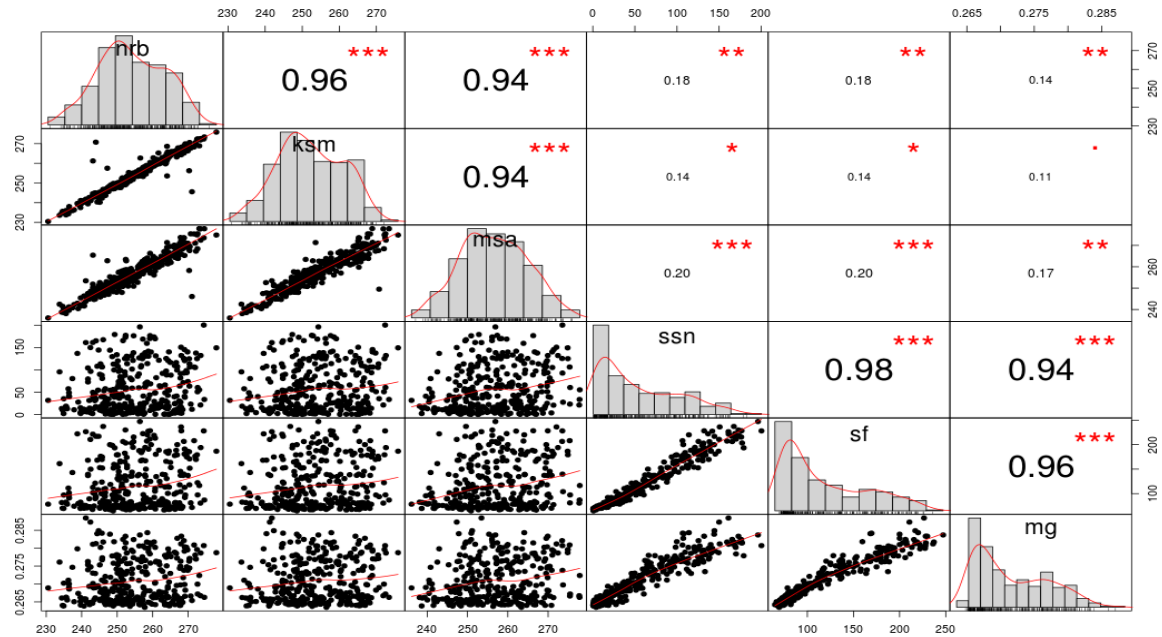
*P-values (0, 0.001, 0.01, 0.05, 0.1, 1) <=> symbols ("***", "**", "*", ".", " ") ,2 − tailed.*

Figure 5.16 Correlation matrix of TCO (nrb, ksm and msa) and the SAI variables (ssn, sf and mg)

Table 5.5 Association among mean monthly TCO at the three cities for the period 1985 – 2011 and significant level

	TCO (nrb)	p	TCO (ksm)	p	TCO (msa)
TCO (nrb)	1				
TCO (ksm)	0.955	< 0.001	1		
TCO (msa)	0.936	< 0.001	0.938	< 0.001	1

The association among the SAI variables is shown in Table 5.6. SAI variables are also highly correlated with each other at p < 0.001 (2- tailed) significant level with highest correlation coefficient for the association between ssn and sf (r = 0.976, p < 0.001). The association between ssn and mg (r = 0.941, p< 0.001) is the least. sf and mg has a correlation of (r = 0.960 , p < 0.001).

Table 5.6 Association among mean monthly SAI variables (ssn, sf and mg) for the period 1985 – 2011 and the level of significance

	ssn	p	sf	p	mg
ssn	1				
sf	0.976	< 0.001	1		
mg	0.941	< 0.001	0.960	< 0.001	1

These results agree well with Pearson's correlation coefficient between F10.7 cm solar radio flux and international sunspot number values range between 0.94 and 0.98 (Tharshini & Shanthi, 2015). Hathaway, Nandy, Wilson and Reichmann (2003) reported that a correlation between F10.7 cm solar radio flux and relative sunspot number exceeds 0.98.

The high correlation coefficient between F10.7 cm solar radio flux and international sunspot number and also between F10.7 cm solar radio flux and Mg II core-to-wing ratio is attributed to the fact that F10.7 cm solar radio flux comes from high part of

chromosphere and lower part of corona of the sun where it tracks other important emissions that form in the same region of the solar atmosphere (Tapping, 2013).

High degree of correlation of F10.7 cm solar radio flux and Mg II core-to-wing ratio suggests dependency upon common plasma parameters and that their sources are spatially close. High correlation between international sunspot number and Mg II core-to-wing ratio is attributed to the 280 nm Mg II solar spectral band containing photospheric continuum and chromospheric line emission hence chromospheric in origin while weakly varying wings or nearby continuum are photospheric in origin.

The monthly averaged ssn, monthly averaged sf and monthly averaged mg (Table 5.7), correlations though low, are significantly positively correlated with monthly mean TCO over the study period. Among the SAI variables, sf is most closely correlated to monthly TCO at nrb ($r = 0.1753$, $p < 0.05$) and Mombasa ($r = 0.2039$, $p<0.001$) while ssn is most correlated to monthly TCO at Kisumu ($r = 0.1372$, $p< 0.05$. Mg was least correlated to monthly TCO at nrb ($r = 0.1440$, $p< 0.05$), at ksm ($r = 0.1089$, $p <0.05$) and at msa ($r = 0.1740$, $p <0.05$). This could be attributed to delayed impact by mg on TCO while ssn and sf have direct impact on TCO.

 It can also be noted that the SAI and TCO correlation values are highest in Mombasa and lowest Kisumu. Though there is positive correlation between SAI and TCO for all the stations, the correlation increases from low latitude (Kisumu) to high latitude (Mombasa). Hence TCO variation at higher latitudes is more influenced by SAI than at low latitude and variations of TCO is approximately in phase with the solar cycle (Madhu & Gangadharan, 2016)

Correlation of SAI and ozone is due to the fact that most of the solar EUV radiation is absorbed in the upper terrestrial atmosphere some of which include international sunspot number, F10.7 cm solar radio flux and Mg II core-to-wing ratio. Correlation in the equatorial region is low where ozone is produced and in the sub Polar Regions where the larger amounts of ozone is found. The effect could be, according to Labitzke and Van

Loon (1997) due to solar induced changes on the pole ward transport of ozone rather than of due to radiative interaction between sun and ozone (Tsiropoula, 2003).

Table 5.7 Association between mean monthly TCO and mean monthly SAI variables for the period 1985 – 2011 and their level of significance

	TCO (nrb)	p	TCO (ksm)	p	TCO (msa)	p
ssn	0.1750	0.00156[**]	0.1372	0.0134[*]	0.1974	0.000351[***]
sf	0.1753	0.0153[**]	0.1368	0.0137[*]	0.2039	0.000220[***]
mg	0.1440	0.00293[**]	0.1089	0.00768[**]	0.1740	0.000729[***]

Signif. Codes 0***, 0.001**, 0.01*

Hence Pearson analysis demonstrates that TCO at all the cities are highly correlated among each other at $p < 0.001$ (2- tailed) significant level. All correlations are positive and highest correlation is found to exist between TCO at Nairobi and TCO at Kisumu. SAI variables are also positive and highly correlated among each other with the highest correlation coefficient (0.976) between ssn and sf. SAI variables are found to bear a significant correlation with mean monthly TCO. This shows that solar activity indices have significant contribution in the variation of stratospheric ozone (Isikwue et al., 2010).

5.7 Cross correlation

Cross correlation function between the time series of TCO at each city and SAI variables is performed and the time lags of SAI preceding TCO at which the series showed strongest (maximum) and minimum correlation is then determined at different cities as reported in Table 5.8.

ssn exhibited the same maximum lag month 0 at Nairobi (r = 0.175) and Mombasa (r = 0.197) but a different maximum correlation coefficient (r = 0.140) at lag month 11 at Kisumu. A minimum correlation coefficient of 0.112 and 0.139 are observed between ssn and TCO at Nairobi and Mombasa respectively at lag month 6. A minimum

correlation of 0.0870 at lag month 5 is observed at Kisumu. sf exhibited the same maximum at lag month 0 at all the cities while a local minimum varied between lags 4 to 6. mg increases gradually from lag 0 to a maximum value at lag month 9 and then drops to its minimum value at lag month 12 (Figure 5.17 – 5.19). mg showed a constant local maximum and minimum cross correlation at lag months 9 and 12 respectively at all the cities.

The lag months for ssn and sf (Table 5.8) are shorter ($\leq$ - 6) than lag months for mg (- 9 and - 12), except in Kisumu where a large lag month of - 11 is observed to give a maximum correlation of 0.140 between TCO and ssn. Hence sf has an immediate impact on TCO at all the cities while ssn has immediate impact on TCO at Nairobi and Mombasa. But a delayed impact at Kisumu. mg has a delayed impact on TCO at all the cities. This has an effect on the ozone variability.

Table 5.8 Cross correlation coefficients and lags (in months) between SAI and TCO

TCO		ssn	lag/months	sf	lag/months	mg	lag/months
nrb	Max	0.175	0	0.175	0	0.167	- 9
	Min	0.112	- 6	0.123	- 6	0.123	- 12
ksm	Max	0.140	- 11	0.137	0	0.150	- 9
	Min	0.0870	- 5	0.0980	- 4, - 5	0.108	- 12
msa	Max	0.197	0	0.204	0	0.190	- 9
	Min	0.139	- 6	0.140	- 5	0.142	- 12

Figures 5.17, 5.18 and 5.19 reports the local maximum and minimum of the lagged cross correlation monthly mean TCO respectively at Nairobi, Kisumu and Mombasa and the SAI over the study period. ssn and sf patterns are similar. Both start at a higher coefficient value at zero month then drop gradually up to lag months; - 6 at Nairobi, - 4 and - 5 at Kisumu and 5 at Mombasa. The correlation starts to increase up to lag month - 10 and again decreases. The difference in the patterns is attributed to decreased accuracy during solar minimum which is exhibited by ssn and sf, not mg. Also, mg is a ratio and hence less sensitive to artifacts and instrumental degradation than a non-ratio measurement (Suess, Snow, Viereck & Machol, 2016).
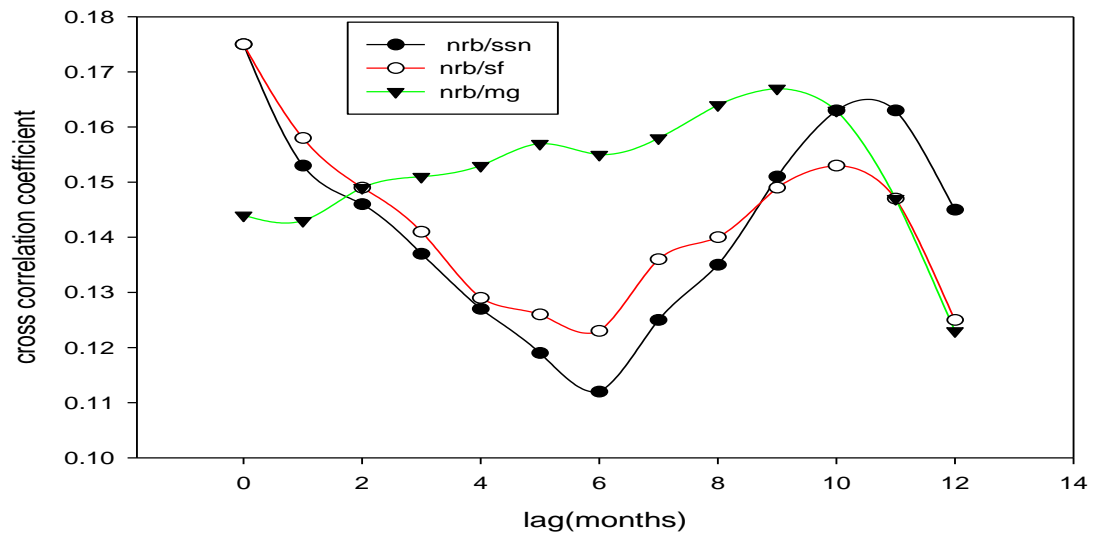
Figure 5.17 Plots of lagged cross correlation of monthly mean TCO at Nairobi and averaged SAI variables over the study period 1985 - 2011
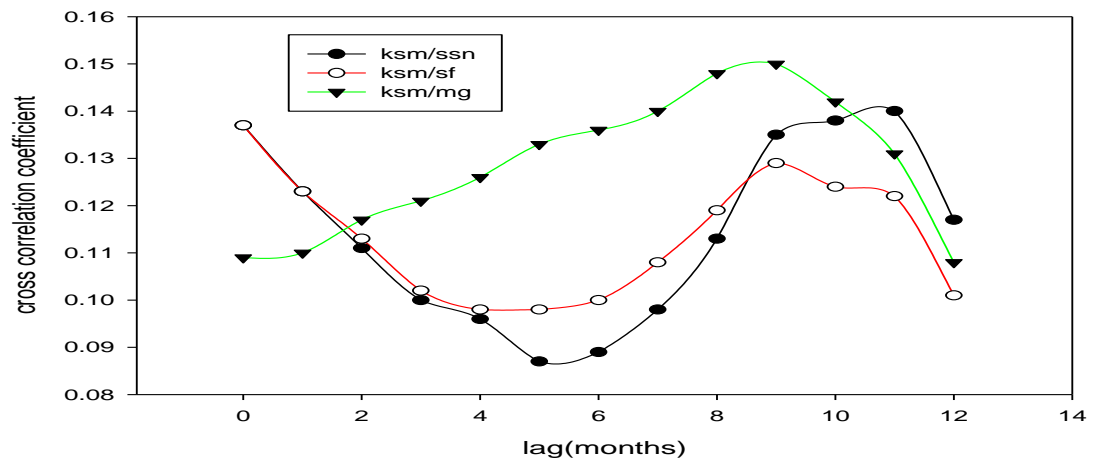
Figure 5.18 Plots of lagged cross correlation of monthly mean TCO at Kisumu and averaged SAI variables over the study period 1985 - 2011
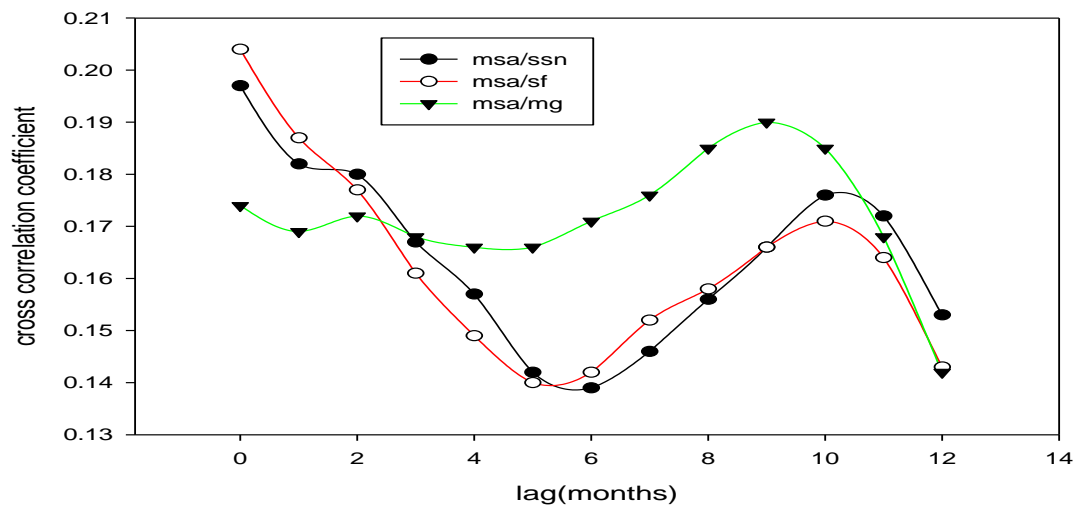
Figure 5.19 Plots of lagged cross correlation of monthly mean TCO at Mombasa and averaged SAI variables over the study period 1985 – 2011

Hence the mean monthly TCO and mean monthly SAI variables have correlations at both long and short lags. Positive maximum correlation is again observed between TCO at all the cities and SAI variables. A local maximum cross correlation between mean monthly TCO and mean monthly SAI variables is observed when ssn and sf variables are at month zero lag with TCO at all the cities as reported in Figure 5.17 for Nairobi, Figure 5.18 for Kisumu and Figure 5.19 for Mombasa. A lag month of - 9 is observed between mg and TCO at all the cities to give a maximum correlation.

5.8 Linear Regression Analysis.

Tables 5.9 (a) – (c) show the results attained after subjecting both the mean monthly TCO at the three cities and SAI variables to linear regression. Linear regression analysis gave the correlation coefficient between TCO and SAI variables as 0.1750, 0.1753 and 0.1671 for ssn, sf and mg respectively at Nairobi, as 0.1372, 0.1368 and 0.1499 for ssn, sf and mg respectively at Kisumu and as 0.1974, 0.2043 and 0.1894 for ssn, sf and mg respectively at respectively at Mombasa.

112

Table 5.9 (a) Results of linear regression and t-test for mean monthly TCO and mean monthly SAI at Nairobi

TCO	intercept	slope	r	r^2	t value	$Pr(> |t|)$
ssn	252.81051	0.03362	0.1750	0.03063	3.190	0.00156[**]
sf	250.64016	0.03490	0.1753	0.03073	3.195	0.00153[**]
mg	181.760	268.620	0.1671	0.02793	2.999	0.00293[**]

Signif. Codes: ** 0.001

Table 5.9 (b) Results of linear regression and t-test for mean monthly TCO and mean monthly SAI at Kisumu

TCO	intercept	slope	r	r^2	t value	$Pr(> |t|)$
ssn	252.42988	0.02576	0.1372	0.01882	2.486	0.0134[*]
sf	250.78070	0.02663	0.1368	0.01872	2.479	0.0137[*]
mg	189.960	235.170	0.1499	0.02248	2.683	0.00768[**]

Signif. Codes: 0.001 '**' 0.01 '*'

Table 5.9 (c) Results of linear regression and t-test for mean monthly TCO and mean monthly SAI at Mombasa

TCO	intercept	slope	r	r^2	t value	Pr$(> |t|)$
ssn	255.08534	0.03435	0.1974	0.03895	3.613	0.000351[***]
sf	252.73619	0.03678	0.2043	0.04175	3.737	0.000220[***]
mg	182.044	276.413	0.1894	0.03586	3.412	0.000729[***]

Signif. Codes: 0 '***'

The straight line probabilistic model has slopes, intercepts and coefficient of determination values given in Table 5.9 (a) – (c) for the respective cities. The least square prediction equation is given as:

Nairobi;	TCO = 252.81051 + 0.03362 ssn	(5.1a)
	TCO = 250.64016 + 0.03490 sf	(5.1b)
	TCO = 181.760 + 268.620 mg	(5.1c)
Kisumu;	TCO = 252.42988 + 0.02576 ssn	(5.2a)
	TCO = 250.78070 + 0.02663 sf	(5.2b)
	TCO = 189.960 + 235.170 mg	(5.2c)
Mombasa;	TCO = 255.08534 + 0.03435 ssn	(5.3a)
	TCO = 252.73619 + 0.03678 sf	(5.3b)
	TCO = 182.040 + 276.413 mg	(5.3c)

The significance of these linear dependence were justified by the t – test where the t – statistic values were 3.190, 3.195, 2.999 for ssn, sf and mg at Nairobi; 2.486, 2.479 and 2.683for ssn, sf and mg at Kisumu and 3.613, 3.737, 3.412 for ssn, sf and mg at Mombasa. Since the P-values were less than the significance level (0.05), the null hypothesis was rejected and the alternate hypothesis accepted. Therefore, there is a significant linear relationship between sunspot numbers; F10.7 cm solar radio flux; Mg

II core to wing ration and TCO at each city. Hence there is a relationship between ozone concentration and solar indices at each station.

Table 5.10 (a) ANOVA table for Nairobi

TCO	F value	$Pr(> F)$
ssn	10.175	0.001564^{**}
sf	10.210	0.001535^{**}
mg	9.017	0.002926^{**}

Signif. Codes: 0.001^{**}

Table 5.10 (b) ANOVA table for Kisumu

TCO	F value	$Pr(> F)$
ssn	6.1778	0.01344^{*}
sf	6.1442	0.01370*
mg	3.861	0.007684^{**}

Signif. Codes: $0.001^{**}\ 0.01^{*}$

Table 5.10 (c) ANOVA table for Mombasa

TCO	F value	$Pr(> F)$
ssn	13.051	0.0003515^{***}
sf	13.966	0.0002201^{***}
mg	10.050	0.0007293^{***}

Signif. Codes: 0^{***}

The linear dependence was further confirmed by the ANOVA results as the P values of all the calculated F – values at the three cities and their corresponding SAI variables Table 5.10(a) – (c) were less than the significance level (0.05)

Hence these results reveal that the mean monthly TCO at Nairobi, Kisumu and Mombasa have positive correlation with SAI variables. A linear relationship exists between the two variables in all the cities. The best fit equations 5.1(a) – 5.1(c) for Nairobi, Equations 5.2(a) – 5.2(c) for Kisumu and equations 5.3(a) – 5.3(c) for Mombasa suggest an increase in TCO of about 2 – 3 % (Nairobi), 1 – 2% (Kisumu) and 3 – 4 % (Mombasa) is attributed to solar activity indices; ssn, sf and mg. According to WMO ozone assessment (1995), the global average TCO changes with solar variations in the 11-year solar cycle changes by about 1 – 5 %.

5.9 Solar Forcing Effect

A linear multivariate model of the form

$$y = b_0 + b_1 ssn + b_2 sf + b_3\, mg$$

(5.4

Where y is the mean monthly TCO, b_0, b_1, b_2 and b_3 are the coefficients determined by the least square fittings. The coefficients are presented in the multivariate models 5.5 to 5.7;

$$TCO_{nrb} = 382.58354 + 0.02036\, ssn + 0.07412 sf - 508.24278 mg$$

(5.5)

$$TCO_{ksm} = 370.28900 + 0.01859 ssn + 0.06200 sf - 460.30874 mg$$

(5.6)

$$TCO_{msa} = 356.70976 - 0.00279 ssn + 0.08728\, sf - 405.00741 mg$$

(5.7)

Models in equations 5.5 to 5.7 show solar forcing of TCO at the cities under study. Models in equations 5.5 and 5.6 show direct forcing of sf and ssn, but a negative forcing of mg at Nairobi and Kisumu. All the models indicate direct forcing of sf and inverse forcing of mg at Nairobi, Kisumu and Mombasa. A direct forcing of ssn is indicated

only at Nairobi and Kisumu. The high coefficients of mg in the models indicate that forcing due to the chromosphere and hence the solar ultraviolet radiation is more prominent on TCO during this study period compared to the photosphere and corona (Ndeda, Rabiu, Ngoo & Ouma, 2011).

Table 5.11 Multiple Correlation Coefficients Results

Model equation	R	R^2	p
5.5	0.196825	0.03874	0.005425[***]
5.6	0.160000	0.025600	0.03995[*]
5.7	0.218128	0.04758	0.001354[**]

Signif. Codes: 0.001'[***]' 0.01 '[**]' 0.05'[*]' (2 – tailed)

The multiple correlation coefficients, R and the significant levels for the three cities are shown in Table 5.11. At Nairobi (R = 0.196825, p = 0.01), Kisumu (R = 0.1600, p < 0.05) and Mombasa (R = 0.218128, p = 0.001) are obtained. Hence 4%, 3% and 5% of the TCO at Nairobi, Kisumu and Mombasa can be predicted by the SAI variables.

5.10 Spectra Analysis

Spectral analysis was applied to identify the frequency dependency of variability. Figure 5.20 shows the periodograms of TCO over Nairobi, Kisumu and Mombasa obtained from the spectral analysis. All the cities showed similarity in power spectra for TCO.
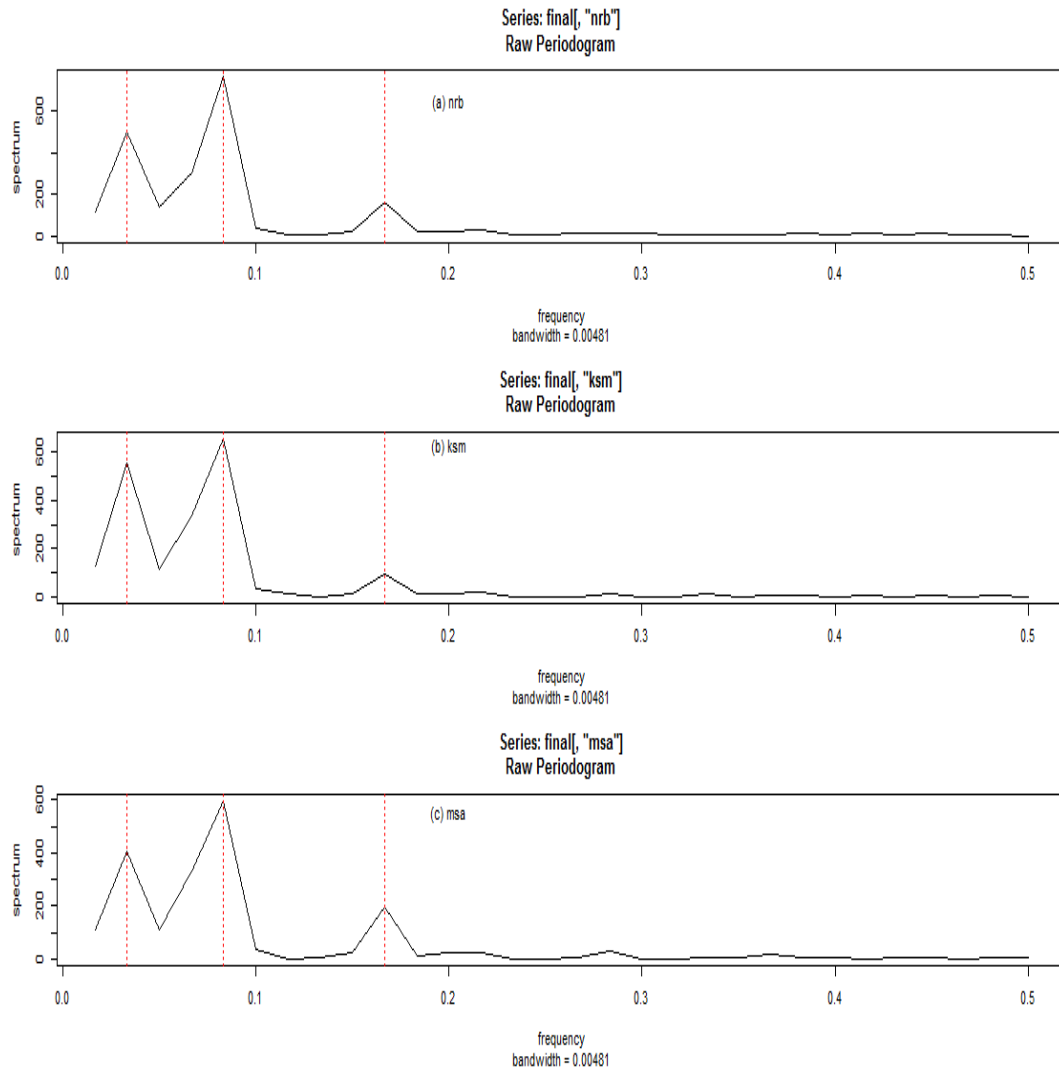
Figure 5.20 Results of the power spectra obtained for TCO over Nairobi, Kisumu and Mombasa

Three major periods (30, 12 and 6 months) periodicities are observed in all the cities. The 12 months period was the most dominant in the TCO. The maximum spectral density estimated for these period are respectively 765.23 W/Hz (Nairobi), 651.45 W/Hz (Kisumu) and 597.21 W/Hz (Mombasa). The 6 month and the 12 months period are a demonstration of semiannual effect in the atmosphere and a manifestation of the annual effect respectively. According to Russell and McPherron (1973) and Clua de Gonzalez,

118

Silbergleit, Gonzaleg & Tsurutani (2001), the semiannual changes in the atmosphere are related to solar activity.

The 30 month period is approximately the quasi biennial oscillation (QBO) periodicity. QBO signals have been identified in a number of geophysical parameters such as ozone distribution and its existence has been shown in solar activity parameters such as sunspot numbers and F10.7 cm solar radio flux (Ndeda, 2013).The 30 month period is more than the QBO periodicity. There are small scale $(2 - 4)$ month periodicities in TCO over all the cities which could be treated as noise in the TCO.

5.11 Modeling and Prediction of TCO

Performing the training process of MLR and MLFNN models using the package neuralnet (Gunter and Fritsch, 2008) in R software, the simulator iteratively adjusted the weights until the error between the output (predicted) data and the actual data (observed) was minimized. Several network factors such as momentum, learning rate, number of hidden nodes, and thresholds were tried during the training process to improve network generalization and prediction accuracy. The best results obtained for MLR (Table 5.14 – 5.16) and Table 5.18 for MLFNN when continuous training was completed, that is, the error is minimized.

5.11.1 Data Partitioning

Table 5.12 and Table 5.13 show how data were partitioned into the three samples.

Table 5.12 Partitioning of the Time Series Data from 1985 - 2011

Data Partition	Percentage	Data Points	Purpose
Training set	75	243	In sample data to train the models
Testing set	25	81	Independent set used to track error during training.
Total	100	324	

Table 5.13 Hold Out Data Sample from January 2012 to August 2013

Data sample	Data points	Purpose
Hold out sample	20	Independent set of data used to assess the final model

The remaining 25%, or 81 cases, were excluded from the training set and used later, after the model was developed, to test the model's performance. The hold out data sample was another independent set of data records used to assess the final models. The error for the hold out sample gave an honest estimate of the predictive ability of the model because the hold out cases is not used to build the model.

5.11.2 MLR Model Results

The MLR was considered using all the three prediction variables. Stepwise regression results obtained on the modeling dataset are shown in Table 5.14 for Nairobi, Table 5.15 for Kisumu and Table 5.16 for Mombasa. From the regression output, only one predictor variable namely mg was significant in affecting TCO prediction in all the three cities.

The significant estimated parameters were found to be; Nairobi (b_0 = 454.60685 and b_3 = -784.74311); Kisumu (b_0 = 436.26008 and b_3 = -714.75563) and Mombasa (b_0 = 406.64225 and b_3 = -595.99994).

Table 5.14 MLR Model Results for Nairobi

	Estimate	Std error	t- value	Pr (>|t|)
Intercept	454.6069	94.7353	4.799	0.00000281***
ssn	0.03206	0.05709	0.562	0.5750
sf	0.09052	0.07352	1.231	0.2195
mg	-784.74311	368.20025	-2.131	0.0341*

Multiple R-squared: 0.04215

Adjusted R-squared: 0.03013   F- statistic: 3.506 on 3 and 239 DF

p- value: 0.01608

Signif. Codes: 0.001 '*' 0.05 '*'**

Table 5.15 MLR Model Results for Kisumu

	Estimate	Std error	t- value	Pr (>|t|)
Intercept	436.26008	92.97972	4.692	0.00000456***
ssn	0.02693	0.05604	0.481	0.6312
sf	0.08022	0.07216	1.112	0.2674
mg	-714.75563	361.37694	-1.978	0.0491*

Multiple R-squared: 0.03061

Adjusted R-squared: 0.01845   F- statistic: 2.516   on 3 and 239 DF

p- value: 0.05895

Signif. Codes: 0.001 '*' 0.05 '*'**

Table 5.16 MLR model results for Mombasa

	Estimate	Std error	t- value	Pr (>|t|)
Intercept	406.64225	84.71908	4.800	0.00000280***
ssn	0.01217	0.05106	0.2380	0.8118
sf	0.09262	0.06575	1.409	0.1602
mg	-595.99994	329.270.97	-1.810	0.0715·

Multiple R-squared: 0.04977

Adjusted R-squared: 0.03785   F- statistic: 4.173 on 3 and 239 DF

p- value: 0.006642

Signif. Codes: 0.001 '' 0.05 '*'**

The constants b_0, b_1, b_2 and b_3. are the regression parameters computed by the method of least squares. In the present study, the regressions (best fit equations) are given as:

$$\text{TCO}_{(nrb)} = 454.60685 + 0.03206 \, \text{ssn} + 0.09052 \, \text{sf} - 784.74311 \, \text{mg} \qquad (5.8)$$

$$\text{TCO}_{(ksm)} = 436.26008 + 0.02693 \text{ ssn} + 0.08022 \text{ sf} - 714.75563 \text{ mg} \qquad (5.9)$$

$$\text{TCO}_{(msa)} = 406.64225 + 0.01217 \text{ ssn} + 0.09262 \text{ sf} - 595.99994 \text{ mg} \qquad (5.10)$$

The models show that only mg, and therefore, the chromospheric activity, is significant at 99% confidence level at Nairobi and Kisumu and at 95% confidence level at Mombasa. Using the t values to determine the most important variable in predicting TCO in the cities, t- values for mg in the three cities are the highest. Hence, the contribution is not the same for all the SAI variables. The Mg II core to wing ratio has the best input in the variation of TCO at Nairobi, Kisumu and Mombasa.

5.11.3 MLR Performance with the Test Cases

The actual TCO values and those predicted by the MLR models are plotted as line diagrams in Nairobi (Figure 5.21), Kisumu (Figure 5.23) and Mombasa (Figure 5.25) and their scatter plots along with the coefficients of determination, for Nairobi (Figure 5.22), Kisumu (Figure 5.24) and Mombasa (Figure 5.26), respectively, are presented.

The scatter plots indicate positive slopes of the trend lines and reflect a positive association between actual and predicted values. In the line diagram, it is apparent that the predicted did not capture the actual TCO pattern, apart from very few test cases at the beginning. To have a statistical assessment of the prediction, the computed coefficient of determination (R^2) values are 0.1153 (Nairobi), 0.1881 (Kisumu) and (Mombasa) 0.2017.

Figure 5.21 Graphical representation of the actual and estimated TCO for testing procedure at Nairobi using MLR
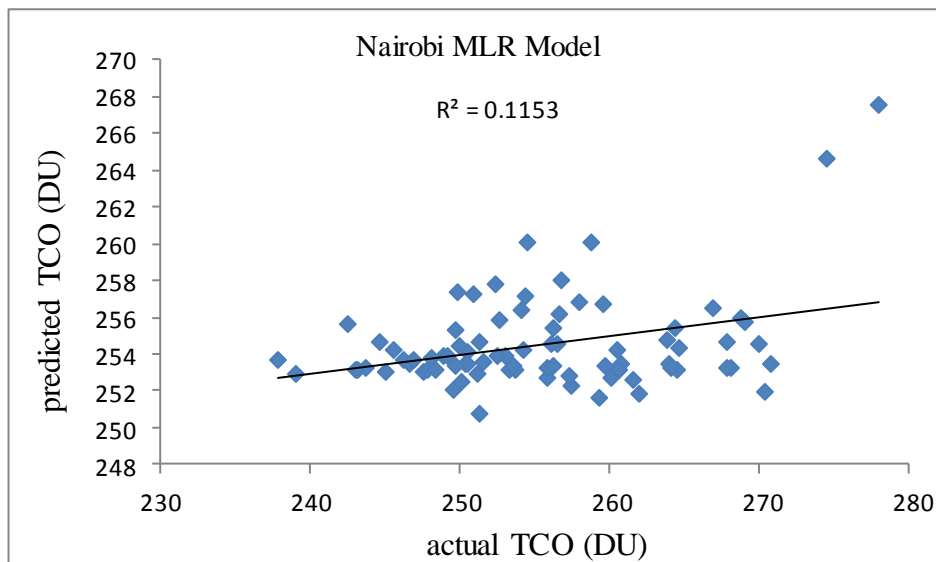
Figure 5.22 A scatter plot representation of the actual and estimated TCO for testing procedure at Nairobi using MLR

124

Figure 5.23 Graphical representation of the actual and estimated TCO for testing procedure at Kisumu using MLR
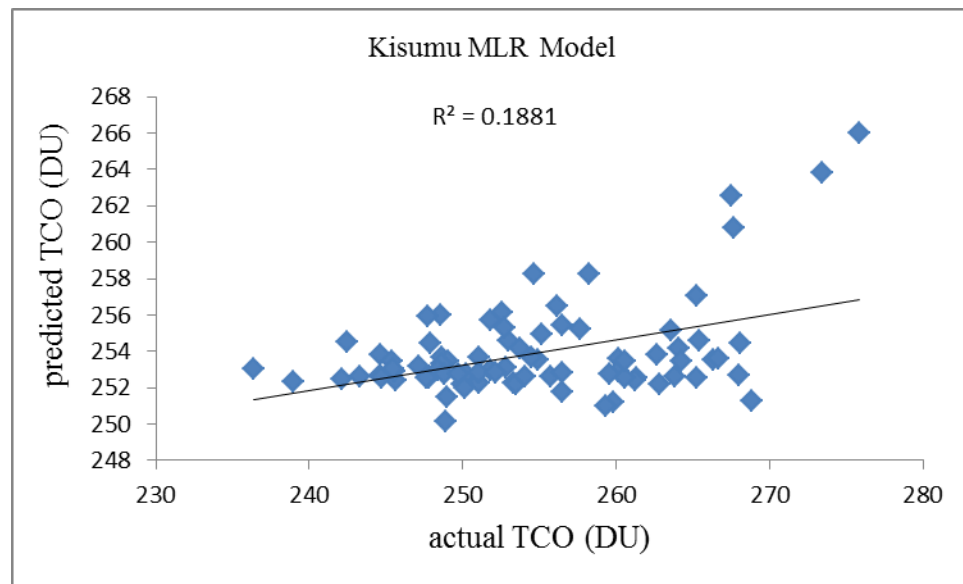
Figure 5.24 A scatter plot representation of the actual and estimated TCO for testing   procedure at Kisumu using MLR
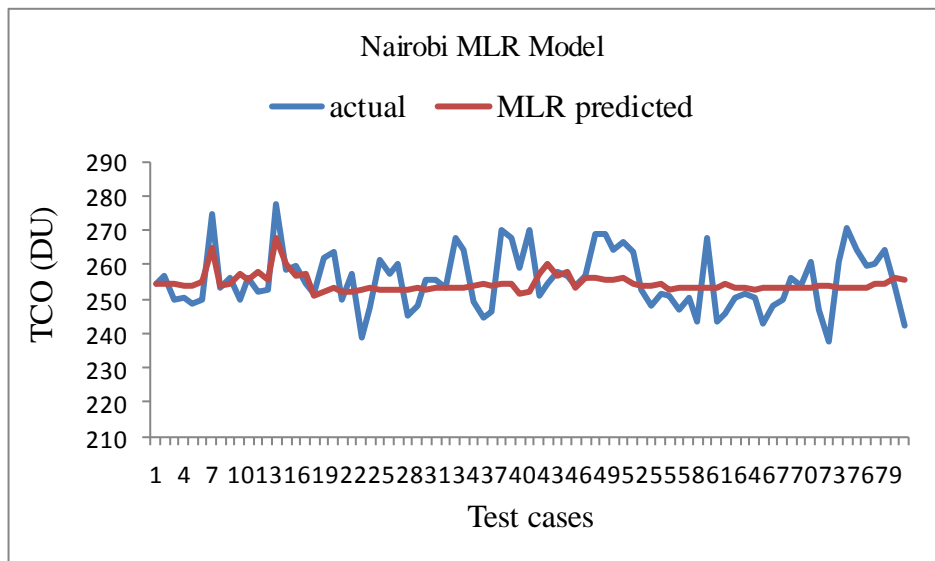
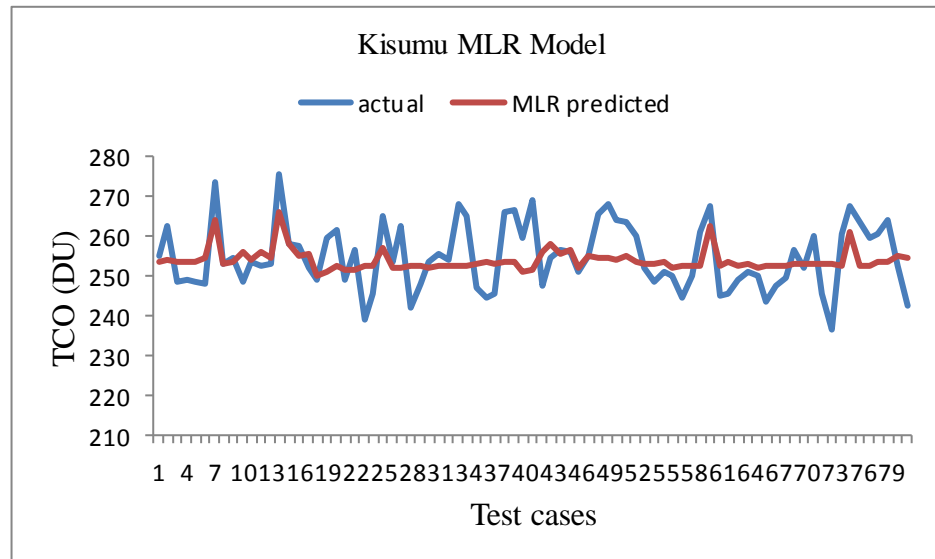**Figure 5.25 Graphical representation of the actual and estimated TCO for testing procedure at Mombasa using MLR**

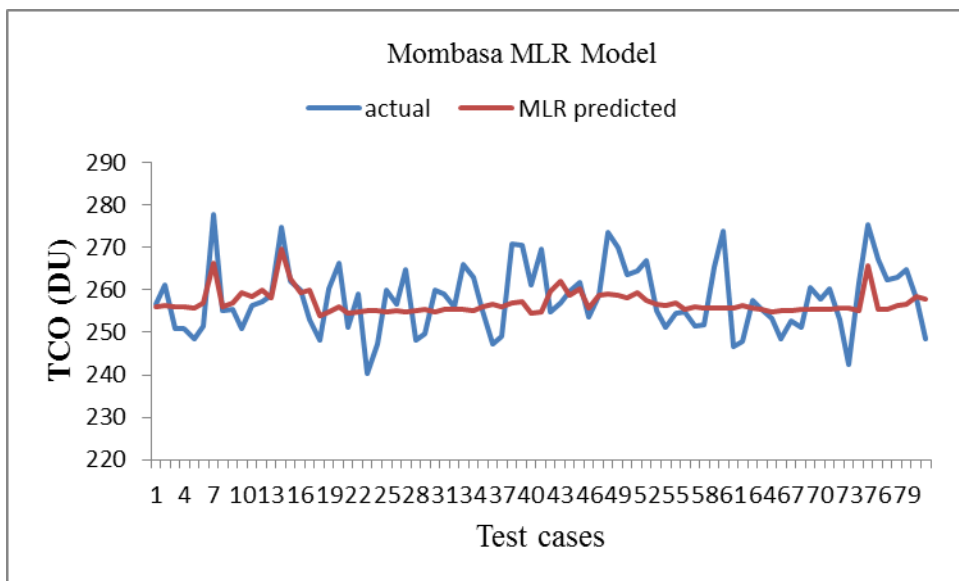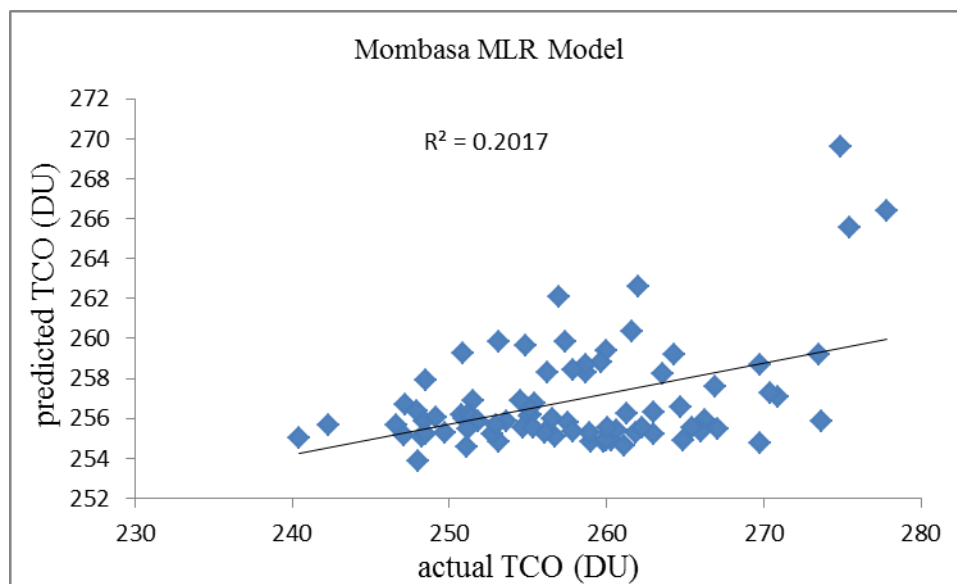**Figure 5.26 A scatter plot representation of the actual and estimated TCO for testing procedure at Mombasa using MLR**

The low proportion of variation in response explained by the MLR model are; 11.53% for Nairobi, 18.81% for Kisumu and 20.17% for Mombasa. The significance of the

models are justified by the t-tests and confirmed by the ANOVA results as the F value (on 3 and 239 DF) is significant in all the three cities since the $p < 0.05$.

Table 5.17 Computed Errors for Mean Monthly TCO for MLR Model for Testing Procedure at (a) Nairobi, (b) Kisumu and (c) Mombasa

TCO	R	RMSE	MAE	R^2	W1	PE%
nrb	0.3396	7.9313	0.9662	0.1153	0.3935	2.713
ksm	0.4337	7.5102	0.8998	0.1881	0.4562	2.428
msa	0.4491	7.1316	0.9681	0.2017	0.5147	2.258

The average RMSE for the residual was found to be 7.9313 (nrb), 7.5102 (ksm) and 7.1316 (msa). The calculated WI and Pearson correlation coefficient, R for all of the three cities are presented in Table 5.17. Figure 5.27 clearly shows that the maximum WI (0.5147) and R (0.4491) are obtained in Mombasa. Next highest values of WI and R are observed for Kisumu and the values are 0.4562 and 0.4337, respectively. The minimum values of WI (0.3935) and R (0.3396) are observed for Nairobi. The Mombasa MLR model presented the highest WI and R values while Nairobi MLR model presented the lowest WI and R values.
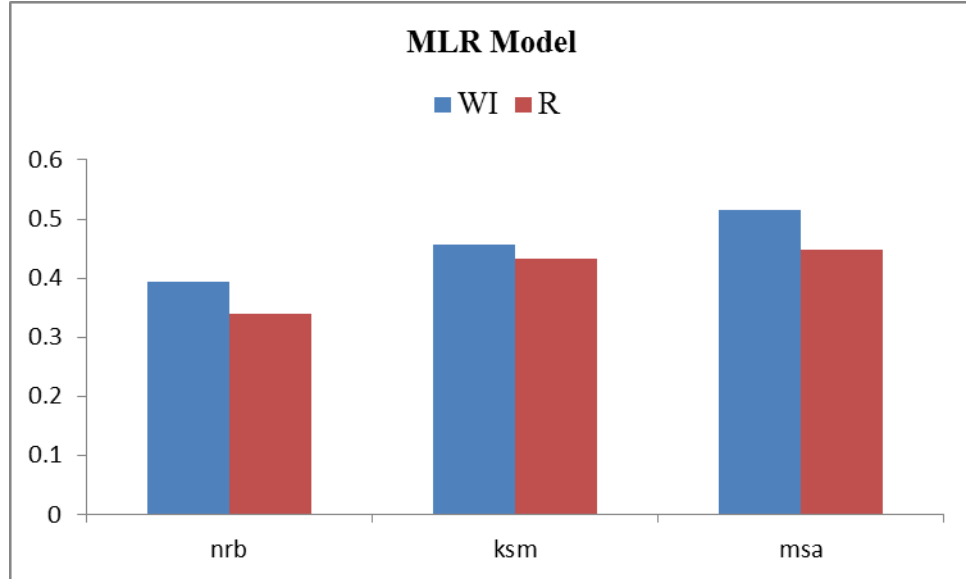
Figure 5.27 The Willmott's index WI and Pearson correlation coefficient for an MLR model generated prediction on the three cities

In Figure 5.28 − 5.30, the performances of the MLR model are pictorially presented; Figure 5.28 (Nairobi) shows that in 71 out of 81 test cases, the percentage prediction error is below 5%. In figure 5.29 (Kisumu), 73 out of 81 test cases are below 5% and in Mombasa (Figure 5.30), 74 out of 81 cases are below 5%.

This means, in 87.65 % (nrb), 90.65% (ksm) and 91.36% (msa) test cases, the absolute prediction error is below 5%. Hence, given ±5% allowance, the prediction yields 0.8765(nrb), 0.9012 (ksm) and 0.9136 (msa). The average percentage prediction errors are given in Table 5.17 as 2.71%, 2.43% and 2.26% for Nairobi, Kisumu and Mombasa respectively.
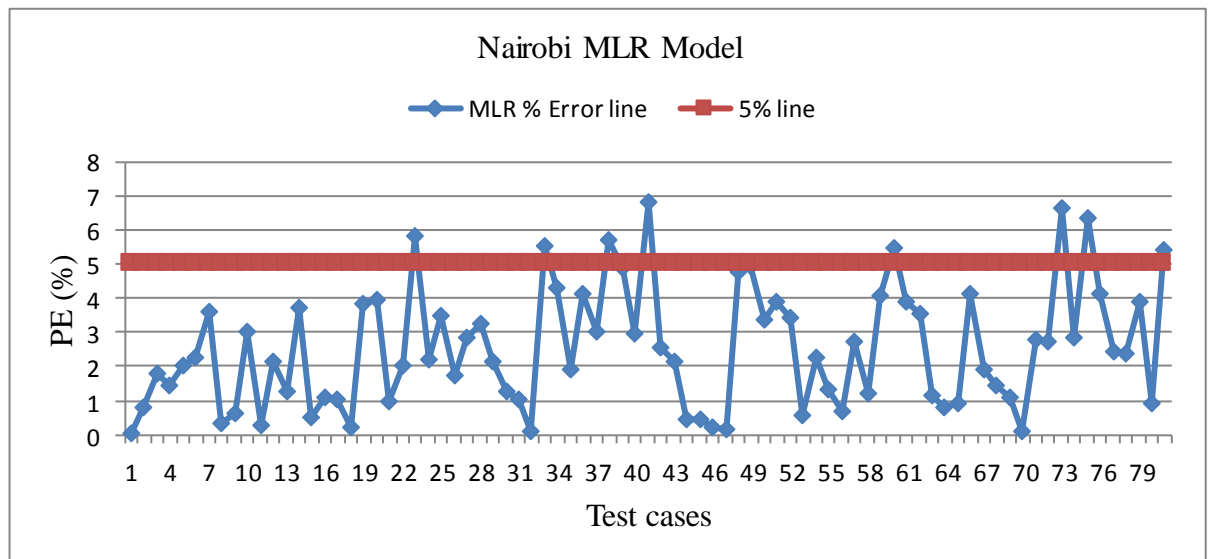
Figure 5.28 Presentation of the absolute prediction errors produced by Nairobi MLR model in the test cases
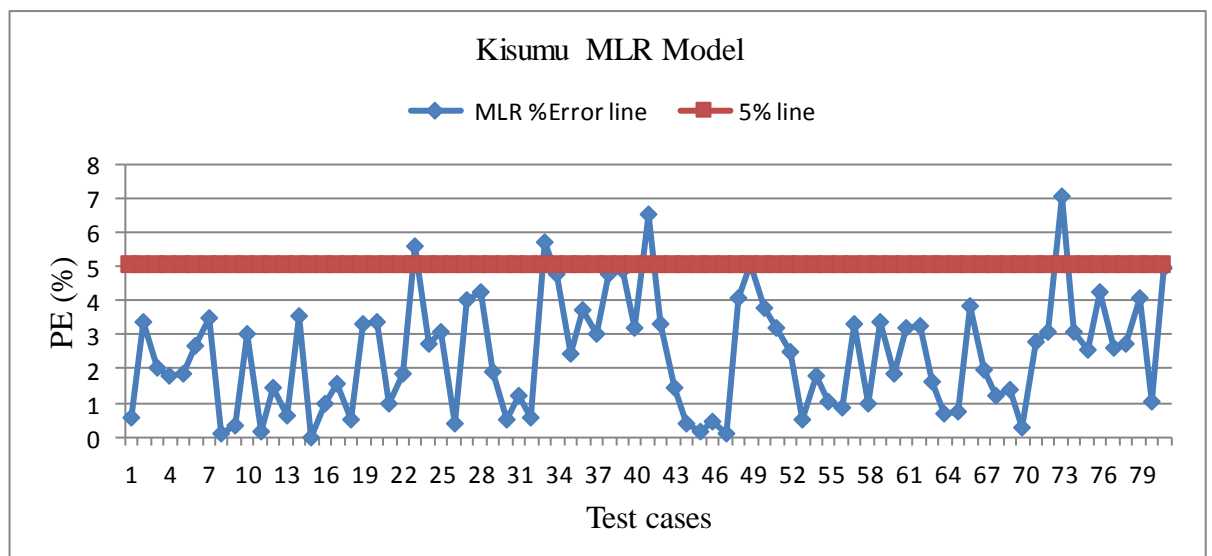
Figure 5.29 Presentation of the absolute prediction errors produced by Kisumu MLR model in the test cases
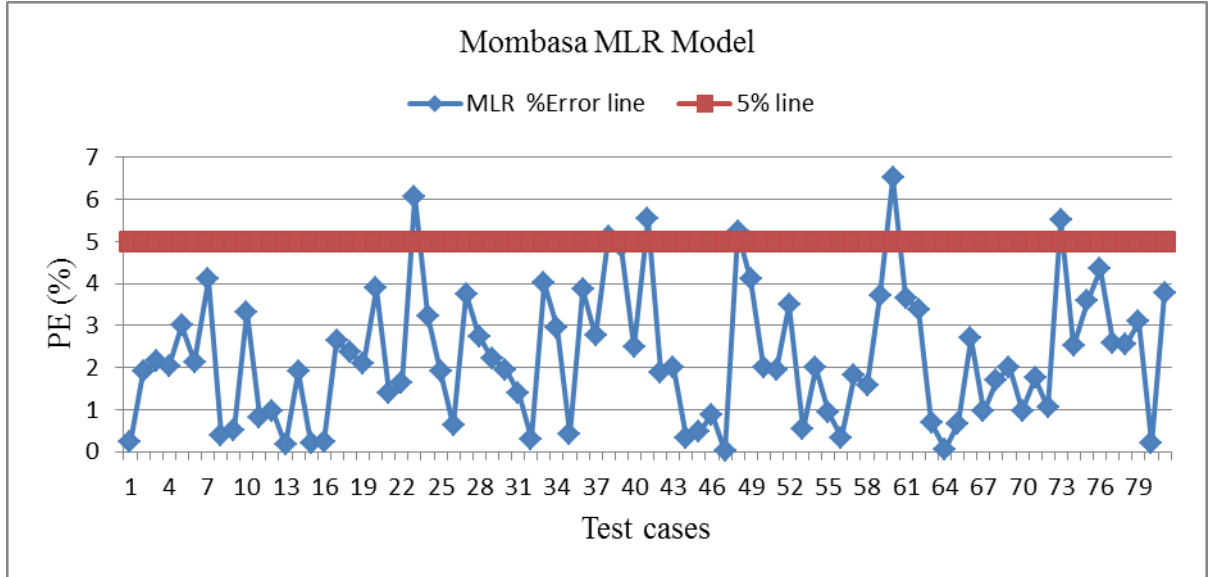
Figure 5.30 Presentation of the absolute prediction errors produced by Mombasa MLR model in the test cases.
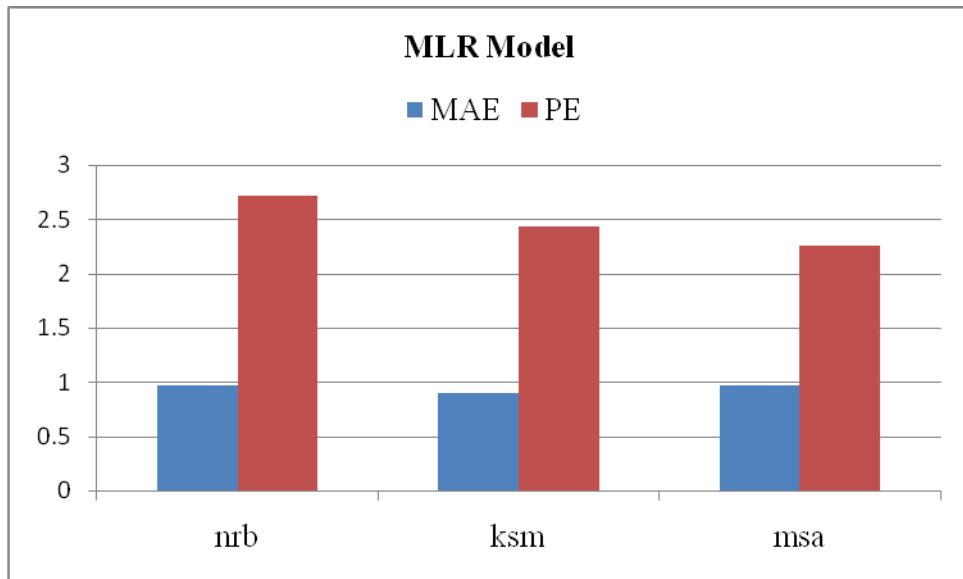
Figure 5.31 The mean absolute error (MAE) and percentage error of prediction (PE) for MLFNN generated prediction over the three cities under study

A bar diagram exhibiting MAE and percentage of PE are presented in Figure 5.30 for the MLR model. Both of the errors attained their maximum for Nairobi and minimum MAE and PE for Kisumu and Mombasa respectively.

5.11.4 MLR Model Prediction Using the Holdout Samples

After the training and testing, the MLR models were validated using the 20 point data hold out sample. Line diagrams; Figure 5.32 (nrb), Figure 5.34 (ksm) and Figure 5.36 (msa) and scatter plots Figure 5.33 (nrb), Figure 5.35 (ksm) and Figure 5.37 (msa) are presented.
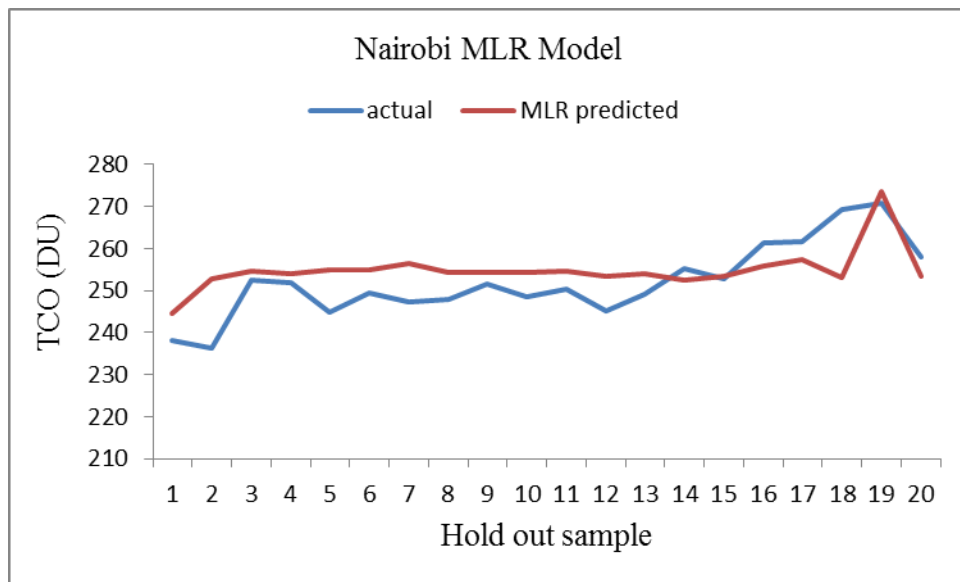
Figure 5.32 Graphical representation of the actual and estimated TCO for predicting procedure at Nairobi using MLR
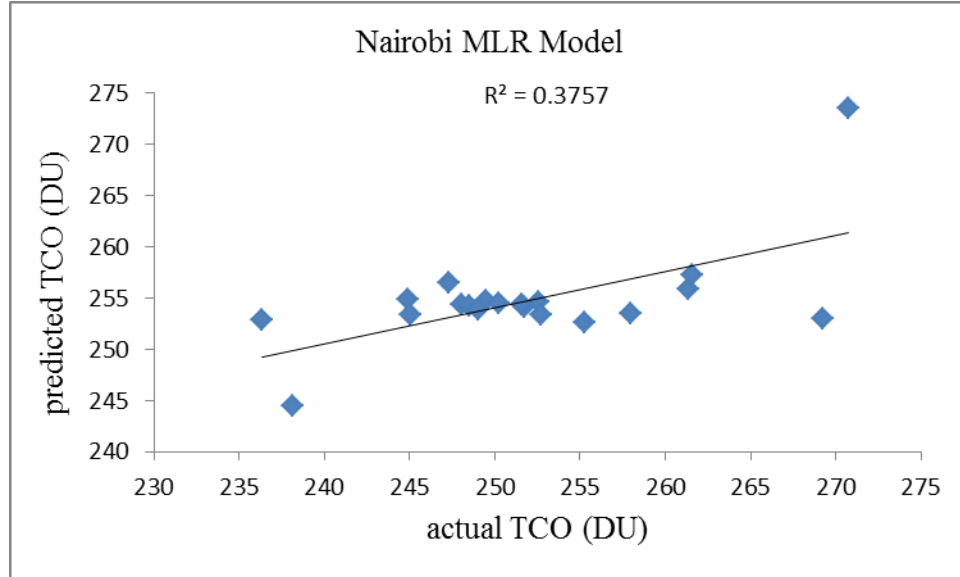
Figure 5.33 A scatter plot representation of the actual and estimated TCO for predicting procedure at Nairobi using MLR
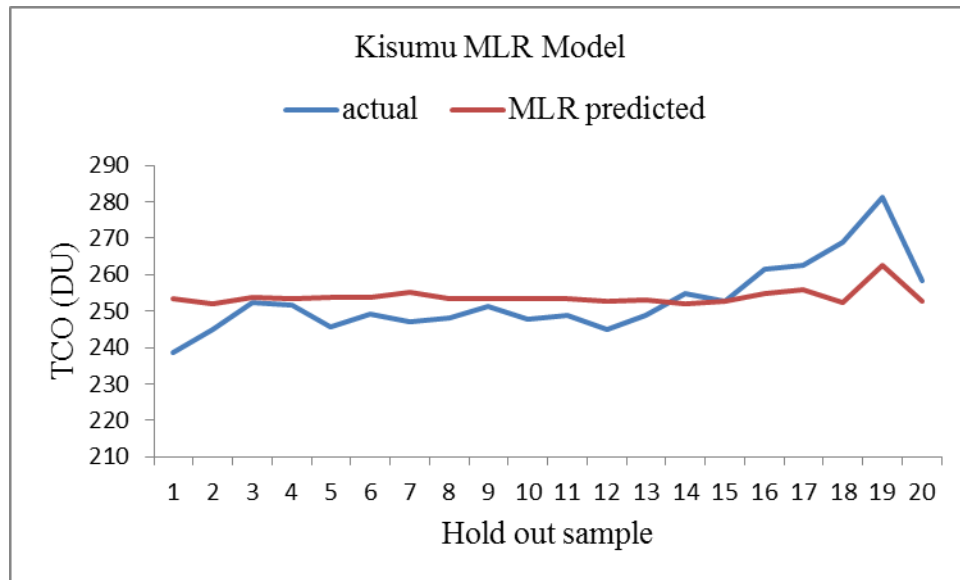
Figure 5.34 Graphical representation of the actual and estimated TCO for predicting procedure at Kisumu using MLR
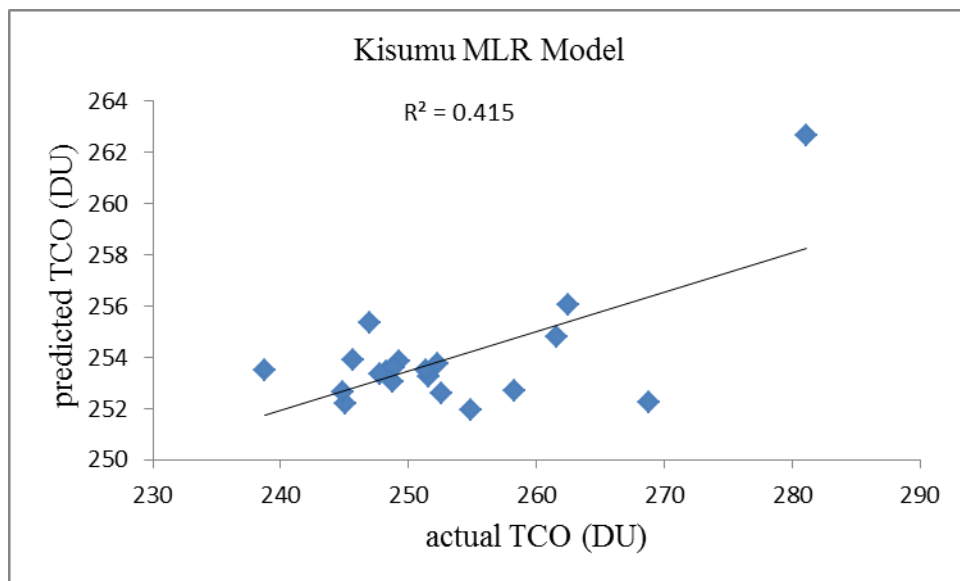
Figure 5.35 A scatter plot representation of the actual and estimated TCO for predicting procedure at Kisumu using MLR
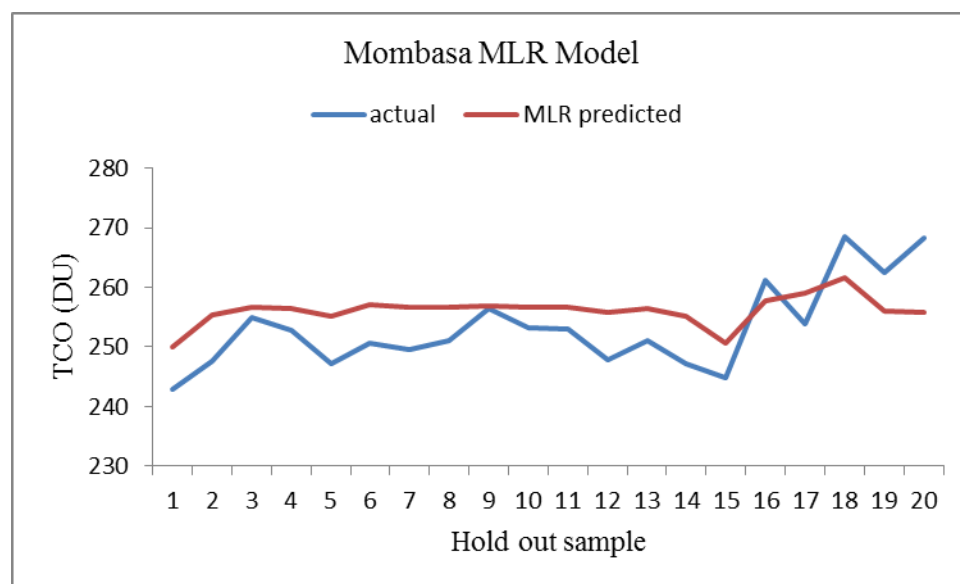
Figure 5.36 Graphical representation of the actual and estimated TCO for predicting procedure at Mombasa using MLR
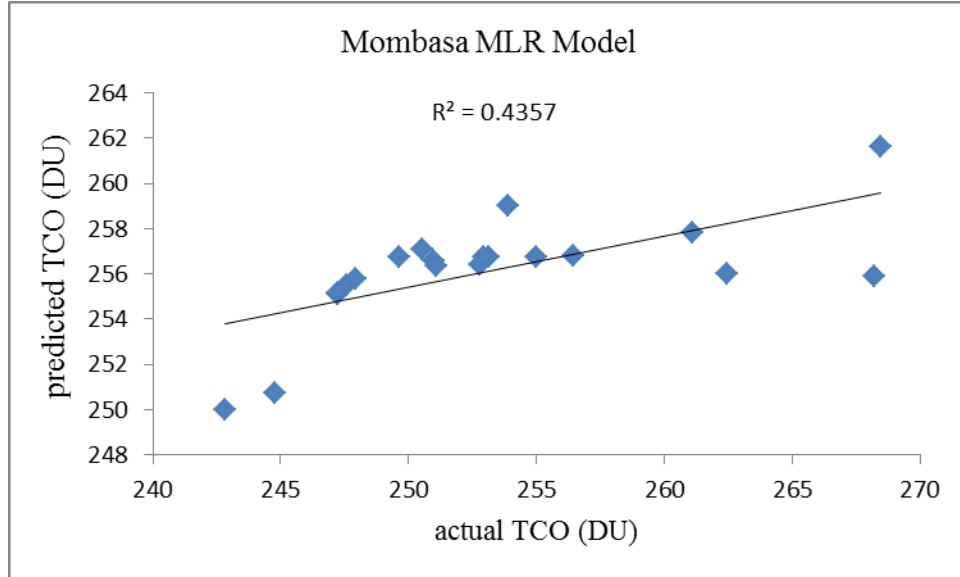
Figure 5.37 A scatter plot representation of the actual and estimated TCO for predicting procedure at Mombasa using MLR

The R^2 are found to be 0.3757 (nrb), 0.4150 (ksm) and 0.2287 (msa) with RMSE values of 7.3177, 8.1765 and 7.1044 for nrb, ksm and msa respectively. These values indicate the proportions of about 37.57 % (Nairobi), 41.50% (Kisumu) and 42.87% (Mombasa) of total variation explained by the results.

5.11.5 MLFNN Model Results

Scale-dependent variables and covariates were rescaled to improve network training by avoiding the asymptotic effect (Chattopadhyay and Chattopadhyay 2009). In the present study, adjusted normalized method was used to rescale the variables. The adjusted transformation had the data converted to real numbers in between 0 and 1.

The backpropogation algorithm with a sigmoid activation function to train the MLFNN with supervised learning method, learning rate η was taken as 0.9 and Momentum taken as 0.7, a feed forward neural network with one input layer, one hidden layer and one output layer was generated. It was noted that the optimum network was 3-15-1. The optimum number of hidden neurons was fifteen in the hidden layer and using the

134

partition given in Table 5.12 for which the error measures, mean squared errors (MSE) are minimum.

There was no easy way to determine the optimum number of hidden units without training and testing. The optimal number of hidden units was found through trial and error. Forward selection method was applied, in which a small number of hidden neurons are selected and the network performance recorded. The training or learning process continued up to step maximum of 1.0×10^6, and number of runs was 10.

Table 5.18 gives the final architectures of the MLFNN models for the respective cities while the schematic diagrams are presented in Figure 5.38 (Nairobi), Figure 5.39 (Kisumu) and Figure 5.40 (Mombasa). All the cities MLFNN model contained 3 neurons in the input layer, one hidden layer with 15 neuron and one neuron in the output layer as the best predictive model. Bandyopadhyay and Chattopadhyay (2007) developed a single layer neural network with 8 hidden nodes as the best predictive model compared to MLR model.

Mombasa MLFNN model presented the lowest RMSE (5.9099) and MAE (0.2232) followed by the Kisumu MLFNN model with MLFNN (6.2858) and MAE (0.2335). Nairobi MLFNN model presented the highest RMSE and MAE values of 6.5494 and 0.4899 respectively.
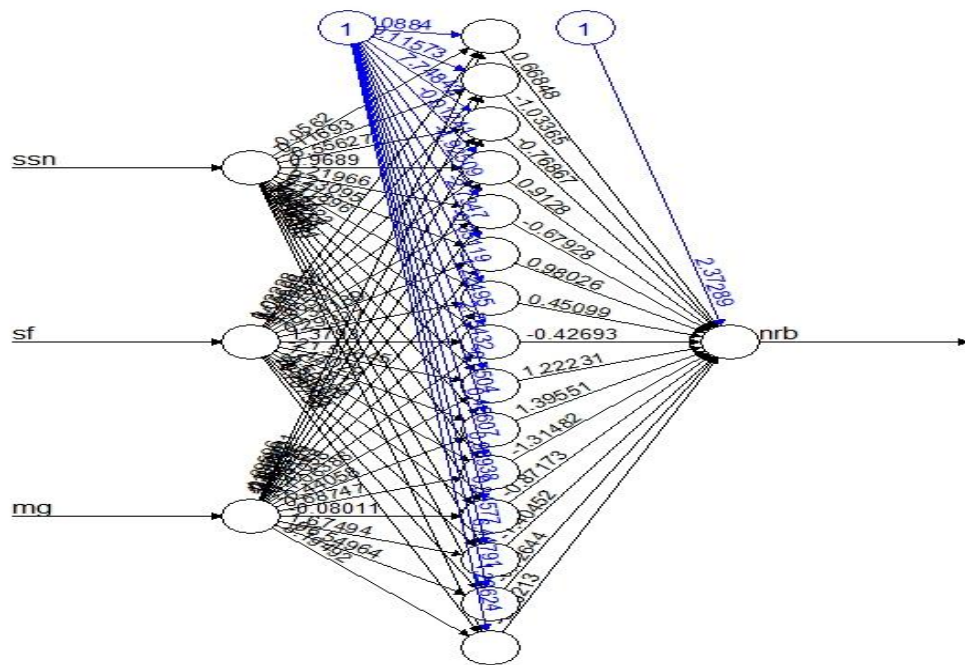
Figure 5.38 A schematic diagram of MLFNN with 3-15-1 for Nairobi
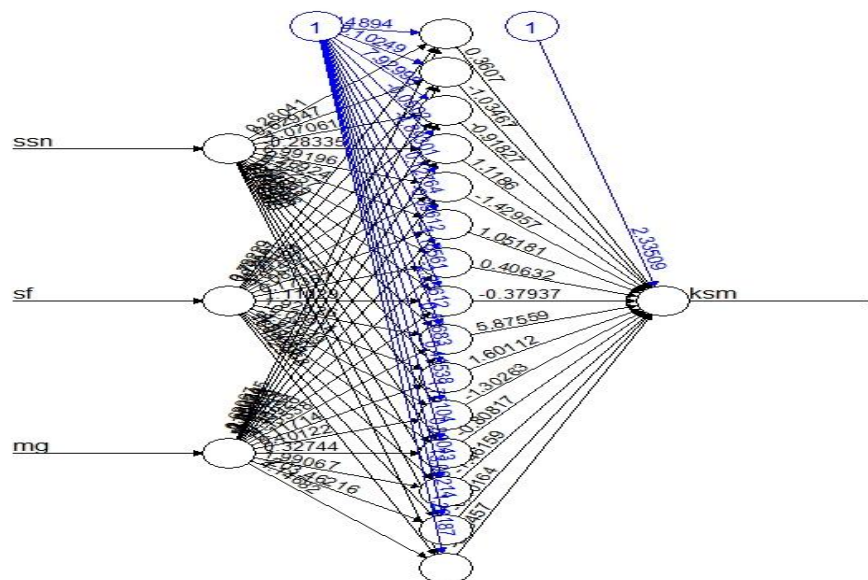
Figure 5.39 A schematic diagram of MLFNN with 3-15-1 for Kisumu
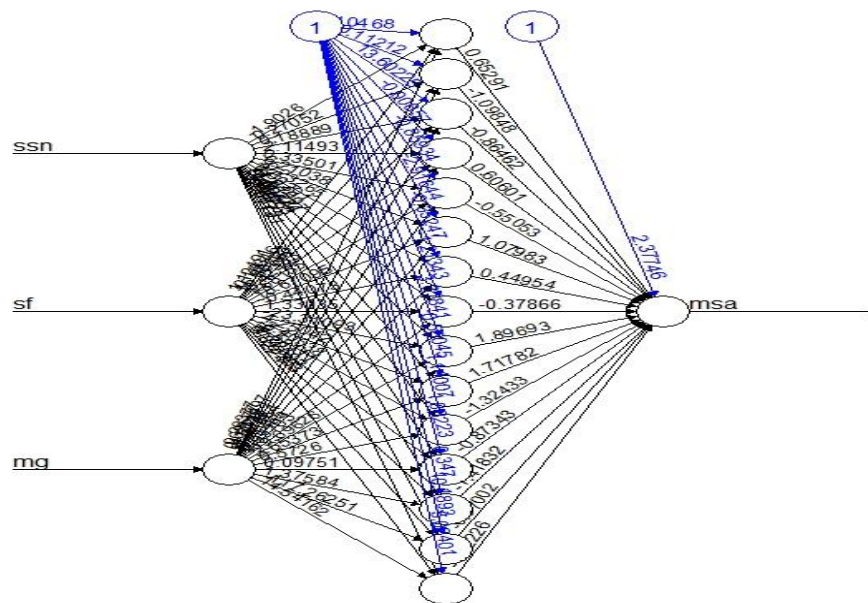
Figure 5.40 A schematic diagram of MLFNN with 3-15-1 for Mombasa

Table 5.18 Developed MLFNN model results

Description	nrb model	ksm model	msa model
Number of training sets	243	243	243
Number of testing sets	81	81	81
Error	4.4943	4.0484	3.7799
Reached threshold	0.008341	0.009990	0.0009799
Steps	6446	6988	17888
Root mean square error	6.5494	6.2858	5.9099
Mean absolute error	0.2899	0.2335	0.2232

5.11.6 MLFNN Performance with the Test Cases

After training the MLFNN, the weight matrix obtained was applied to another independent input to examine the efficiency of the model. This phase is referred to as the testing or validation phase.

In the MLFNN models for Nairobi, Kisumu and Mombasa the line diagrams in (Figure 5.41, Figure 5.43 and Figure 5.45) and scatter plots along with the coefficients of determination (Figure 5.42, Figure 5.44 and Figure 5.46) respectively, are presented.
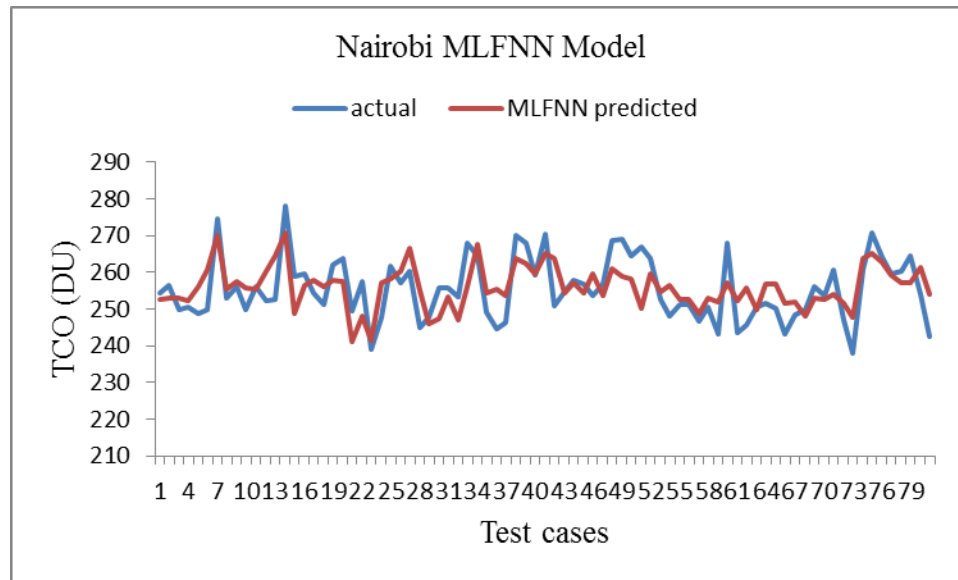
Figure 5.41 Graphical representation of the actual and estimated TCO for testing procedure at Nairobi using MLFNN
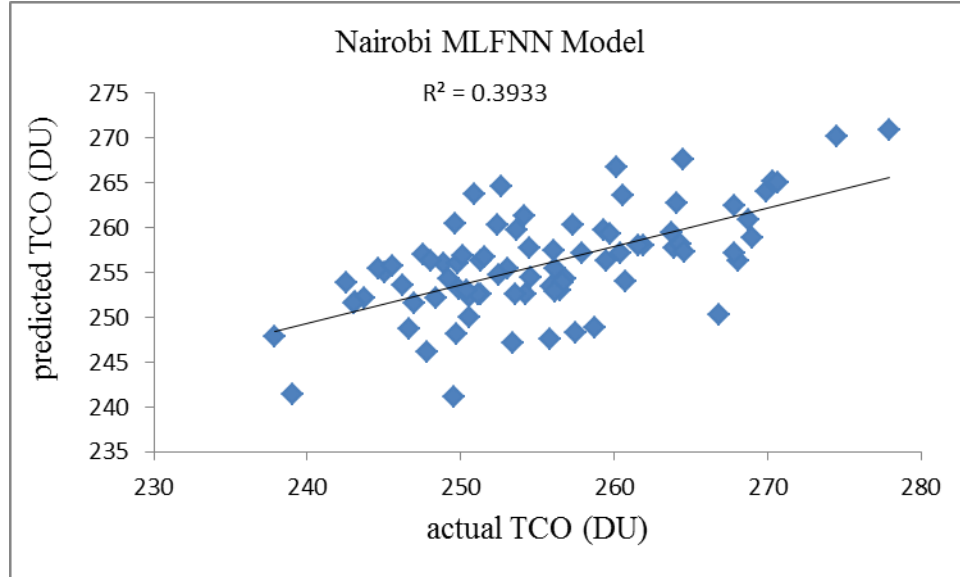
Figure 5.42 A scatter plot representation of the actual and estimated TCO for testing procedure at Nairobi using MLFNN
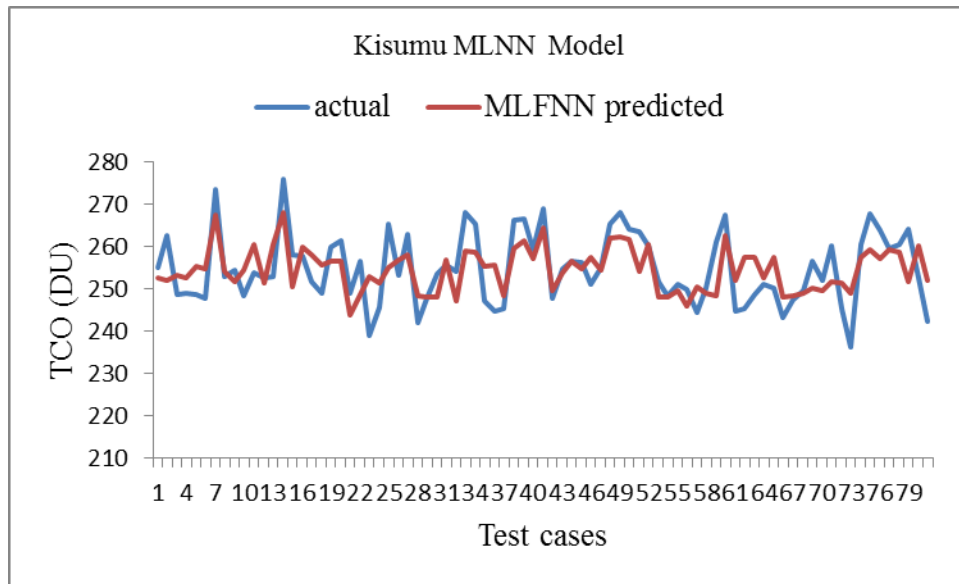
Figure 5.43 Graphical representation of the actual and estimated TCO for testing procedure at Kisumu using MLFNN

Figure 5.44 A scatter plot representation of the actual and estimated TCO for testing procedure at Kisumu using MLFNN

Figure 5.45 Graphical representation of the actual and estimated TCO for testing procedure at Mombasa using MLFNN
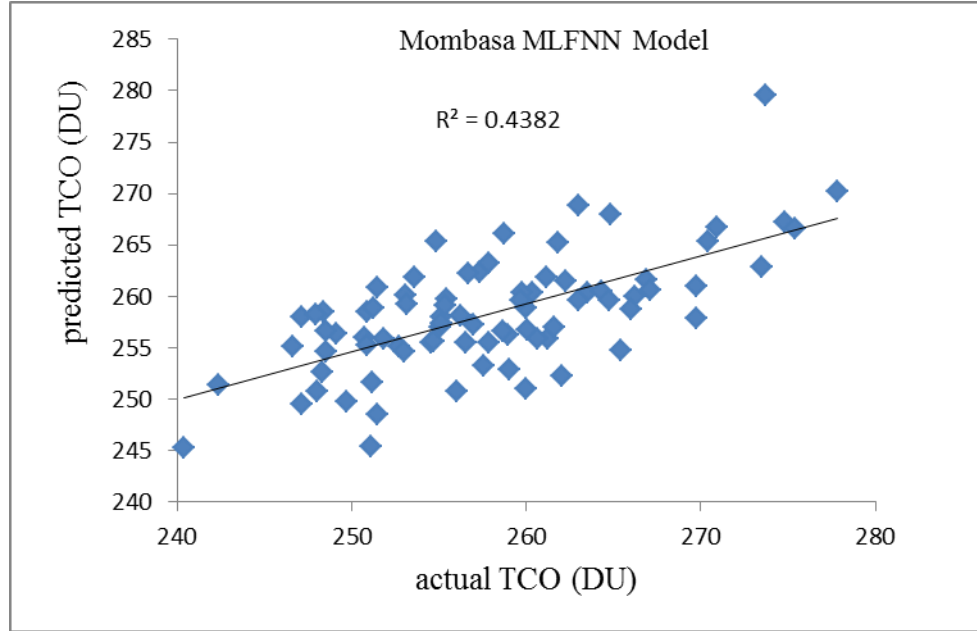
Figure 5.46 A scatter plot representation of the actual and estimated TCO for testing procedure at Mombasa using MLFNN

The scatter plots indicated positive slopes of the trend lines reflecting positive association between actual and predicted values in all the three city models. It is observed that in some of the test cases, in the line diagram, the predicted almost coincides with the actual TCO at a number of test cases. The line diagrams show the nonlinear models, MLFNN, almost captured the pattern of the observed TCO even though they are unable to yield the predictions very close to   TCO values.

Assessing the models statistically, the calculated RMSE for the residual was found to be 6.5494 (nrb), 6.2858 (ksm) and 5.9099 (msa) while the WI and R for all of the three cities are presented in Table 5.19. Figure 5.46 shows that the maximum WI (0.8292) and R (0.6620) are obtained, respectively, in Kisumu and Mombasa. The minimum values of WI (0.7306) and R (0.6271) occur for Mombasa and Nairobi MLFNN models respectively.

Table 5.19 Prediction errors for mean monthly TCO for MLFNN model for testing procedure at (a) Nairobi, (b) Kisumu and (c) Mombasa

TCO	R	RMSE	MAE	R^2	W1	PE (%)
nrb	0.6271	6.5494	0.4899	0.3990	0.7579	2.152
ksm	0.6447	6.2858	0.2335	0.4156	0.8292	1.915
msa	0.6620	5.9099	0.2232	0.4382	0.7306	1.956
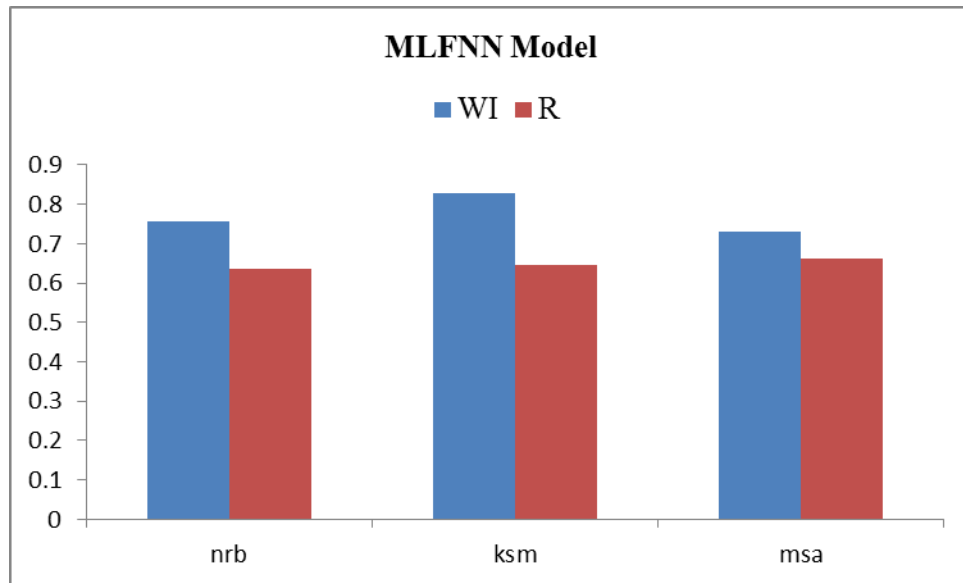
Figure 5.47 The Willmott's index WI and Pearson correlation coefficient for an MLFNN model generated prediction on the three cities

The coefficient of determination, R^2 comes out to be 0.3990 (Nairobi), 0.4156 (Kisumu) and 0.4382 (Mombasa). These values indicate the proportions of about 39.90% (Nairobi), 41.56% (Kisumu) and 43.82% (Mombasa) of total variation are explained by the results.

Percentage predictive performances of the MLFNN models are presented pictorially in Figure 5.48 for Nairobi, Figure 5.49 for Kisumu and Figure 5.50 for Mombasa. It is

observed that; in 79 out of the 81 test cases (2.16 %) for Nairobi , 77 out of 91 cases (2.07 %) for Kisumu; and all of the test cases (100 %) Mombasa, the prediction error is below 5 %. This translates to 2.152 %, 1.915 % and 1.956 % of the absolute prediction error is below 5 % and if ± 5 % is allowed, then the prediction yield is 0.9753 for Nairobi, 0.9506 for Kisumu and 1.00 for Mombasa are significant.

The overall percentage prediction error was 2.16 % for Nairobi model, 2.07 % for Kisumu model and 1.96 % for Mombasa model
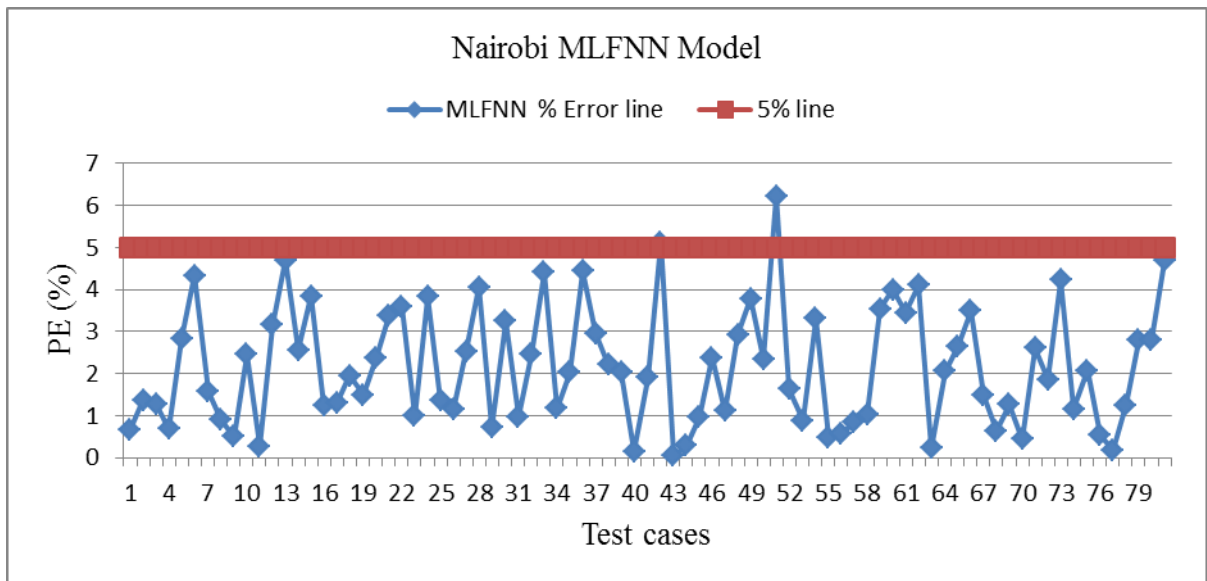
Figure 5.48 Presentation of the absolute prediction errors produced by Nairobi MLFNN model in the test cases
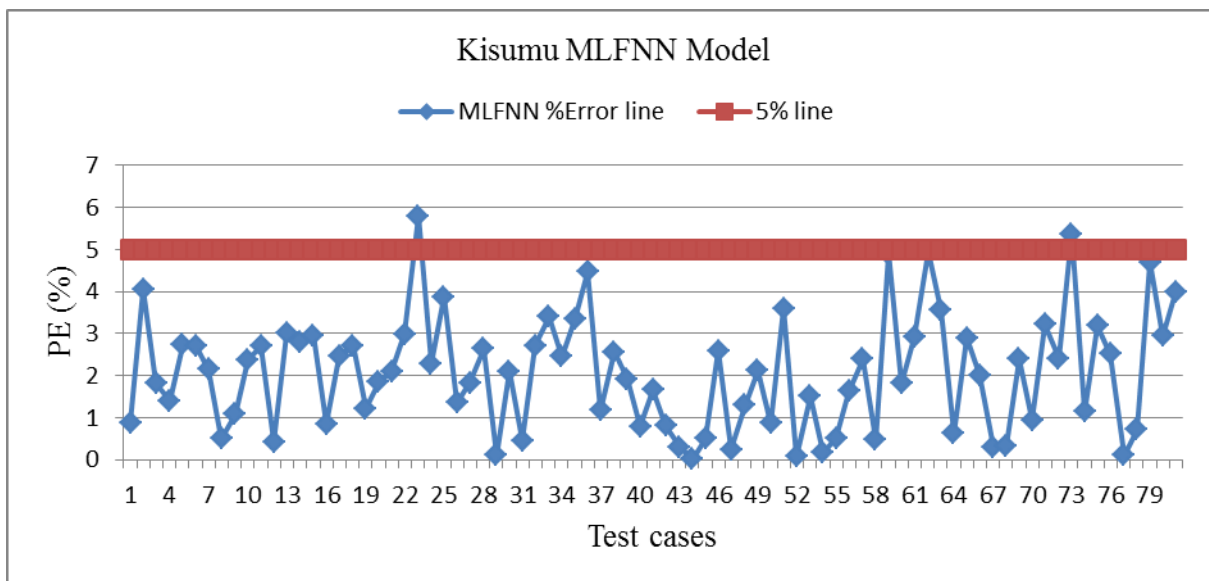
Figure 5.49 Presentation of the absolute prediction errors produced by Kisumu MLFNN model in the test cases
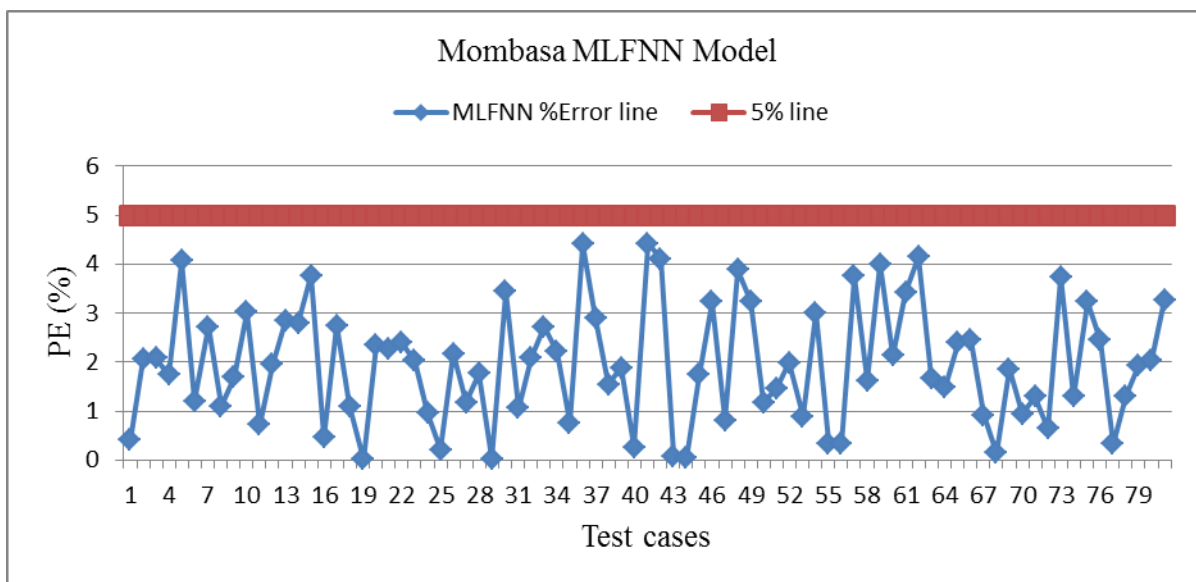
Figure 5.50 Presentation of the absolute prediction errors produced by Mombasa MLFNN model in the test cases
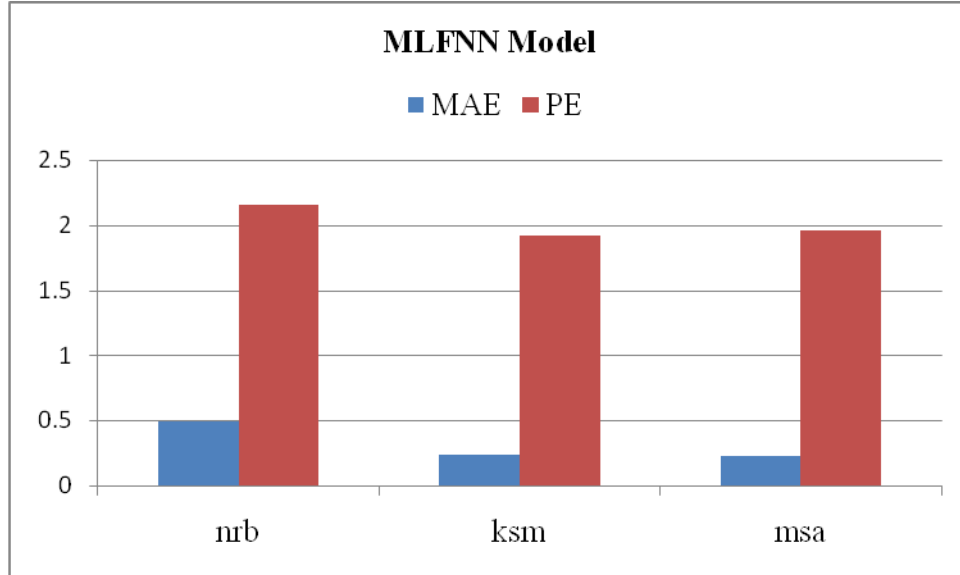
Figure 5.51 The mean absolute error (MAE) and percentage error of prediction (PE) for MLFNN generated prediction over the three cities under study

A bar diagram exhibiting MAE and percentage of PE for the MLFNN models are presented in Figure 5.51. Both of the errors attain their maximum for Nairobi. Minimum MAE and PE are observed in Mombasa and Kisumu models respectively.

5.11.7 MLFNN Model Prediction Using the Holdout Samples

After training and testing, the model was validated over the 20 point dataset set of hold out sample under consideration. For statistical assessment of the hold out samples, the coefficients of determination (R^2), are computed and added to the scatter plots presented in Figure 5.53 (Nairobi), Figure 5.55 (Kisumu) and Figure 5.57 (Mombasa). It is observed that for MLFNN model, the R^2 for Mombasa model (0.5174) is greater than that for Nairobi model (0.4506), which is also the least, while for the Kisumu model, R^2 is 0.4893.
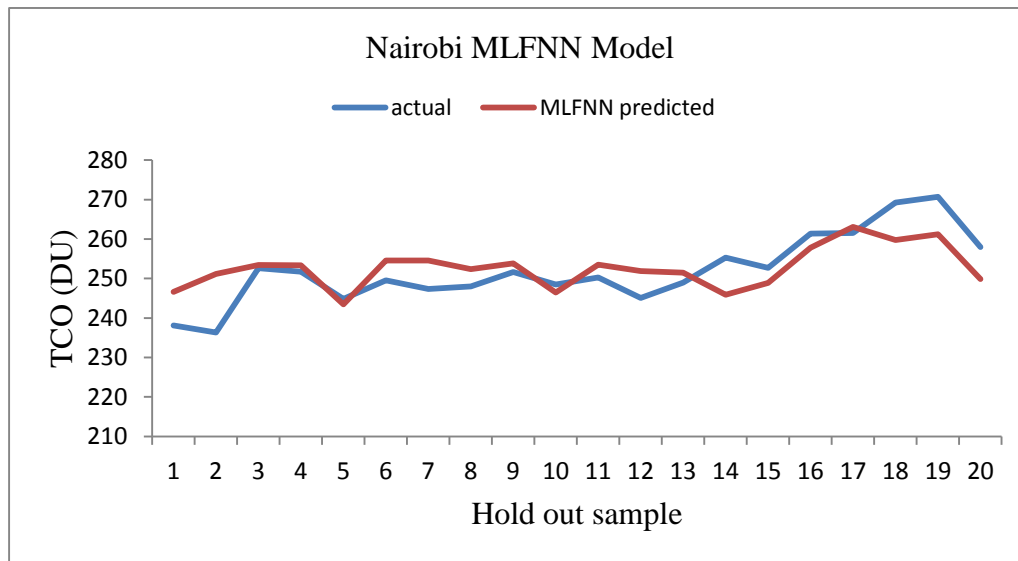
Figure 5.52 Graphical representation of the actual and estimated TCO for predicting procedure at Nairobi using MLFNN
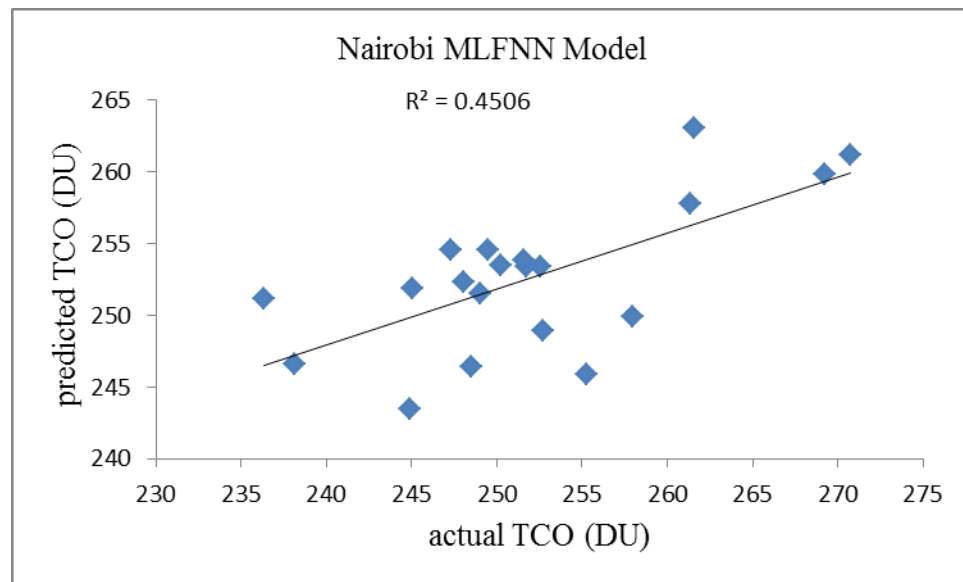
Figure 5.53 A scatter plot representation of the actual and estimated TCO for predicting procedure at Nairobi using MLFNN

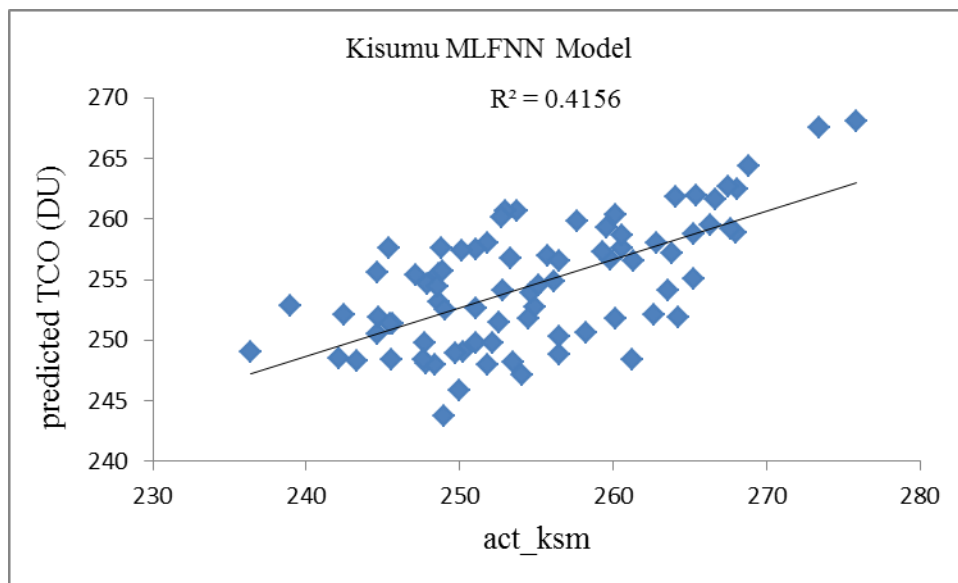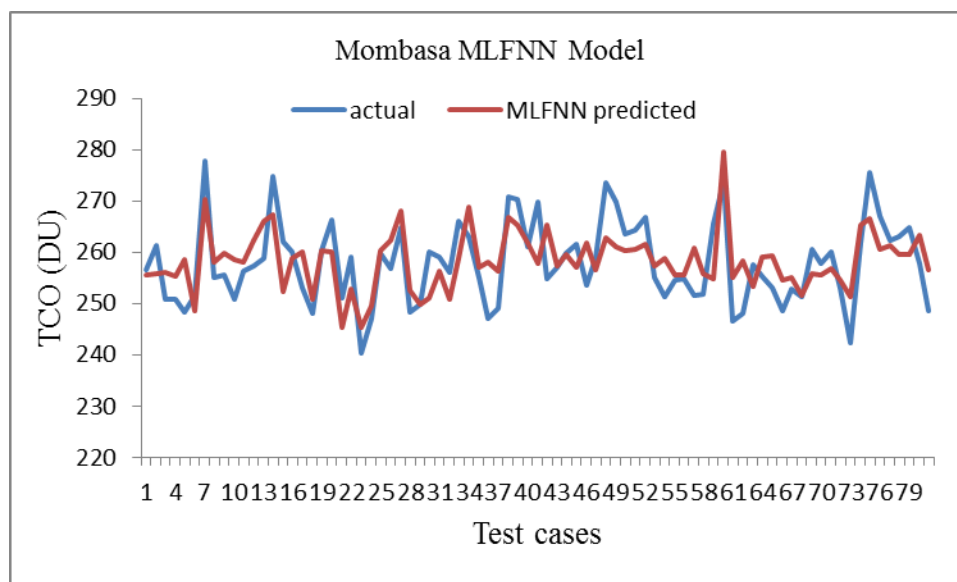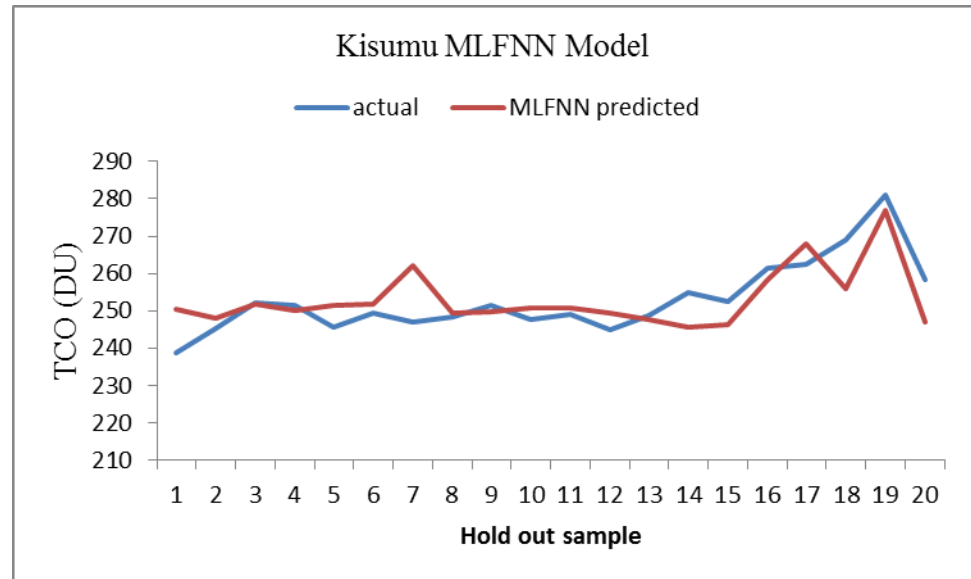**Figure 5.54 Graphical representation of the actual and estimated TCO for predicting at Kisumu using MLFNN**
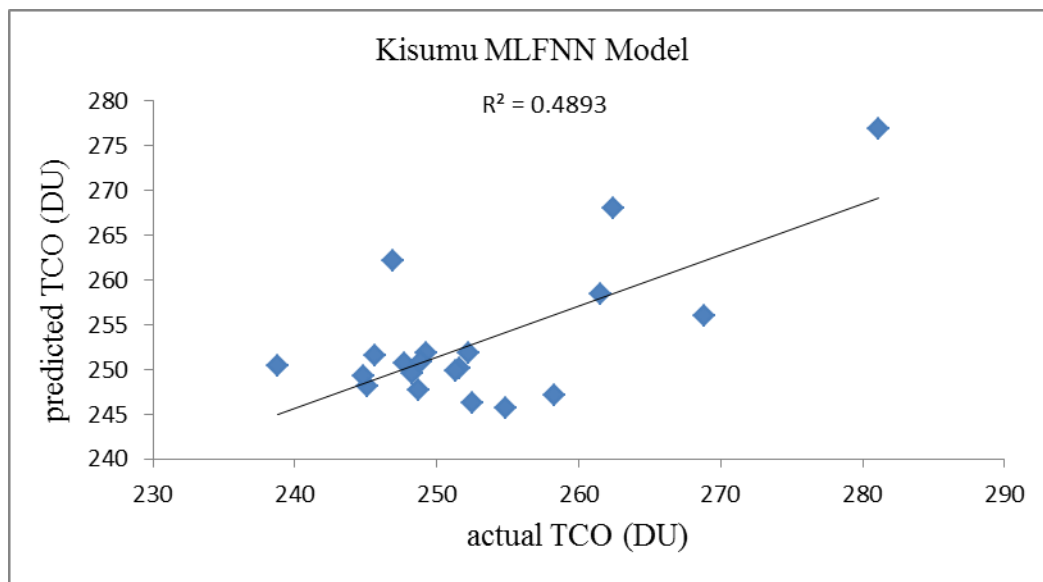
Figure 5.55 A scatter plot representation of the actual and estimated TCO for predicting procedure at Kisumu using MLFNN
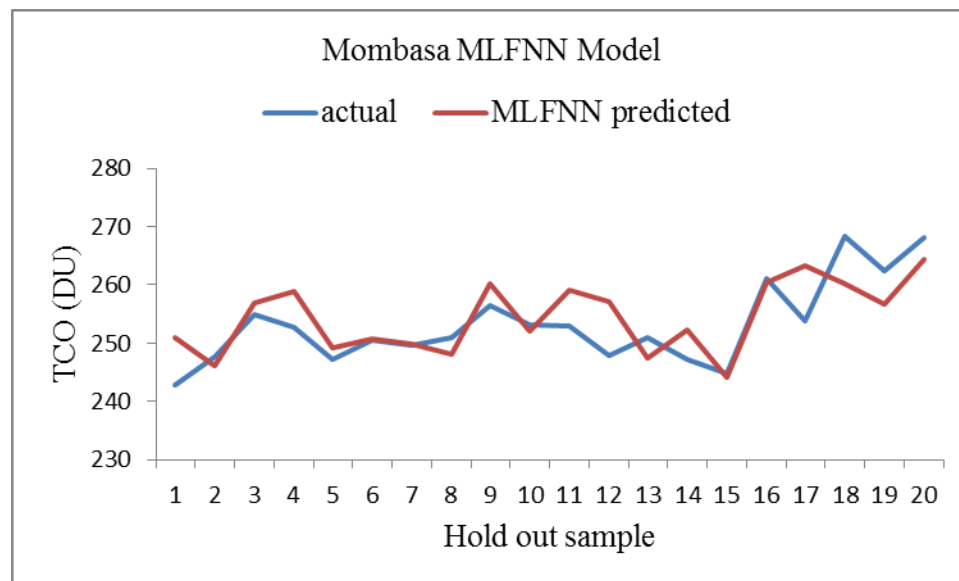
Figure 5.56 Graphical representation of the actual and estimated TCO for predicting procedure at Mombasa using MLFNN
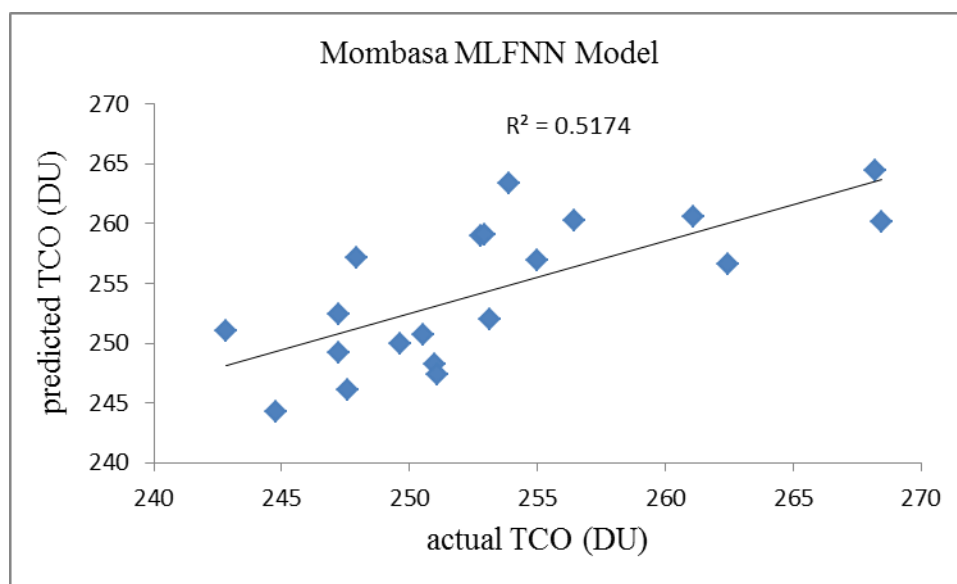
Figure 5.57 A scatter plot representation of the actual and estimated TCO for predicting procedure at Mombasa using MLFNN

5.12 MLR and MLFNN Model Comparison

Performance of the two methods under study, namely MLFNN and MLR in predicting TCO over the three Kenyan cities is measured using R, RMSE, R^2, PE and MAE. To further visualize the prediction performance both line diagrams and scatter plots are compared.

Assessing the models performance Willmott's index (Table 5.20) is close to 1 for the MLFNN model indicating ability to predict mean monthly TCO over the cities. MLFNN model produced higher values of the coefficient of determination (> 0.4) compared to the MLR model (> 0.1) hence the MLFNN explains better the variation in TCO .

To further visualize the performance, it is observed that the scatter plots produced by MLFNN have majority of the points clustered around the linear trend line whereas the MLR model scatter plots, most points are deviated away from the linear trend line. The line diagrams exhibiting the observed predicted TCO almost coincides with the actual TCO at a number of test cases.

Table 5.20 Prediction errors for mean monthly TCO for MLFNN and MLR for testing procedure at (a) Nairobi, (b) Kisumu and (c) Mombasa

	R	RMSE	MAE	R^2	W1	PE (%)
(a) Nairobi						
MLFNN	0.6270	6.5494	0.4899	0.3990	0.7579	2.152
MLR	0.3396	7.9313	0.9662	0.1153	0.3935	2.713
(b) Kisumu						
MLFNN	0.6447	6.2858	0.2335	0.4156	0.8292	1.915
MLR	0.4337	7.5102	0.8998	0.1881	0.4562	2.428
(c) Mombasa						
MLFNN	0.6620	5.9099	0.2232	0.4382	0.7306	1.956
MLR	0.4491	7.1316	0.9681	0.2017	0.5147	2.258

All the MLFNN models presented a lower RMSE, MAE and PE (%) values in all the cities compared to the MLR models as observed in Table 5.20 for the testing cases and Table 5.21 for hold out sample data. Higher values of R, R^2 and WI are observed with the MLFNN models as compared to lower values with the MLR models in both testing and hold out sample data as reported in Table 5.20 and Table 5.21.

Table 5.21 Prediction errors for mean monthly TCO for MLFNN and MLR for holdout sample procedure at (a) Nairobi, (b) Kisumu and (c) Mombasa

	RMSE	R^2
(a) Nairobi		
MLFNN	6.4421	0.4506
MLR	7.3177	0.3757
(b) Kisumu		
MLFNN	6.7957	0.4893
MLR	8.1765	0.4150
(c) Mombasa		
MLFNN	5.0422	0.5174
MLR	7.1044	0.4357
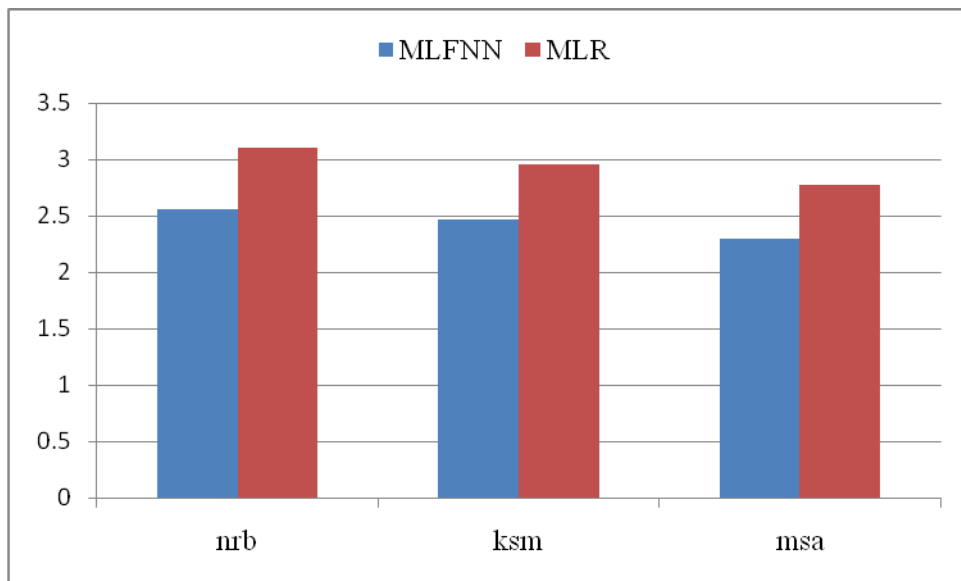
Figure 5.58 RMSE comparison between MLFNN and MLR models in the three Kenyan Cities

The RMSE of the MLFNN and MLR models (Figure 5.58) was found to be 2.56% and 3.10% (Nairobi), 2.47% and 2.95% (Kisumu) and 2.29% and 2.77% (Mombasa) of the mean of observed values respectively.

From Table 5.20 and Table 5.21, the results indicate that MLFNN model outperformed the MLR model. The predictive ability of MLFNN is better and gives better prediction as a result of a result of pattern recognition and generalization made by the network. Similar results were found in previous done studies (Comrie, 1997; Chaloulakou, Grivas & Spyrellis, 2003; Wilks, 2011). MLFNN models produced minimum prediction error when tested against the MLR models applied to the same time series as that of the MLFNN models. On the contrary, the values of RMSE were almost the same among the two models. Although the predictive ability is good, it somehow lacks explanation on the parameters used. Hence some scholars describe ANN as a 'black box'. MLR gives an easy and simple explanation on the estimated parameters. This makes the method to be useful.

MLFNN does not require any underlying assumptions such as linearity, normality etc. MLFNN only requires a good number of data for the network to be able to recognize the pattern formed by the data. MLFNN is also very robust with noise or unexpected data. Another disadvantage of MLFNN is that training time and determination of the optimal number of neurons can take quite some time and can be very complicated and exhaustive.

CHAPTER SIX

CONCLUSIONS AND RECOMMENDATIONS

6.1 Introduction

In this chapter, the conclusions drawn from the results of various methods adopted in this research are stated. Possible future research works in also suggested in the recommendation section.

6.2 Conclusions

6.2.1 Conclusions Drawn from Variability and Trends

The annual and monthly analyses of TCO have shown decreasing trend of TCO with an annual depth of 2.158 DU at Nairobi, 1.759 DU at Kisumu and 2.164 DU at Mombasa during the study period January 1985 − December 2011. A decreasing trend at significant levels of SAI variables is observed showing that, during the study period, SAI was decreasing with highest decrease in ssn (94% of the mean), followed by sf (34%) and least in mg ($\approx$ 2%).

The maximum value of TCO was observed in the SON months of short rain season while the lowest value of TCO was observed in the DJF months of the hot dry season in all the cities. Highest values of TCO were observed in Mombasa and lowest TCO values in Kisumu showing that TCO is a function of latitude. The TCO percentage variability ranged between 1% and 6% (annual) and between 2% and 4% (seasonal) with the highest annual percentage variability observed in the year 2010 at Mombasa (5.76%) while the lowest is observed in 2005 at Kisumu. The highest seasonal variability of 3.91% was observed in June (Nairobi) and lowest variability in the month of October in all the cities

6.2.2 Conclusions Drawn from Statistical Study Analyses.

TCO are highly correlated with each other at ($0.936 < r < 0.955$, $p < 0.001$, 2- tailed). SAI variables are also highly correlated with each other at ($0.941 < r < 0.976$, $p < 0.001$, 2- tailed). Monthly mean SAI variables are significantly positively correlated with

monthly mean TCO over the study period. The highest correlation was found to exist between SAI variables and mean monthly TCO at Mombasa with ssn (0.1974), sf (0.2039) and mg (0.1740).

TCO variations at higher latitudes (Mombasa) are more influenced by the solar activity than at lower latitude (Kisumu). Among the SAI variables, sf and then ssn, seems to have more contribution (input) in ozone production in Nairobi and Mombasa while ssn and then sf, has more input in ozone production in Kisumu. The mean monthly TCO and mean monthly SAI variables showed correlations at both long and short lags. sf has an immediate impact and mg has a delayed impact on TCO while ssn has immediate impact on TCO at Nairobi and Mombasa but a delayed impact at Kisumu. Mg II core to wing ratio has the least contribution to ozone in Nairobi and Mombasa but insignificant in Kisumu. Mg II core to wing ratio is a solar index based on spectral irradiance measurements of the strong Mg II absorption features near 280 nm. Hence at solar maximum ssn and sf are high as well as the UV. But high Mg II core to wing ratio implies high strong Mg II absorption feature near 280nm causing low UV hence low TCO concentrations (Isikwue et al., 2010).

The mean monthly TCO at Nairobi, Kisumu and Mombasa have significant positive correlation (2-tail) with SAI variables. A weak linear relationship exists between the two variables in all the cities. TCO and SAI bore a significant linear relationship at 5% significant level implying that an increase in TCO of about $2 - 3$ % (Nairobi), $1 - 2$% (Kisumu) and $3 - 4$ % (Mombasa) is attributed to solar activity indices.

The contribution is not the same for all the SAI variables. The Mg II core to wing ratio had the most effect on the variation of TCO over Nairobi, Kisumu and Mombasa. All cities indicate positive forcing of the coronal index on TCO. The solar activity in the chromosphere through the mg has negative forcing of TCO in all the cities. The index of the photosphere, the ssn, has positive forcing of TCO at Nairobi and Kisumu and a negative forcing at Mombasa.

154

Spectral analysis revealed three types of periodicities found in TCO over Nairobi, Kisumu and Mombasa. They are 30, 12 and 6 months/cycle. The 12 months period which is a manifestation of the annual effect was more prominent compared to the 6 month period which demonstrates semiannual effect in the atmosphere and the 30 month period which is approximately the QBO periodicity.

6.2.3 Conclusions Drawn from Modeling and Prediction of TCO using SAI Predictors.

The MLR model developed for all the cities showed that the most significant variable in predicting TCO over all the cities was mg, implying that not all solar activity indices have significant contributions in the variation of stratospheric ozone. A fifteen single hidden layer artificial neural network (MLFNN) characterized by sigmoid nonlinearity and an MLR were generated. The training patterns for the models contained three inputs namely: ssn, sf and mg. The output was TCO over the three cities namely; Nairobi, Kisumu and Mombasa.

The MLFNN showed slightly better skills in predicting TCO over the cities than the MLR models. The MLFNN model outmatched the MLR model in capturing better the variability of the data while R was slightly better. A single layered neural layered model (MLFNN) with 15 nodes in the hidden layer and trained with backpropagation learning could be a better alternative to the regression approach in order to predict the average TCO over the cities. The MLR can be used as a simple tool to study the linear relationship between the dependent variable and the independent variables. The method provided two significant explanatory variables to predicting TCO and explains the effect of the contributing factors in a simple and understanding manner.

6.3 Recommendations

1. The general TCO characteristics at the three cities should be compared by using the monthly mean concentration of daily maximum, average and daily minimum for each month. More Kenyan towns, both from the north and south of the equator need to be

analyzed for variability and trend using satellite instruments even when there are no ground based instruments in the respective towns, since TCO is a function of latitude.

2. This study can be extended to examine the use of the artificial neural networks as a method of ozone modeling and for predicting ozone as a function of meteorological conditions and other pollutants. This is because to track and predict ozone, an understanding of not only ozone itself but also the conditions that contribute to its formation is necessary.

3. The results of this study show that the MLFNN (3-15-1) can be a better candidate for predicting TCO compared to MLR. The algorithms used to train ANN in this study are standard backpropagation (BP) which belongs to the gradient descent backpropagation algorithm. Different advanced backpropagation techniques, such as, batch backpropagation (BBP), quick propagation (QP) and Levenberg-Marquardt backpropagation (LM) can also be tried to TCO predict. The details of the algorithms have been reported elsewhere (Ghaffari et al. 2006). Different ANNs can be trained with standard or incremental backpropagation (IBP), batch backpropagation (BBP), quick propagation (QP) and Levenberg-Marquardt backpropagation (LM). A robust comparison of the performances of the above four algorithms can then be made by employing standard statistical indicators.

4. The MLR method is very simple to apply by using available statistical computer software. The future of ANN is promising but further research is needed on the development of computer software that can help reduce the long training time.

5. Develop a relationship between the number of parameters in a model and the optimal number of hidden nodes (neurons) and activation functions in ANN.

REFERENCES

Abdul-Wahab, S. A., & Al-Alawi, S. M. (2002). Assessment and prediction of tropospheric ozone concentration levels using artificial neural networks. *Environmental Modelling & Software*, *17*(3), 219-228.

Agterberg, J. & Brassard, D. (2001). Ozone: The Earth's Sunscreen. Science and Technology Division. p 4.

Ahn, J. B., & Shin, D. W. (1998). Response of total ozone to ENSO in the tropical region. *Korean J. Atmos. Sci*, *1*, 70-77.

Air Resources Board, (ARB) (2002). California Ambient Air Quality Data – 1980 – 2001. Sacramento, CA: ARB

Akinyemi, M. L. (2007). The influence of some atmospheric phenomena on total ozone concentration over the tropics. *Australian Journal of Basic and Applied Sciences, 1*(4), 497-505.

Aksoy, B., Incecik, S., Topcu, S., Demirhan Bari, D., Kahya, C., Acar, Y., ... & Ekici, M. (2009). Total ozone over Ankara and its forecasting using regression models. *International Journal of Remote Sensing*, *30*(17), 4387-4400.

Allen, D. R., & Reck, R. A. (1997). Daily variations in TOMS total ozone data. *Journal of Geophysical Research: Atmospheres*, *102*(D12), 13603-13608.

Anderson, D. R., Sweeney, D. J., & Williams, T. A. (2006). *Essentials of statistics for business and economics*. Thomson South-Western.

Anderson, J. A. (1995). *An introduction to neural networks*. Cambridge, Mass, MIT Press

Anderson, J. G., Toohey, D. W., & Brune, W. H. (1991). Free radicals within the Antarctic vortex: the role of CFCs in Antarctic ozone loss. *Science*, *251*(4989), 39-46.

Andrews, D. G. (2000). *An introduction to atmospheric Physics*. Cambridge, UK: Cambridge University press

Angell, J. K. (1989). On the relation between atmospheric ozone and sunspot number. *Journal of Climate*, *2*(11), 1404-1416.

Arctic Climate Impact Assessment, ACIA (2005) – Chapter 5: *Ozone and ultraviolet radiation*, New York, NY, USA: Cambridge University Press,

Ayoma, W., Gilbert, L., & Bertrand, C. (2004, June). Variability in the observed vertical distribution of ozone over equatorial Eastern Africa: An analysis of Nairobi ozonesonde data 2004. In *Proceedings of the Quadrennial Ozone Symposium* (pp. 1-8).

Bais, A. F., Lubin, D., Arola, A., Bernhard, G., Blumthaler, M., Chubarova, N., ... & Mayer, B. (2007). Surface ultraviolet radiation: Past, present and future, Geneva, Switzerland, Chapter 7 in Scientific Assessment of Ozone Depletion: 2006, Global Ozone Research and Monitoring Project. *World Meteorological Organization*, *58*.

Baldwin, M. P., Gray, L. J., Dunkerton, T. J., Hamilton, K., Haynes, P. H., Randel, W. J., ... & Jones, D. B. A. (2001). The quasi-biennial oscillation. *Reviews of Geophysics*, *39*(2), 179-229.

Bandyopadhyay, G., & Chattopadhyay, S. (2007). Single hidden layer artificial

neural network models versus multiple linear regression model in forecasting the time series of total ozone. *International Journal of Environmental Science & Technology*, *4*(1), 141-149.

Belli, G. (2009). *Nonexperimental quantitative research*. na.

Benestad, R. E. (2006). *Solar activity and earth's climate*. Springer Science & Business Media.

Bhartia, P. K., McPeters, R. D., Mateer, C. L., Flynn, L. E., & Wellemeyer, C. (1996). Algorithm for the estimation of vertical ozone profiles from the backscattered ultraviolet technique. *Journal of Geophysical Research. D. Atmospheres*, *101*, 18793-18806

Bhattacharya, R., Bhoumick, A., & Bhattacharya, A. B. (2012). Satellite and ground based column ozone measurements over three Indian stations. *Nimbus*, *7*, 1978-1993.

Bish, H., Pande B., Chandra, R & Pande, S (2014) Statistical study of different solar activity features with total column ozone at two hill stations of Uttarakhand   Indian *Journal of radio and space physics, 43*,257 - 262

Bodeker, G. E., Hassler, B., Young, P. J., & Portmann, R. W. (2013). A vertically resolved, global, gap-free ozone database for assessing or constraining global climate model simulations. *Earth System Science Data*, *5*(1), 31.

Bodeker, G. E., Nitzbon, J., & Tradowsky J. (2014). A global total column ozone climate data record. Manuscript prepared for Mech. Sci. Discuss. Date: 15 October 2014.

Bojkov, R. D. (1987). The 1983 and 1985 anomalies in ozone distribution in perspective. *Monthly weather review*, *115*(10), 2187-2201.

Bowman, B. R., Tobiska, W. K., Marcos, F. A., Huang, C. Y., Lin, C. S., & Burke, W. J. (2008). A new empirical thermospheric density model JB2008 using new solar and geomagnetic indices, Paper 2008 ,6438. *Am. Inst. of Aeronaut. and Astronaut., New York*.

Brasseur, G. P., & Solomon, S. (2006). *Aeronomy of the middle atmosphere: chemistry and physics of the stratosphere and mesosphere* (Vol. 32). Springer Science & Business Media.

Brasseur, G. (1993). The response of the middle atmosphere to long-term and short-term solar variability: A two-dimensional model. *Journal of Geophysical Research: Atmospheres*, *98*(D12), 23079-23090.

Browning, M. K., Miesch, M. S., Brun, A. S., & Toomre, J. (2006). Dynamo action in the solar convection zone and tachocline: pumping and organization of toroidal fields. *The Astrophysical Journal Letters*, *648*(2), L157.

Bruevich, E. A., & Yakunina, G. V. (2011). Solar Activity Indices in 21, 22 and 23 Cycles. *arXiv preprint arXiv:1102.5502*.

Bruevich, E. A., & Bruevich, V. V. (2013). Correlation study of some solar activity indices in the cycles 21-23. *arXiv preprint arXiv:1304.4545*.

Calisesi, Y., & Matthes, K. (2007). The middle atmospheric ozone response to the 11-year solar cycle. In *Solar Variability and Planetary Climates* (pp. 273-286). New York: Springer

Capone, R. L. (1996). Predicting downwind air quality with a neural network. *Presentation to EPA/Office of Air Quality Planning Standards (OAQPS)*.

Cartalis, C., & Varotsos, C. (1994). Surface ozone in Athens, Greece, at the beginning

and at the end of the twentieth century. *Atmospheric Environment*, *28*(1), 3-8.

Chaloulakou, A., Grivas, G., & Spyrellis, N. (2003). Neural network and multiple regression models for PM10 prediction in Athens: a comparative assessment. *Journal of the Air & Waste Management Association*, *53*(10), 1183-1190.

Chaloulakou, A., Saisana, M., & Spyrellis, N. (2003). Comparative assessment of neural networks and regression models for forecasting summertime ozone in Athens. *Science of the Total Environment*, *313*(1), 1-13.

Chandra, S. (1991). The solar UV related changes in total ozone from a solar rotation to a solar cycle. *Geophysical Research Letters*, *18*(5), 837-840.

Chandrasekhar, S. (1952). XLVI. On the inhibition of convection by a magnetic field. *The London, Edinburgh, and Dublin Philosophical Magazine and Journal of Science*, *43*(340), 501-532.

Chapman, R. D., & Neupert, W. M. (1974). Slowly varying component of extreme ultraviolet solar radiation and its relation to solar radio radiation. *Journal of Geophysical Research*, *79*(28), 4138-4148.

Chapman, S. (1930). A theory of upper atmospheric ozone. *Mem. Roy. Meteorol. Soc.,* *3*,103.

Charbonneau, P. (2010). Dynamo models of the solar cycle. *Living Reviews in Solar Physics*, *7*(1), 1-91.

Chattopadhyay, G., & Chattopadhyay, S. (2008). A probe into the chaotic nature of total ozone time series by correlation dimension method. *Soft Computing-A Fusion of Foundations, Methodologies and Applications*, *12*(10), 1007-1012.

Chattopadhyay, G., & Chattopadhyay, S. (2009). Autoregressive forecast of monthly total ozone concentration: A neurocomputing approach. *Computers & Geosciences*, *35*(9), 1925-1932.

Chattopadhyay, G., & Chattopadhyay, S. (2009). Predicting daily total ozone over Kolkata, India: skill assessment of different neural network models. *Meteorological Applications*, *16*(2), 179-190.

Chattopadhyay, G., & Chattopadhyay, S. (2010). Univariate approach to the monthly total ozone time series over Kolkata, India: autoregressive integrated moving average (ARIMA) and autoregressive neural network (AR-NN) models. *International Journal of Remote Sensing*, *31*(3), 575-583.

Chattopadhyay, G., Chattopadhyay, S., & Jain, R. (2010). Multivariate forecast of winter monsoon rainfall in India using SST anomaly as a predictor: Neurocomputing and statistical approaches. *Comptes Rendus Geoscience*, *342*(10), 755-765.

Chattopadhyay, S. (2007). Feed forward Artificial Neural Network model to predict the average summer-monsoon rainfall in India. *Acta Geophysica*, *55*(3), 369-382.

Chattopadhyay, S., & Chattopadhyay-Bandyopadhyay, G. (2007). Artificial Neural Network versus autoregressive approach: Prediction of total ozone time series. *Model Assisted Statistics and Applications*, *2*(3), 107-120.

Chelani, A. B., Rao, C. C., Phadke, K. M., & Hasan, M. Z. (2002). Prediction of sulphur dioxide concentration using artificial neural networks. *Environmental Modelling & Software*, *17*(2), 159-166.

Choudhuri, A. R. (2007, July). An elementary introduction to solar dynamo theory. In S. S. Hasan, & D. Banerjee (Eds.), *AIP Conference Proceedings* (Vol. 919, No.

1, pp. 49-73). AIP.

Choudhuri, A. R. (1998). *The physics of fluids and plasmas: an introduction for astrophysicists*. Cambridge: Cambridge University Press.

Clette, F., Berghmans, D., Vanlommel, P., Van der Linden, R.A.M. and Koeckelenbergh, A. (2007). Climatological Perspective. *Atmospheric Environment*, *30*(14), 2615-2625.

Clua de Gonzalez, A. L., Silbergleit, V. M., Gonzaleg, W. D.and Tsurutani, B. T.(2001) Annual variation of geomagnetic activities, *Journal of Atmospheric and Solar-Terrestrial Physics 63*,367- 374

Cohen, J., Cohen, P., West, S. G., & Aiken, L. S. (2003). Applied multiple correlation/regression analysis for the behavioral sciences. *UK: Taylor & Francis*.

Comrie, A. C. (1997). Comparing neural networks and regression models for ozone forecasting. *Journal of the Air & Waste Management Association*, *47*(6), 653-663.

Coppola, E. A., Rana, A. J., Poulton, M. M., Szidarovszky, F., & Uhl, V. W. (2005). A neural network model for predicting aquifer water level elevations. *Ground Water*, *43*(2), 231-241.

Covington, A. E. (1948). Solar noise observations on 10.7 centimeters. *Proceedings of the IRE*, *36*(4), 454-457.

Cox, W. M., & Chu, S. H. (1996). Assessment of interannual ozone variation in urban areas from a climatological perspective. *Atmospheric Environment*, *30*(14), 2615-2625.

163

Creswell, J. W. (2009). Qualitative procedures. *Research design: Qualitative, quantitative, and mixed methods approaches*, 173-202.

Crowe, W., & DeFries, T. H. (1996). Use of observation based models to predict ambient ozone levels. *Presentation to EPA/Office of Air Quality Planning Standards (OAQPS)*.

de Wit, T. D., & Watermann, J. (2010). Solar forcing of the terrestrial atmosphere. *Comptes Rendus Geoscience*, *342*(4), 259-272.

Deshler, T., Adriani, A., Gobbi, G. P., Hofmann, D. J., Di Donfrancesco, G., & Johnson, B. J. (1992). Volcanic aerosol and ozone depletion within the Antarctic polar vortex during the austral spring of 1991. *Geophysical research letters*, *19*(18), 1819-1822.

Dessler, A. (2000). *Chemistry and Physics of Stratospheric Ozone* (Vol. 74). Academic press.

Dewitte, S., Crommelynck, D., Mekaoui, S., & Joukoff, A. (2004). Measurement and uncertainty of the long-term total solar irradiance trend. *Solar Physics*, *224*(1), 209-216.

Diab, R. D., Thompson, A. M., Mari, K., Ramsay, L., & Coetzee, G. J. R. (2004). Tropospheric ozone climatology over Irene, South Africa, from 1990 to 1994 and 1998 to 2002. *Journal of Geophysical Research: Atmospheres*, *109*(D20).

Dobson, G. M., & Harrison, D. N. (1926). Measurements of the amount of ozone in The earth's atmosphere and its relation to other geophysical conditions. *Proceedings of the Royal Society of London. Series A, Containing Papers of a Mathematical and Physical Character*, *110*(756), 660-693.

Dobson, G. M. (1966). Annual variation of ozone in Antarctica. *Quarterly Journal of the Royal Meteorological Society*, *92*(394), 549-552.

Donnelly, R. F., Heath, D. F., Lean, J. L., & Rottman, G. J. (1983). Differences in the temporal variations of solar UV flux, 10.7-cm solar radio flux, sunspot number, and Ca-K plage data caused by solar rotation and active region evolution. *Journal of Geophysical Research: Space Physics*, *88*(A12), 9883 9888.

Donnelly, R. F., White, O. R., & Livingston, W. C. (1994). The solar Ca II K index and the Mg II core-to-wing ratio. In *The Sun as a Variable Star: Solar and Stellar Irradiance Variations* (pp. 69-76). Springer Netherlands

Dudok de Wit, T., Kretzschmar, M., Lilensten, J., & Woods, T. (2009). Finding the best proxies for the solar UV irradiance. *Geophysical Research Letters*, *36*(10).

Elkamel, A., Abdul-Wahab, S., Bouhamra, W., & Alper, E. (2001). Measurement and prediction of ozone levels around a heavily industrialized area: a neural network approach. *Advances in environmental research*, *5*(1), 47-59.

Farman, J. C., Gardiner, B. G., & Shanklin, J. D. (1985). Large losses of total ozone in Antarctica reveal seasonal ClOx/NOx interaction.

Fernandez J. H. (2006). An abstract book of UN/NASA workshop on international Heliospherical year (IHY) and borne space science, Bangalore, India

Finlayson-Pitts, B. J., & Pitts Jr, J. N. (1999). *Chemistry of the upper and lower atmosphere: theory, experiments, and applications*. New York: Academic press.

Fligge, M., & Solanki, S. K. (2000). Properties of flux tubes and the relation with solar irradiance variability. *Journal of Astrophysics and Astronomy*, *21*(3-4), 275-282.

Floyd, L., Tobiska, W. K., & Cebula, R. P. (2002). Solar UV irradiance, its variation, and its relevance to the Earth. *Advances in Space Research*, *29*(10), 1427-1440.

Foukal P., (1990). *Solar Astrophysics*. New York: Wiley.

Fröhlich, C., & Lean, J. (2004). Solar radiative output and its variability: evidence and mechanisms. *Astronomy and Astrophysics Review*, *12*(4), 273-320.

Fröhlich, C., & Lean, J. (1998). Total solar irradiance variations: The construction of a composite and its comparison with models. In *Symposium-International Astronomical Union* (Vol. 185, pp. 89-102). Cambridge University Press.

Gardner, M. W., & Dorling, S. R. (1998). Artificial neural networks (the multilayer perceptron)—a review of applications in the atmospheric sciences. *Atmospheric environment*, *32*(14), 2627-2636.

Gardner, M., & Dorling, S. (2001). Artificial neural network-derived trends in daily maximum surface ozone concentrations. *Journal of the Air & Waste Management Association*, *51*(8), 1202-1210.

Gardner, M. W., & Dorling, S. R. (2000). Statistical surface ozone models: an improved methodology to account for non-linear behaviour. *Atmospheric Environment*, *34*(1), 21-34.

Gardner, M. W., & Dorling, S. R. (1999). Neural network modelling and prediction of hourly NOx and NO2 concentrations in urban air in London. *Atmospheric Environment*, *33*(5), 709-719.

Gardner, M.W. (1996). An investigation into the importance of meteorology in determining surface ozone concentrations: a neural network approach. In: First International Conference on GeoComputation. University of Leeds, Leeds School of Geography, GMAP Ltd, Geoinformation International, Elsevier Science pp. 17–19.

Garny, H., Grewe, V., Dameris, M., Bodeker, G. E., & Stenke, A. (2011). Attribution of ozone changes to dynamical and chemical processes in CCMs and CTMs. *Geoscientific Model Development*, *4*(2), 271.

Geller, M. A. (1988). Solar cycles and the atmosphere. *Nature*, *332*(6165), 584-585.

GESDISC, Ozone production and destruction, (April, 2016), (https://disc.gsfc.nasa.gov/ozone/additional/science-focus/aboutozone/ozone_cycle)

Gottman, J. M. (1981). *Time-series analysis: A comprehensive introduction for social scientists* (Vol. 400). Cambridge: Cambridge University Press.

Govindaraju, R. S., & Rao, A. R. (2000). Introduction. In *Artificial Neural Networks in Hydrology* (pp. 1-5). Springer Netherlands.

Gray, L. J., Rumbold, S. T., & Shine, K. P. (2009). Stratospheric temperature and radiative forcing response to 11-year solar cycle changes in irradiance and ozone. *Journal of the Atmospheric Sciences*, *66*(8), 2402-2417.

Gray, L. J. (2010). Stratospheric equatorial dynamics. *Washington DC American Geophysical Union Geophysical Monograph Series*, *190*, 93-107.

Gray, L. J., Beer, J., Geller, M., Haigh, J. D., Lockwood, M., Matthes, K., ... & Luterbacher, J. (2010). Solar influences on climate. *Reviews of Geophysics*,

48(4).

Günther, F., & Fritsch, S. (2010). neuralnet: Training of neural networks. *The R journal*, *2*(1), 30-38.

Haigh, J. D. (2007). The Sun and the Earth's climate. *Living Reviews in Solar Physics*, *4*(1), 1-64.

Haigh, J. D. (1994). The role of stratospheric ozone in modulating the solar radiative forcing of climate. *Nature, 370:544*-546.

Hansen, G., & Svenøe, T. (2005). Multilinear regression analysis of the 65-year Tromsø total ozone series. *Journal of Geophysical Research: Atmospheres*, *110*(D10).

Hathaway, D. H., Nandy, D., Wilson, R. M., & Reichmann, E. J. (2003). Evidence that a deep meridional flow sets the sunspot cycle period. *The Astrophysical Journal*, *589*(1), 665.

Hathaway, D. (2010). The Solar Cycle, Living Rev. *Solar Phys., 7: lrsp-2010-1*.

Hathaway, D. H., & Wilson, R. M. (2004). What the sunspot record tells us about space climate. *Solar Physics*, *224*(1-2), 5-19.

Haynes, P. (2005). Stratospheric dynamics. *Annu. Rev. Fluid Mech.*, *37*, 263-293.

Heath, D. F., & Schlesinger, B. M. (1986). The Mg 280-nm doublet as a monitor of changes in solar ultraviolet irradiance. *Journal of Geophysical Research: Atmospheres*, *91*(D8), 8672-8682.

168

Holgate, S. T., Sandström, T., Frew, A. J., Stenfors, N., Nördenhall, C., Salvi, S., ... & Söderberg, M. (2003). Health effects of acute exposure to air pollution. Part I: Healthy and asthmatic subjects exposed to diesel exhaust. *Research Report (Health Effects Institute)*, (112), 1-30.

Holton, J. R. (2004). *An Introduction to dynamic meteorology* (4th ed.), Elsevier Academic.

Holton, J. R., Haynes, P. H., McIntyre, M. E., Douglass, A. R., Rood, R. B., & Pfister, L. (1995). Stratosphere- troposphere exchange. *Reviews of geophysics*, *33*(4), 403-439.

Hood, L. L., & Zhou, S. (1999). Stratospheric effects of 27- day solar ultraviolet variations: The column ozone response and comparisons of solar cycles 21 and 22. *Journal of Geophysical Research: Atmospheres*, *104*(D21), 26473-26479.

Hood, L. L., & Soukharev, B. E. (2003). Quasi-decadal variability of the tropical lower stratosphere: The role of extratropical wave forcing. *Journal of the atmospheric sciences*, *60*(19), 2389-2403.

Houghton, J. T., Jenkins, G. J., & Ephraums, J. J. (1990). Climate change: The IPCC scientific assessment. *Intergovernmental Panel on Climate Change. Cambridge: CUP*.

Hoyt, D. V., & Schatten, K. H. (1997). *The role of the sun in climate change*. Oxford: Oxford University Press.

IPCC (2001). Climate change 2001: The Scientific Basis – Contribution of Working Group 1 to the Third Assessment Report of IPCC, Cambridge University Press, 944 pp.

Isikwue, B. C., Agada, P. O., & Okeke, F. N. (2010). The contributions of the solar activity indices on the stratospheric ozone variations in Nigeria. *J Emerg Trends Engng Appl Sci (UK)*, *1*(2), 133-139.

Isikwue, B. C., & Okeke, F. N. (2009, April). Effects of Some Atmospheric Parameters on the Dynamics of Lower Stratospheric Ozone in the Low Latitude. In *WOMEN IN PHYSICS: Third IUPAP International Conference on Women in Physics* (Vol. 1119, No. 1, pp. 218-218). AIP Publishing.

Jana, P. K., & Bhattacharyya, S. (2013). Antarctic, Tropical and Equatorial Ozone Depletion and their Correlation with Solar Flux. *International Journal of Innovative Research and Development|| ISSN 2278–0211*, *2*(4), 416-436.

James, I. N. (1994). Introduction to Circulating Atmospheres (Cambridge Atmospheric and Space Science Series; Cambridge.

Jolliffe, I. T. & Stephenson, D. B. (2003). *Forecast Verification. A Practitioner's Guide in Atmospheric Science. West Sussex, England: Wiley*.

Kang, S. M., Polvani, L. M., Fyfe, J. C., & Sigmond, M. (2011). Impact of polar ozone depletion on subtropical precipitation. *Science*, *332*(6032), 951-954.

Kenya meteorological department (2016). Review of rainfall during the "long rains", March to May (MAM) and June-July-August (JJA) seasons.

Kenya Aids Response report, 2014.

Kerr, J. B., & McElroy, C. T. (1993). Evidence for large upward trends of ultraviolet-B radiation linked to ozone depletion. *Science(Washington)*, *262*(5136), 1032-1034.

Kiepenheuer, K. O. (1953). Solar activity. *The Sun*, 322.

Kilcik, A. (2005). Regional sun–climate interaction. *Journal of atmospheric and solar-terrestrial physics*, *67*(16), 1573-1579.

KNBS. (2010). The 2009 Kenya population and housing census. Nairobi: KNBS.

Koskinen, H. (2011). *Physics of Space Storms: From the Solar Surface to the Earth*. Springer Science & Business Media.

Krivova, N. A., Solanki, S. K., Fligge, M., & Unruh, Y. C. (2003). Reconstruction of solar irradiance variations in cycle 23: Is solar surface magnetism the cause?. *Astronomy & Astrophysics*, *399*(1), L1-L4.
.

Kubin, A. (2011). *A model study on the influence of the 11-year solar cycle on the atmosphere* (Doctoral dissertation, Freie Universität Berlin).

Kundt, W. (1992). The 22-year cycle of the sun. *Astrophysics and space science*, *187*(1), 75-85.

Labitzke, K., & Van Loon, H. (1997). Total ozone and the 11-yr sunspot cycle. *Journal of Atmospheric and Solar-Terrestrial Physics*, *59*(1), 9-19.

Lacis, A. A., & Hansen, J. (1974). A parameterization for the absorption of solar radiation in the earth's atmosphere. *Journal of the atmospheric sciences*, *31*(1), 118-133.

Lang, K. (2008). *The sun from space*. Springer Science & Business Media.

Latini, G., Grifoni, R. C., & Passerini, G. (2002). The Importance Of Meteorology In

Determining Surface Ozone Concentrations–A Neural Network Approach. *WIT Transactions on Ecology and the Environment*, *58*.

Layers of Earth's Atmosphere (2016). Retrieved from

http://www.windows2universe.org/earth/Atmosphere/layers_activity_print.html

Lean, J. (1997). The sun's variable radiation and its relevance for earth 1. *Annual Review of Astronomy and Astrophysics*, *35*(1), 33-67.

Lean, J. (1990). A comparison of models of the Sun's extreme ultraviolet irradiance variations. *Journal of Geophysical Research: Space Physics*, *95*(A8), 11933-11944.

Lean, J. L. (2001). Short term, direct indices of solar variability. *Solar Variability and Climate*, 39-51.

Lean, J. (1989). Contribution of ultraviolet irradiance variations to changes in the sun's total irradiance. *Science*, *244*(4901), 197.

Lean, J. (2005). Living with a variable sun. *Physics Today*, *58*(6), 32-38.

Lilensten, J., Wit, T. D. D., Kretzschmar, M., Amblard, P. O., Moussaoui, S., Aboudarham, J., & Auchre, F. (2008, February). Review on the solar spectral variability in the EUV for space weather purposes. In *Annales geophysicae: atmospheres, hydrospheres and space sciences* (Vol. 26, No. 2, p. 269).

Linkages, (1999). 11th MOP to the Montreal Protocol and 5th COP to the Vienna Convention

Loyola, D. G., Coldewey-Egbers, R. M., Dameris, M., Garny, H., Stenke, A., Van Roozendael, M., ... & Koukouli, M. (2009). Global long-term monitoring of the ozone layer–a prerequisite for predictions. *International Journal of Remote Sensing*, *30*(15-16), 4295-4318.

Lockwood, M. (2005). Solar outputs, their variations and their effects on Earth. In *The Sun, solar analogs and the climate* (pp. 109-306). Springer Berlin Heidelberg.

Loyola, D. G., Coldewey-Egbers, R. M., Dameris, M., Garny, H., Stenke, A., Van Roozendael, M., ... & Koukouli, M. (2009). Global long-term monitoring of the ozone layer–a prerequisite for predictions. *International Journal of Remote Sensing*, *30*(15-16), 4295-4318.

Madhu, V., & Gangadharan, K. (2016). Temporal Distribution of Total Column Ozone over Cochin—A Study Based on in Situ Measurements and ECMWF Reanalysis. *Open Journal of Marine Science*, *6*(02), 200.

Madhu, V. (2014). Spatial and Temporal Variability of Total Column Ozone over the Indian Subcontinent: A Study Based on Nimbus-7 TOMS Satellite. *Atmospheric and Climate Sciences*, *4*(05), 884.

Marsh, D. R., Garcia, R. R., Kinnison, D. E., Boville, B. A., Sassi, F., Solomon, S. C., & Matthes, K. (2007). Modeling the whole atmosphere response to solar cycle changes in radiative and geomagnetic forcing. *Journal of Geophysical Research: Atmospheres*, *112*(D23).

McCulloch, W. S., & Pitts, W. (1943). A logical calculus of the ideas immanent in nervous activity. *The bulletin of mathematical biophysics*, *5*(4), 115-133.

McPeters, R. D., Bhartia, P. K., Krueger, A. J., Herman, J. R., Schlesinger, B. M., Wellemeyer, C. G., ... & Torres, O. (1996). Nimbus-7 Total Ozone Mapping Spectrometer (TOMS) data products user's guide.

Mehrotra, K., Mohan, C. K., & Ranka, S. (1997). *Elements of artificial neural networks*.
MIT press.

Midya, S. K., Saha, U., Panda, P., Kundu, A., Chaudhuri, A., & Sarkar, H. (2011). Variation of total ozone concentration and rainfall over different stations of India. *The Pacific J. Sci. Tech.(Spring)*, *12*(1), 580-590.

Miller, A. J., Hollandsworth, S. M., Flynn, L. E., Tiao, G. C., Reinsel, G. C., Bishop, L., ... & Wuebbles, D. (1996). Comparisons of observed ozone trends and solar effects in the stratosphere through examination of ground- based Umkehr and combined solar backscattered ultraviolet (SBUV) and SBUV 2 satellite data. *Journal of Geophysical Research: Atmospheres*, *101*(D4), 9017-9021.

Molina, M. J., & Rowland, F. S. (1974). Stratospheric sink for chlorofluoromethanes: chlorine atom-catalysed destruction of ozone. *Nature*, *249*(28), 810-812.

Msiza, I. S., Nelwamondo, F. V., & Marwala, T. (2008). Water demand prediction using artificial neural networks and support vector regression.

Muthama, N. J. (1989). *Total atmospheric ozone characteristics over a tropical region* (Doctoral dissertation, MSc thesis. Department of Meteorology, University of Nairobi, Kenya).

Nag, T. K., & Das, T. K. (2007). Periodicity in various kinds of solar activity. *Institute*

of Radio Physics & Electronics, Kolkata-700009. Email: tukada2@ vsnl. net.

Naja, M., & Lal, S. (1997). Solar eclipse induced changes in surface ozone at Ahmedabad.

Ndeda, J. O. H., Rabiu, A. B., Ngoo, L. H. M., & Ouma, G. O. (2011). Estimation of climatic parameters from solar indices using ground based data from Kenya, East Africa. *Journal of Science and Technology (Ghana)*, *31*(1).

Ndeda, J. O. H. (2013). *Solar Radiative Variability Forcing of Climate Change on Seasonal to Decadal Scales in Kenya* (Doctoral dissertation).

Newman, P. A. (2004). *Stratospheric ozone*. Retrieved from http://www.ccpo.odu.edu/SEES/ozone/class/chapter_1/index.htm.

NGDC (2013). Retrieved from http://www.ngdc.noaa.gov/stp/space-weather/solar-data/solar-indices/sunspot-numbers/international/listings/listing_international-sunspot-numbers_daily.txt

NGDC (2013). Retrieved from **ftp**://ftp.ngdc.noaa.gov/STP/space-weather/solar-data/solar- features/solar-radio/noontime-flux/penticton/penticton_observed/ flux-observed_daily.txt

NGDC (2013). Retrieved from ftp://ftp.ngdc.noaa.gov/STP/SOLAR_DATA/SOLAR_UV/NOAAMgII.dat

Nicolet, M., & Bossy, L. (1985). Solar radio fluxes as indices of solar activity. *Planetary and space science*, *33*(5), 507-555.

Nunnari, G., Nucifora, A. F. M., & Randieri, C. (1998). The application of neural

techniques to the modelling of time-series of atmospheric pollution data. *Ecological Modelling*, *111*(2), 187-205.

Obiekezie, T. N. (2009). Sunshine activity and total column ozone variation in Lagos, Nigeria. *Moldavian Journal of the Physical Sciences*, *8*(2), 169-172.

Ongoma, V., Muthama, N. J., & Gitau, W. (2013). Evaluation of urbanization influences on urban winds of Kenyan cities. *Ethiopian Journal of Environmental Studies and Management*, *6*(3), 223-231.

Östermark, R. (1999). A Neuro-Genetic Algorithm for Heteroskedastic Time-Series Processes Empirical Tests on Global Asset Returns. *Soft Computing-A Fusion of Foundations, Methodologies and Applications*, *3*(4), 206-220.

Oyekola, O. S. (2011). Climatology of equatorial stratospheric ozone and trends over Lagos (6.6 N, 3.3 E). *Ozone: Science & Engineering*, *33*(6), 489-500.

Ozone layer protection (2016). Retrieved from http://www.epa.gov/ozone

Parker, E. N. (1979). Cosmical magnetic fields: Their origin and their activity. *New York: Oxford University Press,*

Parker, E. N. (1955). Hydromagnetic Dynamo Models. *The Astrophysical Journal*, *122*, 293.

Pérez, P., Trier, A., & Reyes, J. (2000). Prediction of PM 2.5 concentrations several hours in advance using neural networks in Santiago, Chile. *Atmospheric Environment*, *34*(8), 1189-1196.

Pienitz, R., & Vincent, W. F. (2000). Effect of climate change relative to ozone depletion on UV exposure in subarctic lakes. *Nature*, *404*(6777), 484-487.

Pires, J. C. M., & Martins, F. G. (2011). Correction methods for statistical models in tropospheric ozone forecasting. *Atmospheric Environment*, *45*(14), 2413-2417.

Plumb, R. A. (2002). Stratospheric transport. *Journal of the Meteorological Society of Japan. Ser. II*, *80*(4B), 793-809.

Priest, E. R. (1982). Solar Magnetohydrodynamics (Reidel, Dordrecht, 1982). *Google Scholar*, 465.

Rabiu, A. B. (2013). Solar activity and total column ozone variation in Lagos, Nigeria. *Nigeria Journal of pure and applied physics*, *2*(1), 17-20.

Randall, C. E., Harvey, V. L., Singleton, C. S., Bailey, S. M., Bernath, P. F., Codrescu, M., ... & Russell, J. M. (2007). Energetic particle precipitation effects on the Southern Hemisphere stratosphere in 1992–2005. *Journal of Geophysical Research: Atmospheres*, *112*(D8).

Reed, R. J., Campbell, W. J., Rasmussen, L. A., & Rogers, D. G. (1961). Evidence of a downward- propagating, annual wind reversal in the equatorial stratosphere. *Journal of Geophysical Research*, *66*(3), 813-818.

Reid, G. C. (1994). Seasonal and interannual temperature variations in the tropical stratosphere. *Journal of Geophysical Research: Atmospheres*, *99*(D9), 18923-18932.

Riley, P., & Crooker, N. U. (2004). Kinematic treatment of coronal mass ejection evolution in the solar wind. *The Astrophysical Journal*, *600*(2), 1035.

Rind, D., Shindell, D., Perlwitz, J., Lerner, J., Lonergan, P., Lean, J., & McLinden, C. (2004). The relative importance of solar and anthropogenic forcing of climate change between the Maunder Minimum and the present. *Journal of Climate*, *17*(5), 906-929.

Rojas, R. (1996). Neural Networks-A Systematic Introduction Springer-Verlag. *New York*.

Rowland, F. S. (2006). Stratospheric ozone depletion. *Philosophical Transactions of the Royal Society B: Biological Sciences*, *361*(1469), 769-790.

Rubin, M. B. (2001). The history of ozone. The Schönbein period, 1839–1868. *Bull. Hist. Chem*, *26*(1), 40-56.

Ruddiman, W. F. (2001). *Earth's Climate: past and future*. Macmillan.

Russell, C. A., & McPherron, R. L. (1973). Semiannual variation of geomagnetic activity. *Journal of geophysical research*, *78*(1), 92-108.

Salas, J. D., Markus, M., & Tokar, A. S. (2000). Streamflow forecasting based on artificial neural networks. In *Artificial neural networks in hydrology* (pp. 23-51). Springer Netherlands.

Sanz, B. M., & Marqués, N. M. (2004). Total ozone time series analysis: a neural network model approach. *Nonlinear Processes in Geophysics*, *11*(5/6), 683-689.

Secretariat, G. C. O. S. (2009). Implementation plan for the global observing system for climate in support of the UNFCCC (2010 Update).

Selvaraj, R. S., Gopinath, T., & Jayalakshmi, K. (2010). Statistical relationship between surface ozone and solar activity in a tropical rural coastal site, India.

Indian Journal of Science and Technology, *3*(7), 793-795.

Shindell, D. T., Faluvegi, G., Miller, R. L., Schmidt, G. A., Hansen, J. E., & Sun, S. (2006). Solar and anthropogenic forcing of tropical hydrology. *Geophysical Research Letters*, *33*(24).

Silverman, D., & Dracup, J. A. (2000). Artificial neural networks and long-range precipitation prediction in California. *Journal of applied meteorology*, *39*(1), 57-66.

Skupin, J., Weber, M., Bovensmann, H., & Burrows, J. P. (2005, April). The Mg II solar activity proxy indicator derived from GOME and SCIAMACHY. In *Envisat & ERS Symposium* (Vol. 572).

Snow, M., Mcclintock, W. E., Woods, T. N., White, O. R., Harder, J. W., & Rottman, G. (2005). The Mg II index from SORCE. *The Solar Radiation and Climate Experiment (SORCE)*, 325-344.

Solanki, S. K. (2003). Sunspots: an overview. *The Astronomy and Astrophysics Review*, *11*(2-3), 153-286.

Solar structure (2015). Retrieved from http://www.columbia.edu

Solomon, S. (1986). RR Garcia FS Rowland DJ Wuebbles. *On the depletion of Antarctic ozone, Nature*, *321*, 755-758.

Sousa, S. I. V., Martins, F. G., Alvim-Ferraz, M. C. M., & Pereira, M. C. (2007). Multiple linear regression and artificial neural networks based on principal components to predict ozone concentrations. *Environmental Modelling & Software*, *22*(1), 97-103.

Sousa, S. I. V., Pires, J. C. M., Martins, F. G., Pereira, M. C., & Alvim- Ferraz, M. C. M. (2009). Potentialities of quantile regression to predict ozone concentrations. *Environmetrics*, *20*(2), 147-158.

Space Physics course (2011). Ozone UV-radiation, climate University of Oslo

Spiegel, E. A., & Zahn, J. P. (1992). The solar tachocline. *Astronomy and Astrophysics*, *265*, 106-114.

Spruit, H. (2000). Theory of solar irradiance variations. *Space Science Reviews*, *94*(1-2), 113-126.

Stanford, J. L., Ziemke, J. R., McPeters, R. D., Krueger, A. J., & Bhartia, P. K. (1995). Spectral analyses, climatology, and interannual variability of Nimbus-7 TOMS version 6 total column ozone.

Stein, M. L. (2007). Spatial variation of total column ozone on a global scale. *Annals of Applied Statistics*, **I**, 191—210

Stix, M. (2012). *The Sun: an introduction*. Springer Science & Business Media.

Stolarski, R. S., Krueger, A. J., Schoeberl, M. R., McPeters, R. D., Newman, P. A., & Alpert, J. C. (1986). Nimbus 7 satellite measurements of the springtime Antarctic ozone decrease. *Nature*, *322*(6082), 808-811.

Suess, K., Snow, M., Viereck, R., & Machol, J. (2016). Solar Spectral Proxy Irradiance from GOES (SSPRING): a model for solar EUV irradiance. *Journal of Space Weather and Space Climate*, *6*, A10.

Tapping, K. F. (2013). The 10.7 cm solar radio flux (F10. 7). *Space Weather*, *11*(7),

394-406.

Tapping, K. F., & Charrois, D. P. (1994). Limits to the accuracy of the 10.7 cm flux. *Solar physics*, *150*(1), 305-315.

Tharshini A. D. S., and Shanthi G. (2015). The Study of Solar Activity in Relation with High Frequency Variations of Solar Radio Flux. *American Journal of Astronomy and Astrophysics*.*3*(6): 87-92.

The structure of the Sun (2015). Retrieved from http://www.cs.berkeley.edu

Thiong'o, K. K. (2014). Kenya Meteorological Service National report of the 9th Meeting of the Ozone Research Managers of the parties to the Vienna Convention Geneva, Switzerland.

Tobias, S. M. (2002). The solar dynamo. *Philosophical Transactions of the Royal Society of London A: Mathematical, Physical and Engineering Sciences*, *360*(1801), 2741-2756.

Tobias, S. M., Brummell, N. H., Clune, T. L., & Toomre, J. (2001). Transport and storage of magnetic field by overshooting turbulent compressible convection. *The Astrophysical Journal*, *549*(2), 1183.

Tobiska, W. K., Bouwer, S. D., & Bowman, B. R. (2008). The development of new solar indices for use in thermospheric density modeling. *Journal of Atmospheric and Solar-Terrestrial Physics*, *70*(5), 803-819.

Toma, G., White, O. R., Knapp, B. G., Rottman, G. J., & Woods, T. N. (1997). Mg II core- to- wing index: Comparison of SBUV2 and SOLSTICE time series.

Journal of Geophysical Research: Space Physics, *102*(A2), 2597-2610.

Tsiropoula, G. (2003). Signatures of solar activity variability in meteorological
parameters. *Journal of Atmospheric and Solar-Terrestrial Physics*, *65*(4), 469-
482.

UNEP (1998). Environmental Effects of Ozone Depletion, 1998 assessment.
Photochemistry and photobiology, 205 pp Geneva: United Nations Environment
Programme.

UNEP (2003). Environmental Effects of Ozone Depletion: 2002 assessment.
Photochemistry and photobiology, 1–72 pp., Geneva: United Nations
Environment Programme.

Unruh, Y. C., Solanki, S. K., & Fligge, M. (1999). The spectral dependence of facular
contrast and solar irradiance variations. *Astronomy and Astrophysics*, *345*, 635-
642.

Usoskin, I. G. (2013). A history of solar activity over millennia. *Living Reviews in
Solar Physics*, *10*(1), 1-94.

Van den Berghe, D.H. (2012) How to Use the Solar Cycle. Retrieved from
http://www.fourpillars.net/contact.php

van der Leun, J. C., & de Gruijl, F. R. (1993). Influences of ozone depletion on
human and animal health. *UV-B radiation and ozone depletion: effects on
humans, animals, plants, microorganisms, and materials*, 95-123.

Varotsos, C. (2005). Power- law correlations in column ozone over Antarctica.
International Journal of Remote Sensing, *26*(16), 3333-3342.

Varotsos, C., Kondratyev, K. Y., & Efstathiou, M. (2001). On the seasonal variation of the surface ozone in Athens, Greece. *Atmospheric Environment*, *35*(2), 315 320.

Varotsos, C., & Kirk-Davidoff, D. (2006). Long-memory processes in ozone and temperature variations at the region 60 S–60 N. *Atmospheric Chemistry and Physics*, *6*(12), 4093-4100.

Veryard, R. G., & Ebdon, R. A. (1961). Fluctuations in tropical stratospheric winds. *Meteorol. Mag*, *90*(1,666), 125-143.

Viereck, R. A., & Puga, L. C. (1999). The NOAA Mg II core- to- wing solar index: Construction of a 20- year time series of chromospheric variability from multiple
satellites. *Journal of Geophysical Research: Space Physics*, *104*(A5), 9995-10005.

Viereck, R., Puga, L., McMullin, D., Judge, D., Weber, M., & Tobiska, W. K. (2001). The Mg II index: A proxy for solar EUV. *Geophys. Res. Lett*, *28*(7), 1343-1346.

Viereck, R. A., Floyd, L. E., Crane, P. C., Woods, T. N., Knapp, B. G., Rottman, G., ... & DeLand, M. T. (2004). A composite Mg II index spanning from 1978 to 2003. *Space Weather*, *2*(10).

Wang, W., Lu, W., Wang, X., & Leung, A. Y. (2003). Prediction of maximum daily ozone level using combined neural network and statistical characteristics. *Environment International*, *29*(5), 555-562.

Wenzler, T., Solanki, S. K., Krivova, N. A., & Fröhlich, C. (2006). Reconstruction of

solar irradiance variations in cycles 21–23 based on surface magnetic fields. *Astronomy & Astrophysics*, *460*(2), 583-595.

Welch, C. (2014). Data compiled from The British Antarctic study, NASA, NASA Ozone.

Whitten, R. C., & Prasad, S. S. (1985). Ozone in the free atmosphere. *New York, Van Nostrand Reinhold Co., 1985, 298 p. No individual items are abstracted in this volume.*, *1*.

Wikipedia (2012). Retrieved from http://en.wikipedia.org/wiki/Multilayer_perceptron

Wilks, D. S. (2011). *Statistical methods in the atmospheric sciences* (Vol. 100). Academic press.

Willmott, C. J. (1982). Some comments on the evaluation of model performance. *Bulletin of the American Meteorological Society*, *63*(11), 1309-1313.

Willson, R. C., & Hudson, H. S. (1988). Solar luminosity variations in solar cycle 21. *Nature*, *332*(6167), 810-812.

Willson, R. C., & Mordvinov, A. V. (2003). Secular total solar irradiance trend during solar cycles 21–23. *Geophysical Research Letters*, *30*(5).

World Meteorological Organization (2002), scientific assessment of ozone depletion: Global ozone research and monitoring project, Report No. (47): 181 – 382. Geneva: WHO

World Meteorological Organization (2003), Scientific assessment of ozone depletion: *Global Ozone Research. and Monitoring Project Report.,* 47**:***498 ., Geneva,*

Switzerland

World Meteorological Organization (1995), Scientific assessment of ozone depletion:
1994 *Global Ozone Research. and Monitoring Project Report.,* 37 *., Geneva,*
Switzerland

Zahid, M., & Rasul, G. (2010). Status of stratospheric ozone over Pakistan 1987-2008.
Journal of Environmental Protection, *1*(04), 374.

Zeilik, M., Gregory, S., & Smith, E. Introductory Astronomy and Astrophysics.
Philadelphia: Saunders College Publishers